SIMULATION OF SOLAR THERMAL APPLICATION IN A CEMENT PLANT

A THESIS SUBMITTED TO
THE GRADUATE SCHOOL OF NATURAL AND APPLIED SCIENCES
OF
MIDDLE EAST TECHNICAL UNIVERSITY

BY

SHADI SALEHIAN

IN PARTIAL FULFILLMENT OF THE REQUIREMENTS
FOR
THE DEGREE OF MASTER OF SCIENCE
IN
MECHANICAL ENGINEERING

JANUARY 2020

Approval of the thesis:

SIMULATION OF SOLAR THERMAL APPLICATION IN A CEMENT PLANT

submitted by **SHADI SALEHIAN** in partial fulfillment of the requirements for the degree of **Master of Science** in **Mechanical Engineering, Middle East Technical University** by,

Prof. Dr. Halil Kalıpçılar
Dean, Graduate School of **Natural and Applied Sciences**　　　　_____

Prof. Dr. M. A. Sahir Arıkan
Head of the Department, **Mechanical Engineering**　　　　_____

Prof. Dr. İlker Tarı
Supervisor, **Mechanical Engineering, METU**　　　　_____

Prof. Dr. Derek K. Baker
Co-Supervisor, **Mechanical Engineering, METU**　　　　_____

Examining Committee Members:

Assist. Prof. Dr. Ozgur Bayer
Mechanical Engineering, METU　　　　_____

Prof. Dr. İlker Tarı
Mechanical Engineering, METU　　　　_____

Prof. Dr. Derek K. Baker
Mechanical Engineering, METU　　　　_____

Prof. Dr. Murat Koksal
Mechanical Engineering, Hacettepe University　　　　_____

Prof. Dr. Cemil Kocar
Mechanical Engineering, Hacettepe University　　　　_____

Date: 30.01.2020

I hereby declare that all information in this document has been obtained and presented in accordance with academic rules and ethical conduct. I also declare that, as required by these rules and conduct, I have fully cited and referenced all material and results that are not original to this work.

Name, Last name : Shadi Salehian

Signature :

ABSTRACT

SIMULATION OF SOLAR THERMAL APPLICATION IN A CEMENT PLANT

Salehian, Shadi
Master of Science, Mechanical Engineering
Supervisor: Prof. Dr. İlker Tarı
Co-Supervisor: Prof. Dr. Derek K. Baker

January 2020, 158 pages

This study presents solar thermal application in the most energy consuming units of a cement plant located in Gaziantep, Turkey. Cement industry is the most important energy intensive and the second largest contributor to anthropogenic greenhouse gas emissions in the world which accounts for 5-6% of global CO_2 emissions. Both material and energy flows are analyzed in the system for a conventional cement industry and a solar integrated one taking the most energy-efficient innovations into account. The whole system is modeled in TRNSYS and is simulated using data from the literature. The reason TRNSYS software is used is the availability of a considerable number of variable components required to simulate thermal and electrical energy systems. The aim of this work is to assess how much electricity can be supplied by solar resources and fossil fuel energy can be replaced using solar thermal energy. By using solar hybridization at the calcination and clinkerization processes in the cement production line, fossil fuel and CO_2 emission flowrates are evaluated. According to the results, the studied solar-integrated systems produce

approximately half of the electrical work demand of the plant and contribute to the reduction in annual fossil fuel consumption and CO_2 emission by more than 10%.

ÖZ

ÇİMENTO FABRİKASI GÜNEŞ TERMAL UYGULAMASININ SİMÜLASYONU

Salehian, Shadi
Yüksek Lisans, Makina Mühendisliği
Tez Yöneticisi: Prof. Dr. İlker Tarı
Ortak Tez Yöneticisi: Prof. Dr. Derek K. Baker

Ocak 2020, 158 sayfa

Bu çalışma, Gaziantep'de bulunan bir çimento fabrikasının en fazla enerji tüketen birimlerinde güneş enerjisi uygulaması sunmaktadır. Çimento endüstrisi, en önemli enerji tüketicisi ve küresel CO_2 emisyonlarının %5-6'sını oluşturan dünyadaki antropojenik sera gazı emisyonlarına ikinci en büyük katkısıdır. Hem kütle hem de enerji akışları, sistemde geleneksel çimento endüstrisi ve güneş enerjisiyle entegre bir sistem için, enerji açısından en verimli yenilikleri dikkate alarak analiz edilir. Tüm sistem TRNSYS'de modellenmiştir ve literatürden veriler kullanılarak simüle edilmiştir. TRNSYS yazılımı, termal ve elektrik enerji sistemlerini simüle etmek için önemli sayıda değişken bileşen içerir. Bu çalışmanın amacı güneş enerjisi kullanılarak ne kadar elektrik sağlanabileceğini ve fosil yakıt enerjisinin güneş termal enerjisi kullanılarak değiştirilebileceğini değerlendirmektir. Çimento üretim hattındaki kalsinasyon ve klinkerizasyon işlemlerinde güneş hibridizasyonu kullanılarak fosil yakıt ve CO_2 emisyon debileri değerlendirilir. Sonuçlara göre, incelenen güneş enerjisi ile entegre sistem, tesisin elektrik iş ihtiyacının yarısını

üretmekte ve yıllık fosil yakıt tüketiminde ve CO_2 emisyonunda %10'dan fazla azalmaya katkıda bulunmaktadır.

Anahtar Kelimeler: Çimento endüstrisi, Güneş Çimento Fabrikası, Güneş Kalsinasyonu, CO_2 emisyonunun azaltılması, TRNSYS

To My Parents

ACKNOWLEDGMENTS

First of all, I would like to express my deepest gratitude to my supervisor Prof. Dr. İlker Tarı and my co-supervisor Prof. Dr. Derek K. Baker for their invaluable criticism, supervision and support throughout this study.

I shall thank the members of the examining committee for their helpful comments and constructive suggestions.

Finally, I would like to thank my family for their constant support, love and patience.

TABLE OF CONTENTS

LIST OF TABLES

LIST OF FIGURES

xx

LIST OF ABBREVIATIONS

ABBREVIATIONS

GHG	Greenhouse gas
SEC	Specific Energy Consumption
R/M	Raw meal
RM	Raw mill
PT	Pyroprocessing tower
RK	Rotary kiln
GCC	Grate clinker cooler
CSP	Concentrating solar power
HTF	Heat transfer fluid
CPC	Compound parabolic collector
ETC	Evacuated tube collectors
FR	Fresnel reflector
CTC	Cylindrical trough collector
PTC	Parabolic trough collector
PDR	Parabolic dish reflector
HFC	Heliostat field collector
PV	Photovoltaic
DNI	Direct normal irradiation
CV	Control volume
LHV	Lower heating value

LIST OF SYMBOLS

SYMBOLS

m	Mass (kg)
$\dot{m}$	Mass flow rate (kg h^{-1})
C_p	Specific heat at constant pressure (kJ kg^{-1} K^{-1})
h	Specific enthalpy (kJ kg^{-1})
$\dot{Q}$	Heat transfer rate (kJ.h^{-1})
$\dot{W}$	Work transfer rate (kJ.h^{-1})
η	Efficiency
ρ	Reflectivity
ε	Emissivity
P	Power (W)

CHAPTER 1

INTRODUCTION

1.1 Introduction

Concrete as a vital part of global construction industry is the most consumed material after water which is made up of three basic components of water, aggregate and cement [1,2]. Cement, which forms 10 to 15% of the fresh concrete's mixture is composed of limestone, alumina, shale, clay, iron ore and silica sand which are the basic raw materials abundantly available in mines. An indispensable global growth in production line of cement industry is seen from 2002 to 2007, which contributes to approximately 95 million tonnes of cement per year. From 2010 to 2012, approximately 3.5 billion tons of cement is produced each year [3]. Taking the population growth rate and urbanization into account, and without efforts to reduce demand, annual cement production is expected to increase reasonably until 2030 [4]. Cement manufacturing is the most energy intensive process consuming 12–15% of total industrial energy use which demands high quantities of natural resources (raw materials) and fossil fuel sources (e.g. coal, natural gas, lignite, petroleum coke, oil) to provide the majority of the essential energy in the cement industry [4,5]. About 30 to 40 percent of a cement industry's expenditures are related to fossil fuels and electricity [6]. Thermal energy is used in three main production steps including raw material mining and grinding in raw mill, clinker production in pyroprocessing unit and rotary kiln, and finish grinding with electrical energy consumption in grinding mill, motors, pumps, compressor, transformers, fans, and chiller [7]. Cement production consumes thermal energy of the order of 3.3 GJ/tonne of clinker produced and electrical energy of 0.3-0.4 GJ/ton of cement [8]. Global cement production was 24.6 million tons in 1960, 37.5 million tons in 1975, 33.1 million tons in 1980, and 24.4 million tons in 1990 which contribute to 4.8, 3.8, 3.4, and 3GJ fossil fuel energy

and 0.32, 0.34, 0.39, and 0.42 GJ electrical energy requirement per ton of cement respectively [9]. Cement plants release contaminants such as CO_2, NO_x, SO_2, CO, organic compounds, metals and minor pollutants to the atmosphere which are considered hazardous to human health [10]. Cement industry is responsible for 5-7% of the total anthropogenic CO_2 emissions predominantly produced in calcination and combustion processes [11]. Besides, electrical energy is used in the rotary kiln and for grinding and mixing raw materials as well as finished cement produces 100 kg of CO_2 per ton of cement [12]. Currently, CO_2 increase in the last five decades has led to global warming by 10% and a doubling of this amount would lead to a temperature rise by 1.6^{oc} [13,14].

Low thermal efficiency rate (about 50%) and high greenhouse gas (GHG) emission rate of cement industry makes it of paramount importance in terms of energy auditing. As a result, several energy efficiency technologies have been taken into account. These strategies mainly focus on cut of GHG emissions per ton of cement product. To illustrate, removing moisture content of raw material [15], proper insulation of potential heat loss equipments [16,17], heat recovery from exhaust gases [18]; multi-cyclone pyroprocessing tower [19], precalciner [20], waste heat recovery system for power production [21,22], variable speed grate cooler fans, and alternative fuels [23,24] are being used in practice. Alternative fuels such as biomass and waste with the benefit of depletion of the use of non-renewable fossil fuels and lower emissions of greenhouse gases only account for 6-7% of thermal energy used in 2017 [4]. Substituting alternative fuels for fossil fuels and mineral ashes derived from waste fuel for 5% of raw materials contributes to a worldwide reduction of CO_2 emission by 41Mt per year and 0.75Gt until 2050 respectively [25]. By the same token, integration of solar thermal into industrial processes are being studied and designed in order to mitigate CO_2 emissions. Solar hybridization in a cement plant would decrease fossil fuel consumption in calcination and kiln unit which would conduce to 40% CO_2 and 20% financial cost reduction [26]. The use of concentrated solar energy as a replacement to fossil fuel energy for driving the endothermic calcination reaction at above 1300K would lower CO_2 emissions by 20% in a state-

of-the-art cement plant and up to 40% in a conventional cement plant [27]. In the lime and cement sector, the SOLPART [28] project is to be mentioned since the target of the project is to provide, entirely or partially, the mandatory thermal energy for limestone calcination and fossil fuel combustion by using high temperature solar heat in three radical aspects: design of a high temperature solar reactor, high-temperature solid material transportation and high temperature thermal storage. This will aid diminish the negative environmental impacts of the process and enhance the use of renewable heating technologies and developments in industries [29]. Correspondingly, this thesis is devoted to boosting heat recovery issues and shortening the pollutant emissions diffused by combustion of fossil fuels.

In this thesis, the main units of a conventional cement plant comprised of raw mill, pyroprocessing tower, rotary kiln and clinker cooler are modeled in TRNSYS. The mass and energy flows in the system are assessed based on the law of conservation of mass and first law of thermodynamics. The essential data for modeling are extracted from literature that are actual measurements corresponding to a cement plant located in Gaziantep, Turkey [30]. Furthermore, a precalciner is added to the model to evaluate pyroprocessing unit's performance. Consequently, the exhaust gases of the cooler are recuperated to be used in the rotary kiln and grate clinker cooler.

The main objective of this study is to simulate the incorporation of solar energy into the cement plant in TRNSYS18 (Transient System Simulation Tool) using its built-in thermodynamic components and Solar Thermal Electric Components (STEC) library to optimize thermodynamic energy balances in the system in order to decrease the fuel consumption. The capital operational discrepancy between solar and conventional cement plants are predominantly derived from the process heat source. Solar hybridization demands a solar concentrating system to provide high temperature process heat for the calcination process. Thus, solar collectors are used in the rotary kiln unit to provide essential reaction energy for calcination and clinkerization in the rotary kiln in order to reduce non-renewable fuel sources usage

and generate electrical power, therefore reduce the environmentally detrimental emissions of CO_2. Thus, a heliostat field is added to the system and convincing results have been achieved.

1.2   Motivation and the Scope of the Thesis

This thesis is motivated by the need for an environmentally sustainable development in cement industry. Cement is by far the most fundamental and the most popular raw material in the global construction sector. Rising level set of self-evident problems such as the increase of CO_2 emissions with the potential of exacerbating global warming and depletion of nonrenewable energy sources encourages the researchers to try to make continuous strides. Not only is 40% CO_2 emitted by the use of thermal energy of fossil fuel combustion, but 50% CO_2 also is emitted in the calcination reaction [31]. For each tonne of Portland cement produced, approximately one tonne of CO_2 is emitted to the atmosphere. The main purpose is to find applicable strategies to reduce the electrical energy and fuel consumption in rotary kilns, which consume roughly about 7 tons of coal per hour. Cement production which consumes about 3.5 GJ of energy to produce one ton of cement, is an energy demanding process [16,30]. Theoretically, producing one tonne of clinker requires 3.7GJ thermal energy and 0.31GJ electricity [32]. However, using modern and suitable kiln systems, energy consumption can be cut down to about 2.9 GJ per one ton of clinker [33].

It may be appropriate to start out by stressing the fact that the solution is the gradual conversion to renewable resources. Solar energy as a beneficial heat source can be used to supply a thermal load. Solar energy can also be converted into electricity with two methods. Primarily, by collecting solar energy as heat then converting into electricity using a conventional power plant or heat engine. Secondly, by collecting solar energy and converting directly into electricity using photovoltaic cells [34], [35]. An advantage of hybridization is that the power plant can generate electricity on demand and so become more efficient. In brief, there has been ample number of studies on energy and exergy analyses in the cement sector but there are a few

researches on solar hybridization in a cement plant. Regularly, researchers are working on large-scale solar reactors, solar furnaces and thermal storage systems for high-temperature industrial plants.

The main objective of this dissertation is to simulate a solar-integrated cement plant in order to make use of concentrated solar radiation as the energy source of process heat to drive endothermic reactions. This project is motivated by task WP4 of INSHIP [36] (Integrating National Research Agendas on Solar heat for Industrial Processes) project which encompasses the technology and application of solar energy to high temperature industrial processes. Initially, a conventional cement plant is implemented in TRNSYS18, an extensible simulation environment for transient systems simulation, using thermodynamic components library, TESS library and STEC library to optimize thermodynamic energy balances in the system. Then, solar hybridization is synthesized in the units conducive to upgrading.

1.3   Thesis Objectives

The main objectives of this thesis can be summarized as follows:

- To simulate a traditional cement plant within TRNSYS
- To construct a solar-hybridized system model of the plant
- To compare the performance of both systems and evaluate reduction rates of fossil-fuel consumption and GHG emission

1.4   Thesis Structure

This research is organized in the following order:

Chapter 1 is the introduction to the whole study,
Chapter 2 presents the literature review of existing research,
Chapter 3 defines the basic concepts of a cement industry and cement manufacturing process,

Chapter 4 explains the solar thermal energy and solar collector types,

Chapter 5 presents the thermodynamic formulation of mass and energy balances in a system,

Chapter 6 is an introduction to TRNSYS and defines the modelling approach of a conventional and solar-integrated cement plant,

Chapter 7 presents the results and discussions of the cement plants,

After Chapter 7, Conclusions, References, and Appendix are included to the thesis.

CHAPTER 2

LITERATURE REVIEW

2.1   Previous Works

Cement industry has recently been an appealing subject of research. In several studies, performance and thermodynamic analysis of a cement industry have been investigated.

Madlool et al. [6] studied energy consumption and saving of a cement plant comprehensively. They used Specific Energy Consumption factor (SEC) (a key indicator of the efficiency of a cement plant usu. in MJ/t clinker) to indicate energy consumption of diverse units. Lower SEC value corresponds to a more energy efficient process. Thermal and electrical energy SEC values are presented in this study with maximum value of thermal SEC 4.60 GJ/tonne and electrical energy SEC 141 kWh/tonne in United States of America and minimum value of Thermal SEC 3 GJ/tonne and electrical energy SEC 88 kWh/tonne in India. Firstly, SEC calculations for different types of clinker manufacturing process showed that using multi-stage pre-heating stages could reduce energy consumption significantly. Secondly, they indicated that the dry cement manufacturing process is more efficient compared to the wet process as in the dry process 13% less electrical energy and 28% less fuel are consumed. They [37] also reviewed previous research on energy consumption and carbon dioxide emissions of a cement plant. As demonstrated in Figure 2.1, total energy sources for cement manufacturing sector are coal 53%, petroleum coke 21%, sponge coke 8%, natural gas 2%, Gasoline and oil 2%, tire derived 1% and electricity 13%. Total energy consumption of each unit of the cement-manufacturing sector is illustrated in figure 2.2 that corresponds to 4% raw materials preparation, 86% kiln fuel, 4% Kiln electricity, and 5% finish grinding. Subsequently, they studied energy saving and detrimental emission reduction technologies: Such as efficient piping

systems for raw materials preparation, raw meal homogenizing systems, roller mill systems, high-efficiency classifiers in grinding unit, roller mills for fuel drying by recuperating hot gases, advanced insulating refractories in kiln unit, mounting clinkerization process controllers in the rotary burner, using variable-speed fans, embedding a precalciner and using low pressure drop cyclones in the preheating tower, indirect firing for clinker making in rotary kilns, and optimizing heat recovery system in the plant.
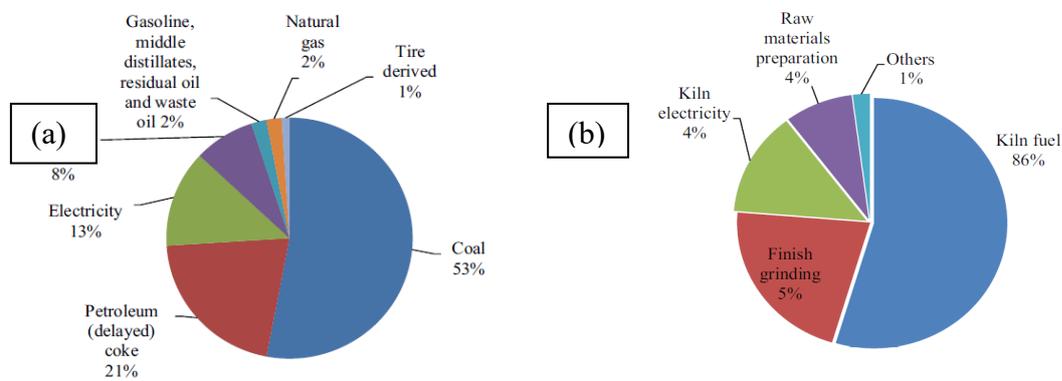
Figure 2.1 (a) Total Energy for Cement Manufacturing Sector by Energy Source, 2006 [37]; (b) Total Energy for Cement Manufacturing Sector by Process Step, 2006 [37]

Gao et al. [38] examined mass flow routes and mass balances in three production steps of roller mill, clinkerization and grinding units using on-site data. They showed that 2.48kg raw material is required to produce 1kg of input raw meal of a cement plant. In the roller mill, the materials from the roller press were classified into two groups of the coarse materials returning to the roller press for further grinding and the fine materials combined with the hot gas and leaking being transported to the dynamic separator for further filtering. In this unit, the waste rate was 63.31% and the recycle rate of waste was 16.33%. In the second unit, which was a combination of three sub-units of pyroprocessing tower, kiln and the cooler, coal was fed to the kiln to provide the energy for the clinkerization process of the input farine, clinker output of the kiln be rapidly air-cooled to prevent further chemical reactions. In this unit, the waste rate was 78.89% and the recycle rate of waste was 70.71%. In the

grinding unit, 4.00% gypsum was blended with 84.00% ground clinker, along with 7.00% additives, to produce finished cement. In this unit, the waste rate was 74.12% and the recycle rate of waste is 00.00%.

Atmaca et al. [39] studied the correlation between the specific electrical energy consumption of the raw mill unit and the vibration of the main driving motors of the unit. It was proved that by reducing the vibration rates of the motors, the electrical energy consumption reduced by 2.16%, which meant a saving of 0.55kWh/ton of farine production.

Sogut et al. [40] and Utlu et al. [16] performed energy and exergy analyses of a raw mill in a cement plant. They led thermodynamic analysis of the unit and proved that the efficiency of a raw mill could be increased by using energy recovery systems.

Kolip and Savas [41] analyzed a co-current four-cyclone preheater equipped with a precalciner type cement plant using first and second law of thermodynamics for the whole system. For precise calculation of energy, exergy and irreversibility, reaction energies of re-carbonation in the preheating stage, the calcination in the precalciner and rotary kiln as well as the clinker formation in the rotary kiln were calculated. According to the results, the first and second law efficiencies were 51% and 28%, respectively. In another study by the same research group [20], a comparative energy and exergy analyses and mass balance calculations were run for specific clinker production in a dry system for a serial and parallel flow four-cyclone precalciner cement plant. A serial flow pre-calcination system varies a parallel flow in being equipped with a burning cabin added to the bottom cyclone of the pyroprocessing unit. In the serial flow pre-heater cyclone system, calcination and the kilning processes occurred in the 60% and 40% of the rotary furnace length, respectively, while in serial flow pre-calcination systems, calcination and the kilning occurred in the 35% and 65% of the rotary furnace length, respectively. As a result, a serial flow pre-calcination system functioned better by 10%. Results of the study stated that the first law efficiency of a serial flow pre-heater cyclone system, a serial flow pre-calciner system and a parallel flow pre-calciner system were 32.36%, 32.73%,

31.27%, respectively. From these values, it was concluded that the lowest irreversibility rate occurred in the serial flow pre-calcination cement production method.

Kabir et al. [42] studied the energy auditing in the pyroprocessing tower of the cement industry. In order to enhance the thermal efficiency of the tower from an average value of 50%, the effects of the secondary kiln shell and a waste heat recovery steam generator were examined. In addition to the power and thermal energy savings of approximately 43 kWh/year and 5.3 MW, 14% drop in the GHG emissions was achieved, respectively.

Mikulcic et al. [43] put forward a CFD simulation of a precalciner model equipped with a swirl burner that resulted in more efficient combustion, less NO_x production and less CO_2 concentration inside the calciner.

Camdali et al. [44] conducted energy and exergy analyses in a rotary kiln with pre-calcinations using the material flows in it, Figure 2.2. In this study, the mass balances, the energy and exergy analyses, heat losses by conduction, convection and radiation were evaluated. The calculated first and second law efficiency of the kiln were 97% and 64%, respectively.
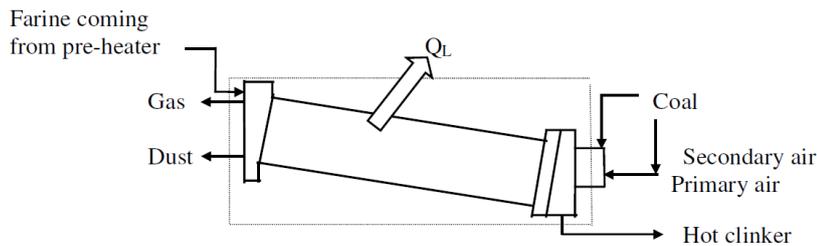
Figure 2.2 Rotary kiln and the materials going into and leaving

Wu et al. [45] assessed the heat loss through the kiln shell by using infrared thermography technique to measure the temperature field of the kiln shell in the calcination zone. It was concluded that less than 12% of the energy input into the

rotary kiln was lost through the whole kiln shell with 54% radiation and 46% convection heat loss.

Sogut et al. [46], Engin et al. [19], and Caputo et al. [47] examined heat recovery from the rotary kiln. Mastorakos et al. [48], Wirtz et al. [49], and Lauredan et al. [50] simulated the heat transfer inside the kiln; Granados et al. [51] and Wang et al. [52] modeled the combustion in the kiln. Besides, Gutierrez et al. [53] conducted energy and exergy analyses of the rotary burner.

Taweel et al. [54] simulated the temperature profile, the energy and exergy balances of a clinker cooler system placed after a rotary burner to reduce the temperature of the hot clinker by the fresh air supplied by the fans and recover the hot clinker's energy by heating the cooling air. Neglecting heat losses, temperature distribution profile at any length x of the cooler was derived:

$$T_{c_x} = T_{c_i} . e^{\frac{k.x}{m_c . C_{p_c} . \upsilon}} \qquad (2.1)$$

$$T_{a_x} = \frac{m_c . C_{p_c}}{m_a . C_{p_a}} \left(T_{c_i} . e^{\frac{-k.x}{m_c . C_{p_c} . \upsilon}} - T_{ambient} \right) + T_{ambient} \qquad (2.2)$$

where T_{c_x} is the temperature of clinker at any length x, T_{c_i} is the initial temperature of clinker, m_c is clinker mass, C_{p_c} is clinker heat capacity , m_a is air mass, C_{p_a} is air heat capacity, υ is viscosity, k is thermal conductivity and $T_{ambient}$ is the ambient temperature.

By substituting these equations in the first and second law of thermodynamics, the energy and exergy balance equations were obtained in terms of input temperature of clinker T_{c_i}. It was concluded that the temperature profile of the clinker bed had an exponential increase over the axial direction along the reciprocating blades of the cooler and the temperature of the clinker at the output was always less than the temperature of the clinker at the input.

The great clinker cooler's energy and exergy were also studied by Ahamed and Madlool [55] who investigated scenarios to increase energy and recovery energy

efficiencies, Amole [56] applied the second law of thermodynamics efficiency in the system in order to reduce heat loss and irreversibility, D. Touil et al. [57] modeled the great clinker cooler as a fully mixed cross heat exchanger and proved the importance of clinker inlet temperature ratio in entropy generation. Ahmad et al. [58] developed an energy model of the clinker cooler with the objective of the temperature variation derivation and simulations of heat losses through the walls of the compartment. Finally, Cao et al. [59] simulated an advanced structure for high-resistance grate plates in Ansys-Fluent and justified that by decreasing the pressure drop by 51.58%, performance of the cooler could be enhanced by 2.84%.

Atmaca investigated the raw mill [60], the pyroprocessing tower [17], rotary kiln [61], and grate clinker cooler of a conventional cement plant [62]. He studied the performance of all units of the cement plant based on the energy and exergy balances as well as exergoeconomic analysis [63,64]. Effects of ambient temperature, moisture content of raw materials, the effect of insulation on the efficiency of the cyclones, gas channels and rotary burner were analyzed. Finally, he applied a waste heat recovery system for electricity generation with the energy and cash savings of 886.16 kWh/year and 669,538 $/year, respectively [30].

Mujumdar et al. [65] developed a computational model taking the clinker manufacturing process into account, as illustrated in Figure 2.2, in order to investigate the performance of the preheater, calciner, kiln and the clinker cooler. Appropriate model of the preheater was created using the gas-solid heat transfer in the cyclones, the turbulent particle flow and the heat loss of the unit. Calciner was modeled by considering the simultaneous combustion of coal and calcination of raw material, heat transfer in the calciner and losses through the walls. A complex model of the rotary kiln was simulated by evaluating the coal combustion, gas-solid heat transfer, clinker formation, coating formation within the kiln and heat losses. Finally, the cross-flow heat transfer between the fresh air and hot clinker was modeled in the clinker cooler.
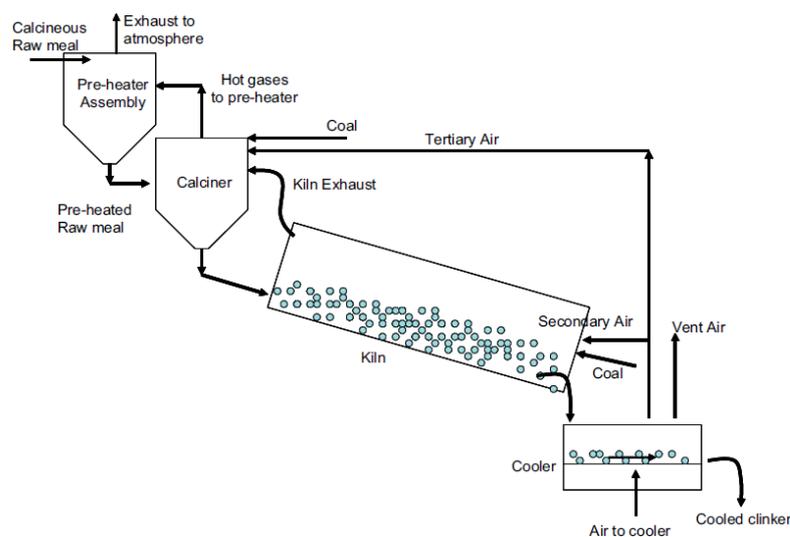
Figure 2.3 Schematic of cement clinker process [65].

Worell et al. [66] reviewed the total CO_2 emissions of a cement industry and investigated the emission mitigation options. Rahman et al. [67] used Aspen software to model the preheater tower based on the energy recovery from waste. It was concluded that using tyre as an alternative fuel by 25% could raise first law efficiency by 3% and reduce CO_2 by 2.5%. Likewise, Dong et al. [68] modeled a waste heat recovery system in a cement plant integrated with a CO_2 capture system and calculated the efficiency of the system using Aspen software. Mikulcic et al. [69] compared the various approaches to the GHG emission reductions, such as use of alternative raw materials, waste heat recovery, CO_2 capture and storage, and use of alternative fuels. Akgun [70] searched the feasibility of the reduction of the NO_x emissions in the rotary kiln. Finally, Meyer [71] proposed partial use of alternative cementitious materials in concrete industry in order to decrease GHG emissions in cement plants. For instance, use of fly ash (coal ash) by 30%, ground granulated blast furnace slag by 70%, condensed silica fume, municipal solid waste, concrete debris, recycled carpets, and tyres improve the environmental friendliness of concrete production.

Licht et al. [72,73] proposed a new thermal chemistry solution to produce CaO with Electrochemical Solar Thermal energy (STEP) without CO_2 emission. To elaborate,

the chemical reactions for the combustion of fossil fuel and conventional decarbonation of limestone to lime are:

$$nC + nO_2 \rightarrow nCO_{2\,+}\,Q_{heat} \tag{2.3}$$

$$CaCO_3 + Q_{heat} \rightarrow CaO + CO_2 \tag{2.4}$$

Using this strategy, limestone as a raw material of cement production undergoes solar heated electrolysis provided by a non-fossil fuel electricity source to produce lime, O_2 and carbonate without carbon dioxide emission.

Meier et al. [74] developed a solar chemical reactor, demonstrated in Figure 2.4, for efficiently processing calcination reaction. They built and tested a scalable indirect solar heating i.e. concentrated solar radiation penetrates through the aperture of a front shield and heats the absorber tubes that are arranged along the cylindrical cavity wall. By using this modern reactor, CO_2 emissions have declined by 20% in a recent cement plant and by 40% in a normal cement plant. The overall efficiency of the reactor is 30–35%. Their aim is to boost the overall efficiency to 45-55% by lowering conduction losses and preheating the limestone in the future.
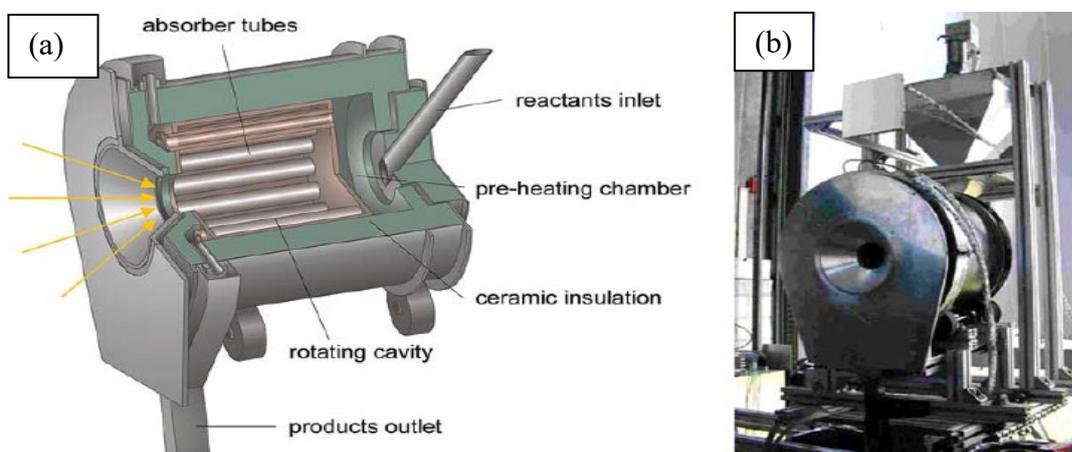
Figure 2.4 (a) Schematic of the multi-tube rotary kiln prototype [74]; (b) A solar kiln prototype [74].

Moumin et al. [75] discussed the potential of implementing solar thermal calciner technology in the form of a solar reactor in the cement industry. Heat could be

supplied via concentrated solar energy in two distinct ways of Top of Tower (TT) and Beam Down (BD) system. Correspondingly, a cement plant working in hybrid mode was designed. Using first law of thermodynamics, fuel thermal and solar thermal requirements of the plant were calculated in order to evaluate the maximum reduction rate of CO_2. The minimum emission value by utilizing the solar calciner was equal to 665 kg CO_2 per 1 ton of clinker. In addition, the maximum CO_2 reduction in the case of a 100% calciner solarization by nonrenewable fuel replacement in the conventional calciner was equal to 21%.

Abanades and Andre [76] developed a solar-heated rotary tube reactor model for the high-temperature heating of the raw meal particles in order to undergo calcination reaction. Correspondingly, Tescari et al. [77] focused on a large solar-driven rotary kiln for continuously transferring the solar heat to the particles of the kiln's feed and heating the particles to over $1000^{\circ C}$ at flowrates up to 20 kg/h. Additionally, Gonzalez [5] described the feasibility of solar hybridization in a cement plant by partially replacing the thermal energy requirement of the plant.

2.2   Gap and Objective

In the works cited in this chapter, the mass, energy and exergy, heat recovery systems, and the possibility of the conversion of a conventional rotary kiln to a solar reactor have been studied in the cement industry. However, to the best of author's knowledge, simulation of solar hybridization in cement production process has not been considered to date. The primary objective in this study is to consider a solar hybrid (solar energy + fossil fuel) operation in the rotary kiln of a cement plant. The mass and energy balances for the solar cement plant are performed using TRNSYS to quantify the solar energy required by the process to substitute the fossil fuel energy. In addition, the thesis targets at consumption of solar-heated air in the pyroprocessing tower in order to examine its impacts on fossil fuel consumption rate.

CHAPTER 3

CONVENTIONAL CEMENT MANUFACTURING PROCESS

3.1   Overview of cement manufacturing process

This chapter discusses the cement manufacturing process, its energy use, CO_2 emissions and alternative strategies to upgrade production system.

Joseph Aspdin invented a mixture of limestone and clay in 1824, and named it "Portland cement". Isaac Johnson invented the modern Portland cement in 1845. Cement manufacturing in industrial level was found in Poland in 1857 [78]. By growth of construction at the end of 19th century, small cement plants became widely spread. At the end of 20th century, cement became a globally popular material for construction implementations like roads, dams, bridges, tunnels, canals, and other infrastructure projects. Figure 3.1 shows the diagram of the cement manufacturing process [79].
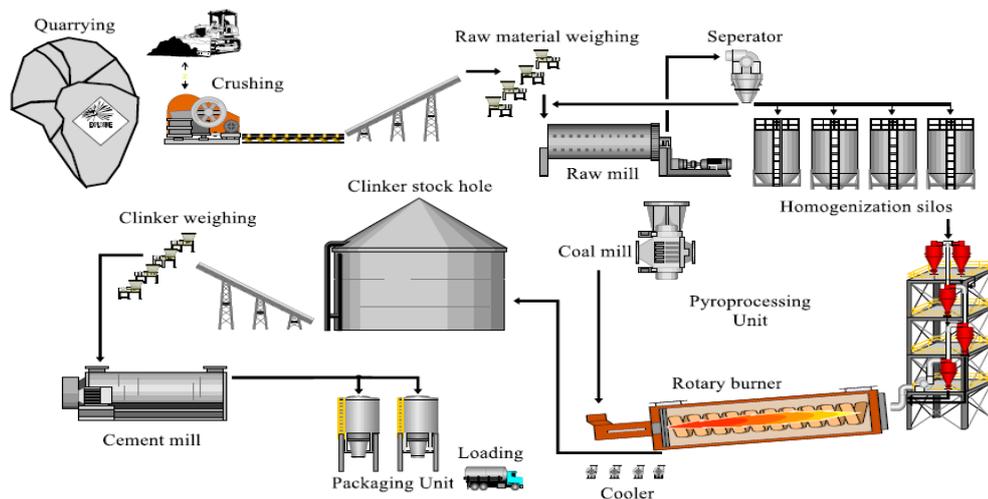
Figure 3.1 Process flow diagram of the cement manufacturing process [79].

There are 12 main stages in the manufacturing process of cement [80]:

1. Raw material quarrying and crushing in a mechanical crusher,
2. Conveying additives from storage silo,
3. Grinding the raw materials in a raw mill,
4. Blending the raw mixture in precise proportions in homogenization silos,
5. Preheating process in the pyroprocessing tower,
6. Precalcination process,
7. Clinker preparation in the rotary kiln.
8. Cooling in the grate clinker cooler,
9. Grinding coal particles in coal mill,
10. Grinding clinker in cement mill,
11. Storing cement in cement silo,
12. Packaging and dispatching cement

3.1.1 Brief description of cement manufacturing process

3.1.1.1 Limestone quarrying and crushing

Raw materials of cement production are 75% to 90% limestone supplying calcium carbonate ($CaCO_3$), silica sand and iron ore and alumina providing the main strength of the product, iron lowering the reaction temperature, magnesium carbonate and impurities [81]. Limestone is obtained from quarrying mines, consuming 85% of the total energy of this unit, through the process of heavy blasting and mucking out the rocks with loaders. After a quality control, which consists of removing soil, vegetation and impurities, mechanical conveyor belts are used to transport the raw material in varied sizes from 0.5 mm to 0.5 m particles in diameter. Consuming the remainder 15% of the energy, the limestone is crushed, using a pyrocrusher, an impact hammer mill or a clinker hammer crusher [82], in three crushers in a row to be scaled down into smaller chunks of 20-25mm in size and transported to the next unit [83].

3.1.1.2   Additives storage hopper

Some iron, bauxite, and silica are added to achieve the precise proportions of raw feed composition so that a quality cement clinker can be produced. These materials are stored in silos or hoppers and are transported using conveyor belts in conjunction with weigh-feeders [84].

3.1.1.3   Raw mill

There are various types of raw mills that can be used to grind up the raw mix before the process stage. A high-pressure roller press (HPGR) (ball mill) a tube mill [82], an impact mill or a centrifugal roller mill [85], a vertical roller mill (VRM) [86], and a ring roll mill [87] can be used for a grinding process. The raw mix is dried using the excess part of heat recuperated from the cooler in this stage to reduce moisture content of the raw feed.

3.1.1.4   Blending and storing silo

Homogenization of raw meal is done by aerating it in this section. It is necessary to blend and homogenize the raw material efficiently. The raw meal is distributed radially in eight zones and aerated every 5 minutes. In order to blend and homogenize the raw materials properly, continuous blending silos are used [88].

3.1.1.5   Pre-heater

The most efficient pyroprocessing systems consist of preheaters, a precalciner, and a rotary kiln. The first main cement production process commences in this stage. Homogenized raw meal is fed to the pyroprocessing tower with a height varying from 50 to 180 m. Here, the meal is exposed to high temperature gases in order to be preheated in a series of 4 to 6 countercurrent flow cyclones [89]. These multi-stage

cyclones are the main components for the heat transfer from the kiln to the raw materials. They serve as heat exchangers and separators [90]. The most of heat exchange between farine and exhaust gases from rotary kiln occurs in the connecting lines between the various cyclones [89,91]. Pressure drop of the whole system increases with the increase of number of cyclones [92]. In the end of this unit, the raw meal and hot gas are discharged at about 1000K from the bottom cyclone and 500K from the top cyclone, respectively.

3.1.1.6   Precalcination process

All of the recent and efficient pre-heater towers contain a combustion chamber at the bottom of the tower. Figure 3.2 shows a dry kiln with a pre-heater and a pre-calciner [6]. The precalcination chamber is known as a pre-calciner used with the objective of preheating and partially calcining of the meal. In this stage, the preheated raw material is burnt to undergo calcination reaction. The basic chemical process of the cement manufacturing begins with the decomposition of $CaCO_3$ at about 900°C to calcium oxide (CaO, lime) and gaseous CO_2 [93]. Calcination reaction is a highly endothermic reaction, with a heat requirement of 1784 kJ per kg of $CaCO_3$ [53]. This energy is supplied from the combustion of solid fuels along with the exhaust gases from a rotary kiln. Using a precalciner in the system decreases the NO_x emission and the energy consumption of clinkerization by 8 to 11% [21].
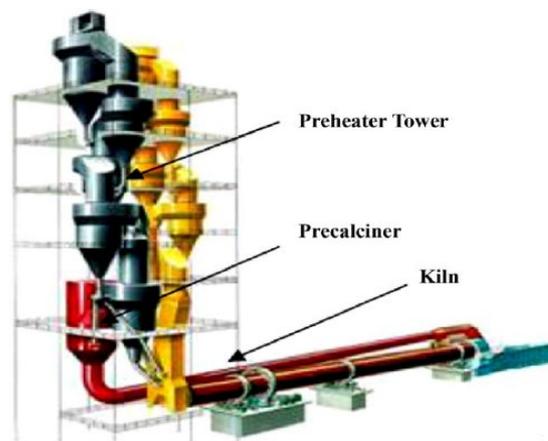
Figure 3.2 Pre-heater Tower and Pre-calciner [6].

3.1.1.7   Clinker preparation in the rotary kiln

The feed i.e. farine which is the semi product of clinker from the preheater tower is discharged to the upper end of a cylindrical rotary kiln, the central component of a cement plant, with a length ranging from 60 to 200m and a diameter of 3 to 9m. Rotary kilns are more commonly used than vertical kilns (shaft kilns). The shell of rotary kiln is made of mild steel plate. For further reinforcement of the shell, castings of heat resistant steel attached to the end of the mild steel to retain the refractories. Refractories are inner-wall brick lining of the shell fitting the curvature of the kiln used to protect the shell from the high temperatures of the feed and combustion gases [94].

Generally, there are seven types of rotary kilns [95]:

- Wet rotary kiln

    When the moisture content of the raw material is 15-25%, a wet slurry is made to feed into the kiln. In this case, due to the homogeneity of the meal, less electrical energy is used for grinding. Nevertheless, since extra energy is needed to evaporate water content in the slurry, overall energy consumption is 30% higher than the dry type.

- Semi-wet rotary kiln

    It is the advanced version of wet kiln. The moisture content of the material is reduced using a filter resulting in a decline in energy consumption by 0.3 GJ/tonne of clinker.

- Semi-dry rotary kiln

    Waste heat recovered from the kiln is used to remove moisture content of the raw meal. Then, it is fed into the kiln. This will reduce overall energy consumption.

- Dry long rotary kiln

  This type of kiln includes long dry kilns without pre-heater and kilns with one-cyclone pre-heater. In this type, energy consumption is 33% more than the new dry kilns with pre-heater and pre-calciner (PH-PC kiln) [96].

- Dry rotary kiln with pre-heater

  Rotary kilns equipped with 4–6 multistage cyclone preheaters are in this category. Cyclones are placed above each other in a tower with approximately 100m height. The kiln length is rather shorter than the previous ones. Since a partial calcination reaction takes place in the preheater, energy consumption can be reduced. The only disadvantage of this type is the production of alkali that may cause interruptions in the operations.

- Dry kilns with pre-heater and pre-calciner

  In this case, an additional combustion chamber is installed between the pre-heating tower and the kiln. A proportion of exhaust gas from cooler and 60% of the fuel used in the kiln are consumed in the pre-calciner. Since 80–90% of the calcinations occurs here, energy consumption is reduced by 8–11%.

- Shaft kiln

  Shaft kilns are static production systems in which the raw material (limestone in various particle sizes) is fed into the kiln from the top, from where it moves downwards through the kiln shaft purely by gravity [97]. By introducing heat energy from fuel, a chemical reaction takes place, whereby the limestone ($CaCO_3$) is split into lime (CaO) and carbon dioxide (CO_2). A number of cement plants with shaft kilns can be found in China and India.

The actual range of thermal energy demand for each type of the kilns is shown in the center column of table 3.1 [98]. The last column shows the average values of thermal energy consumption collected in 2006 [99].

Table 3.1 The thermal energy demand for each type of the kiln [98,99].

TECHNOLOGY	Specific thermal energy demand	
	MJ/t Clinker	Averaged MJ/t Clinker
Dry process, multi-stage cyclone (3-6 stages) preheater and pre-calciner kiln	3000 to 4000	3382
Dry process rotary kilns equipped with cyclone preheaters	3100 to 4200	3699
Semi-dry/ semi-wet processes	3300 to 5400	3844*
Dry process long kilns	Up to 5000	4489
Wet process long kilns	5000 to 6400	6343
Shaft kilns	3100 to 6500 and higher	-
Electricity demand	90 to 150 kWh/t cement	

(*)Not including the energy needed for drying

In a cement plant, a kiln is placed with a slope of 3-4 degrees with the horizontal [95] and rotates at a speed ranging from 0.5 rpm to 5 rpm [100]. The inclination of the kiln makes the raw material tumble through it towards hotter zones (heated by fire of combustion reaction) where the farine undergoes chemical and physical changes to comprise the clinker. Clinkerization is the main step in the dry cement manufacturing process that starts typically at 1400-1500$^{\circ C}$. The red-hot clinker is discharged from the end of the kiln.

3.1.1.8   Cooling in the grate clinker cooler

The clinker coming out of the kiln at approximately 1500$^{\circ C}$ is cooled by ambient air blown using multiple fans over the hot clinker to reduce its temperature to approximately 170 $^{\circ C}$ [101], demonstrated in Figure 3.3 [102]. Cooling prevents

further changes of the clinker. The exhaust air of this unit is recovered to feed the kiln and pre-calciner burners [103].
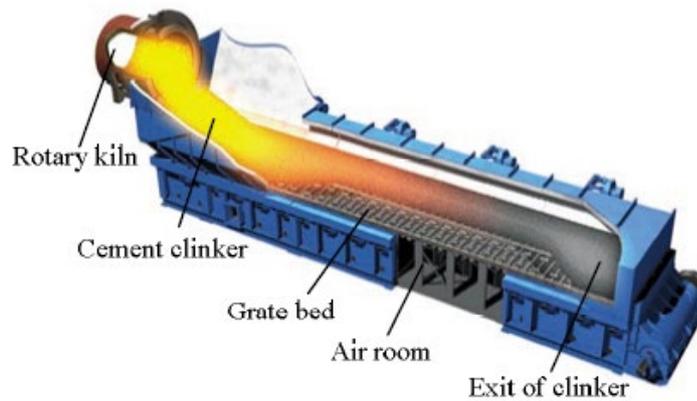
Figure 3.3 The schematic diagram of grate cooler [102].

3.1.1.9 Grinding coal particles in coal mill

A coal mill is usd to control the temperature and fineness of the coal [104].

3.1.1.10 Grinding clinker in cement mill

This is the final step in a cement manufacturing process. In this step, a cement mill grinds the clinker along with some additives (e.g. gypsum) [86].

3.1.1.11 Storing cement in cement silo

Cement is stored on site in waterproof and dry bulk silos in order to prevent the negative impacts of humidity on the cement.

3.1.1.12 Packaging and dispatching cement

Cement is packaged and distributed by bulk cement delivery trucks.

CHAPTER 4

SOLAR THERMAL ENERGY

4.1 Overview of Solar Thermal Energy

Population growth in global scale and rising demand for energy from fossil fuels play a key role in air pollutants and GHG increments, which induce inconvenient situation for the environment [104]. To overcome this problem, complementary energy sources and renewable energies like biogas, biomass, solar energy, and geothermal energy are implemented [105]. Solar energy has innumerable advantages including environmental protection, being a clean and constant renewable energy source, free availability in many regions, reduced dependence on fossil fuels, low maintenance costs, and application diversity [106]. Furthermore, it offers large-scale possibilities, such as large-scale low-carbon solar thermal power plants in combination with seasonal storages and heat pumps, and power generation systems [107].

Solar energy can be used for electricity (photovoltaic cells) or heat generation (solar thermal) with the help of solar energy systems. Figure 4.1 shows the most basic system types schematically. In the first diagram, the solar resource is captured and converted into heat to be supplied as a thermal load. Then it can be used for house heating, water heating or industrial processes. This type of system may or may not include thermal storage, and usually include an auxiliary source of energy so that the demand may be met during long periods with no sunshine. According to the diagram, there are two methods for the conversion of solar energy into electricity. The first method to provide electrical load is to collect solar energy heat then convert it into electricity using a regular power plant or heat engine. The second method is to collect solar energy heat then convert it directly into electricity using photovoltaic cells [35].
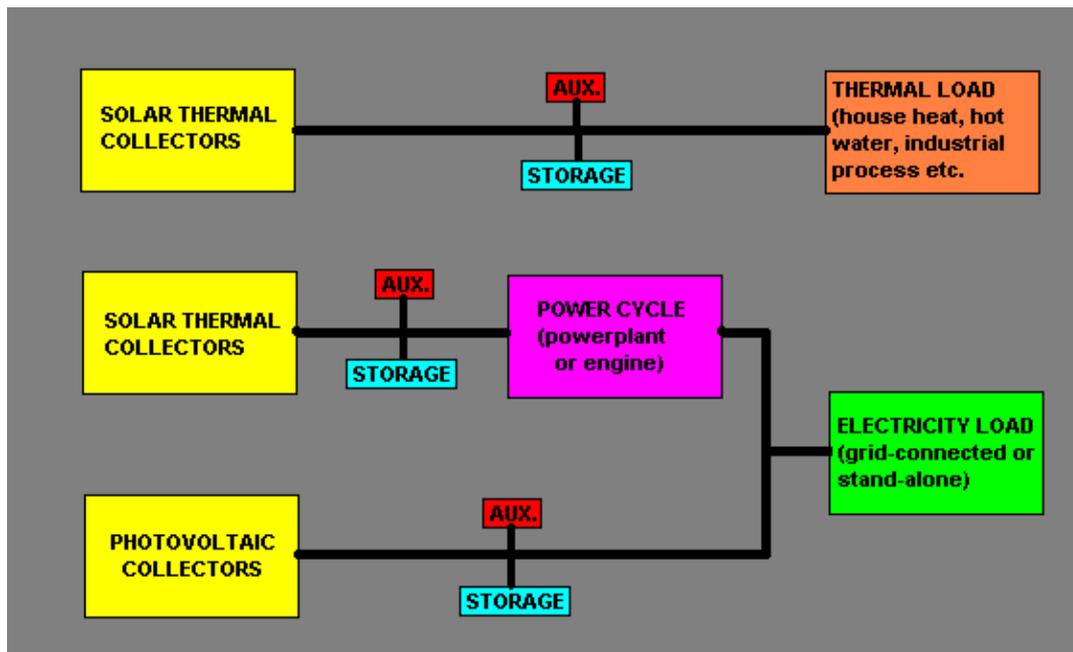
Figure 4.1 Diagram of a basic solar energy conversion system. The AUX. box represents some auxiliary source of thermal or electrical energy [35].

Thus, solar thermal energy is the utilization of energy obtained from solar irradiation, transferred to a heat carrier medium. Solar collectors capture incident solar radiation energy to heat a heat transfer fluid (HTF) to a high temperature. Solar thermal can be used through three temperature levels with distinguished technologies put into operation [105]:

a. Low-temperature collectors with temperature levels around $65^{\circ C}$. Such as, all individual hot water systems for buildings and houses

b. Medium-temperature collectors concentrating solar radiation supplying useful heat at higher temperature usually between $100^{\circ C}$ and $300^{\circ C}$

c. High-temperature collectors with temperature levels higher than $500^{\circ C}$. Here, steam production is possible for power generation.

26

4.2   Solar Radiation

Solar radiation (insolation) is radiant energy emitted by the sun. Figure 4.2 shows global direct normal irradiation [108]. According to the figure, irradiation variations on the earth shows that some regions intercept more solar energy because of local climate effects and the relative motion of the sun with respect to the earth. It can be implied that solar energy can be used over the entire globe with some modifications in the collector fields' size.
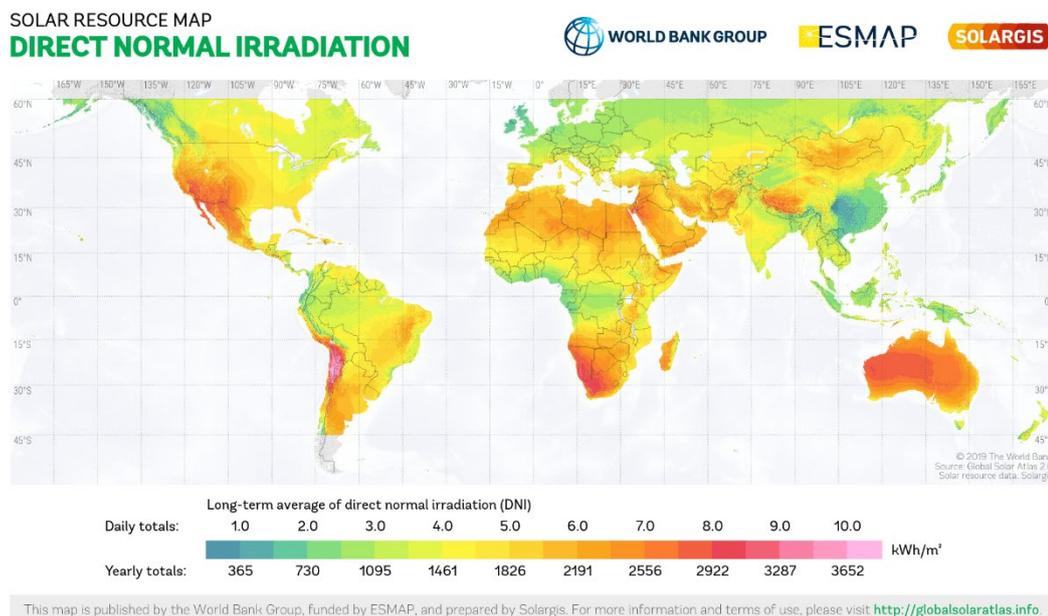
Figure 4.2 Global map of direct normal irradiation [94].

The amount of energy concentration of solar collectors changes with respect to the insolation changes. Therefore, the solar-integrated systems should be backed up by fossil fuels.

Solar thermal collectors are divided according to their motion and the operating temperature. Motion-based collectors are three types [109]:

Stationary collectors are fixed in position and do not track the sun. Three collector types of this category are:

1. Flat plate collectors

They are the most widely used type As shown in the Figure 4.3, a large blackened absorber plate is heated by the solar energy and converted to thermal energy. Heat exchange occurs between the plate and the fluid in the tubes or ducts. In order to reduce heat loss from the plate to the atmosphere, one or more transparent plates are placed in front of the absorber plate. Flat plate collectors absorb the beam normal radiation and diffuse radiation. This type of collectors were developed for use in sunny and warm climates. Their efficiency reduces in severe cold conditions [35]. They are low-temperature collectors with temperature ranges between $30^{\circ C}$ and $80^{\circ C}$.
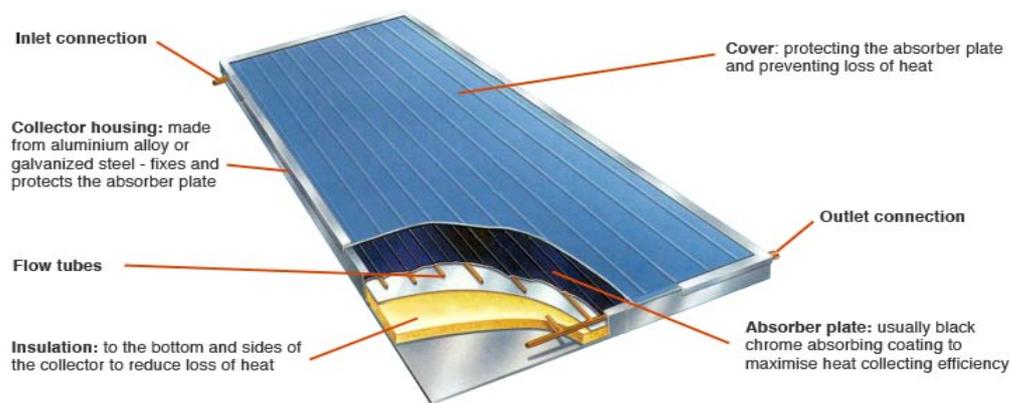
Figure 4.3 Flat-plate solar collector [110].

2. Stationary compound parabolic collectors (CPCs)

CPCs collect the divergent light and reflect all of the incident radiation within wide limits to reach the absorber. CPCs are defined using an acceptance angle, which is the angular range in which a CPC can collect light. Any radiation intercepting the aperture within the collector acceptance angle reaches the absorber surface by multiple reflections. CPCs are ideal for the applications that require concentrating the divergent light source. They are medium-temperature collectors with temperature ranges between $60^{\circ C}$ and $240^{\circ C}$. A tracking CPC can be a better option when higher levels of temperature are needed (up to $300^{\circ C}$) [109]. Figure 4.4 shows a detailed structure CPCs [111,112].
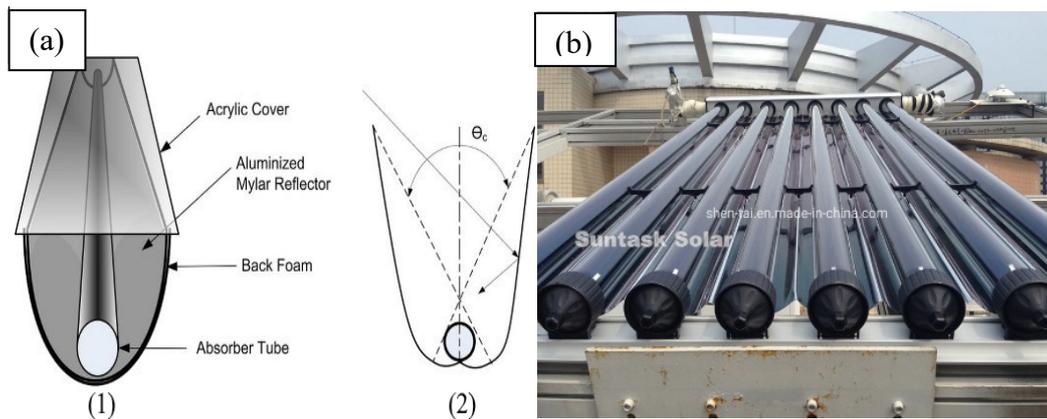
Figure 4.4 (a) Schematic of: (1) one compound parabolic collector, (2) The value of acceptance angle θc; (b) Poland CPC solar collector.

3. Evacuated tube collectors (ETCs)

ETCs consist of a sealed copper pipe placed inside a vacuum-sealed tube. The tube walls are two layers of glasses, vacuumed between. ETCs collect both direct and diffuse radiation. Solar insolation intercepts the outer layer, passes through the vacuumed space and is absorbed by the inner tube. The temperature of the inner tube's surface can rise up to $300^{\circ C}$ while the outer surface is cool enough to be touched. On the other hand, the pipe is covered with a layer of aluminum that is in contact with the tube's inner surface. Aluminum layer transfers the heat into the sealed pipe. The pipe is a highly efficient thermal conductive fluid (e.g. methanol) container. As shown in the Figure 4.5 [113,114], the liquid evaporates and travels to the condenser bulb protruding from the top of each tube. The condenser bulb is usually placed inside the manifold of a tank containing water. Therefore, the vapor condenses and releases its latent heat. The condensed fluid returns to the solar collector as a liquid and the evaporating-condensing cycle is repeated. These collectors show better performance than flat-plate collectors at high temperatures do because the vacuum envelope reduces the heat losses. These medium temperature collectors with temperature ranges between $65^{\circ C}$ and $200^{\circ C}$.
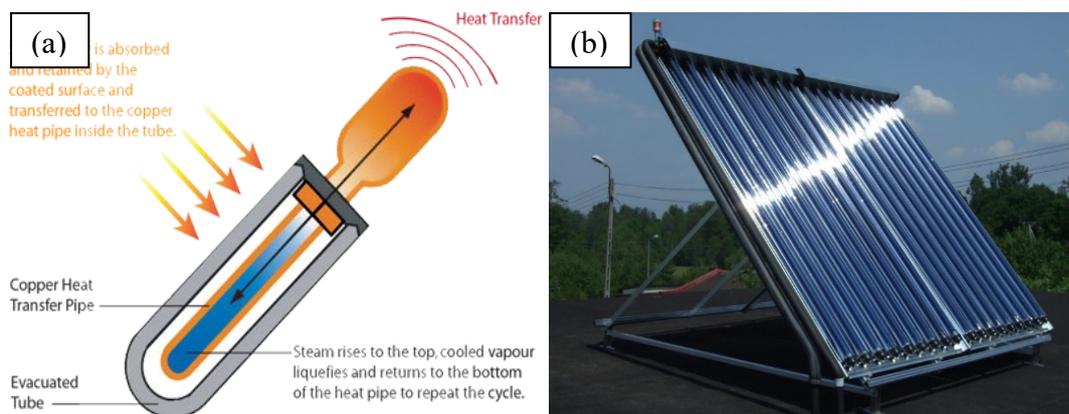
Figure 4.5 Diagram of an ETC [113]; (b) ET solar collector [114].

Single-axis tracking collectors rotate on one axis moving back and forth in a single direction to follow the sun's path to maximize energy capture. Three collector types of this category are [109].

1. Fresnel reflector (FR)

Fresnel collectors are divided into two categories [115]: The Fresnel lens collector (FLC), shown in Figure 4.6, and the linear Fresnel reflector (LFR), shown in Figure 4.7. The former collector focuses the parallel solar rays to a point receiver and uses refraction rather than reflection to collect energy. Whereas the LFR uses an array of linear mirror strips to concentrate sunrays onto a linear receiver.
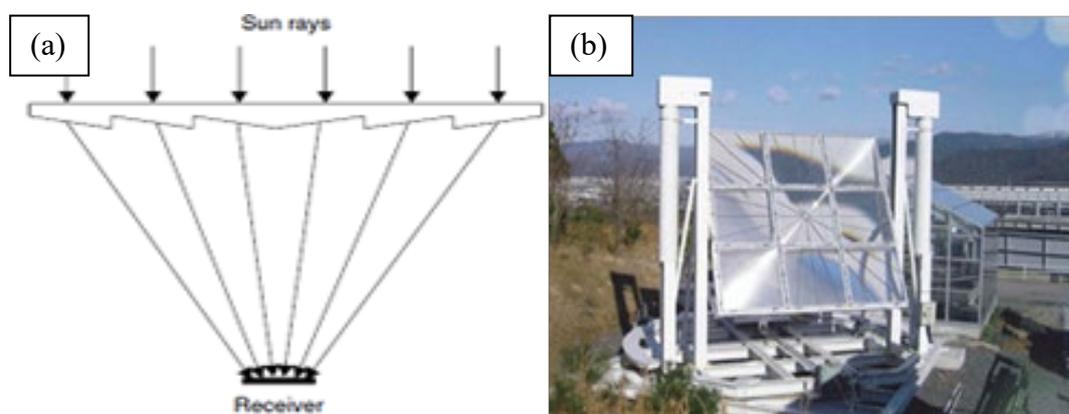
Figure 4.6 (a) Fresnel lens collector (FLC) [109]; (b) FLC solar furnace [114].
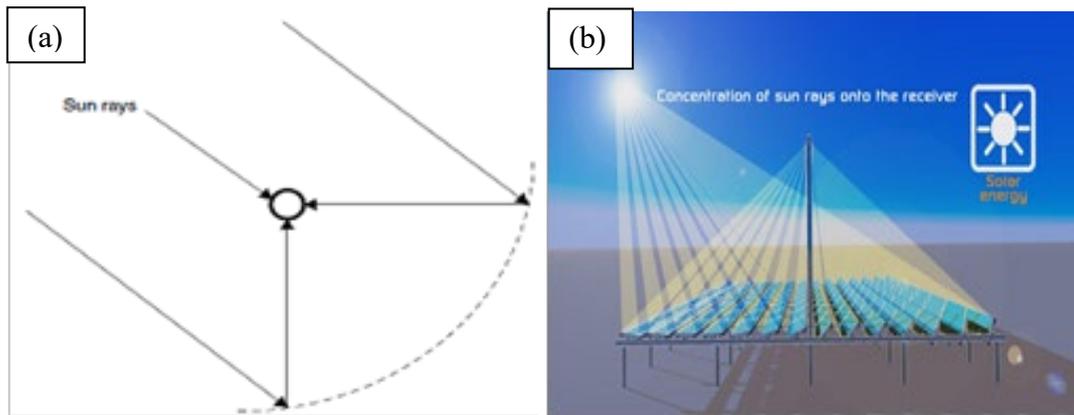
Figure 4.7 (a) Linear Fresnel-type parabolic trough collector [109]; (b) a downward-facing receiver illuminated from an LFR field [115].

2. Cylindrical trough collector (CTC)

CTCs are made by bending the reflective material and flexing it into a cylindrical shape as shown in Figure 4.8 [116]. The receiver inside the cylinder is painted in black and in order to reduce the thermal losses, a transparent (glass) cylinder encloses it. Since the collector is single-axis tracking, it tracks the sun's motion and absorbs sun's energy. The heat transfer fluid moving along the receiver is heated in this way [117].
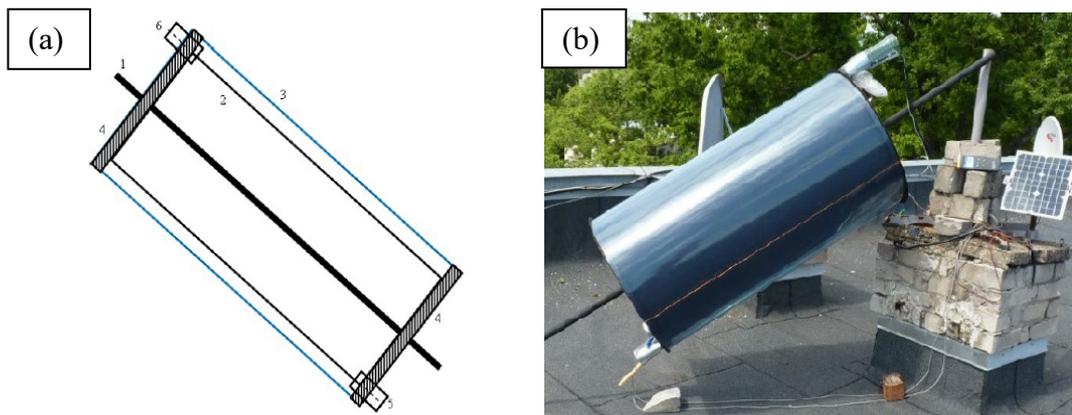
Figure 4.8 (a) Structure of cylindrical solar collector: 1. Axis, 2. Inner cylinder-absorber, 3. Outer transparent cylinder, 4. Thermoinsulation at ends, 5. Inflow opening, 6. Outflow opening [116]; (b) Cylindrical solar collector [116].

3. Parabolic trough collector (PTC)

The parabolic-shaped collectors reflect the incident solar radiation onto a tube-like receiver. The absorbed solar energy heats the fluid running inside the tube as shown in the Figure 4.9 [118]. Temperature ranges between $220^{\circ C}$ and $400^{\circ C}$ can be reached without considerable heat loss [119].
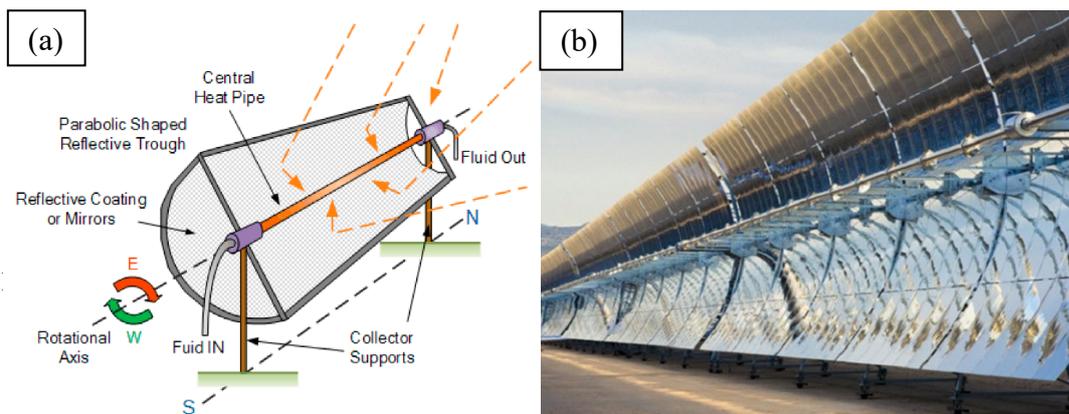
Figure 4.9 (a) General conceptual form of a PTC [118]; (b) A parabolic trough collector [35].

Dual-axis tracking collectors track the sun in two axes. Two collector types of this category are:

1. Parabolic dish reflector (PDR)

PDRs concentrate the solar radiation onto a receiver aperture in the focal point. Absorbed energy is converted into thermal energy in an insulated fluid container [109]. Figure 4.10 shows a PDR [110,120]. PDRs are high-temperature collectors with temperatures in over and above $1500^{\circ C}$. Thereupon, the thermal load of these systems can be converted directly into electricity or transported to a central power plant [119].
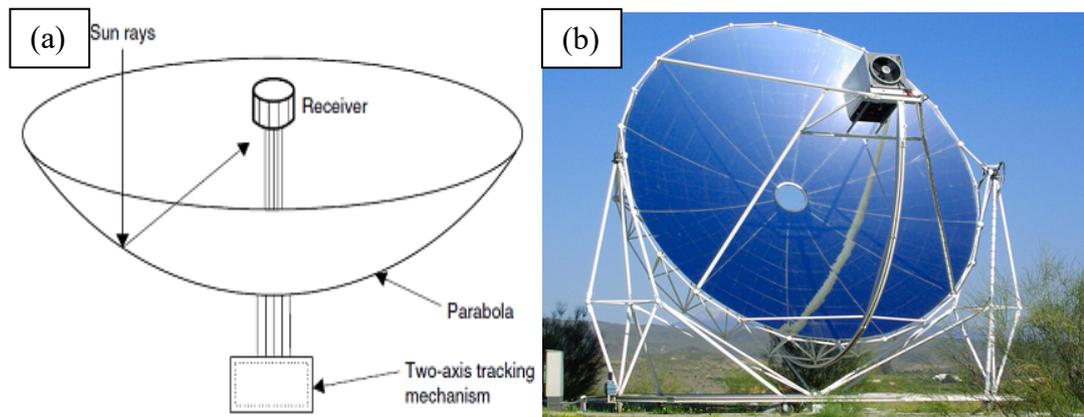
Figure 4.10 (a) Schematic diagram of a PDR [110]; (b) a PDR [120].

2. Heliostat field collector (HFC)

HFCs (heliostat field collectors) consist of an array of individual heliostats (flat mirrors), distributed around a receiver that reflect their incident direct solar radiation onto a central receiver located on top of a tower as shown in Figure 4.11 [121,122]. These systems are high-temperature collectors and achieve temperatures up to $1350^{\circ C}$. Thermal load of these systems can be used to charge steam generators [123].
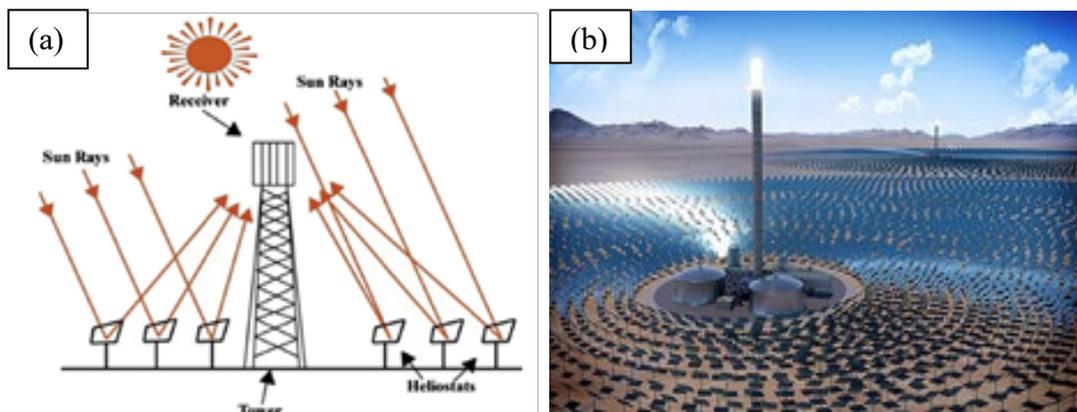
Figure 4.11 (a) Schematic diagram of a HFC [121]; (b) A heliostat solar field [122].

The concentration ratio (C), defined as the ratio of the average concentrated solar flux to the solar irradiation of $1kW/m^2$ [124] is used to characterize the optical

concentrators. It is calculated as the aperture area divided by the receiver or absorber area of the collector [109]. Tracking solar concentrators have larger concentration ratios than stationary solar collectors [125]. To illustrate, in a heliostat solar field, higher concentration ratios are achieved since a solar receiver tower system concentrates the sunlight onto a fixed receiver mounted at the top of a tower reaching a higher energy conversion efficiency [126].

Table 4.1 presents the concentration ratio and indicative temperature range of the commonly used solar collectors [109,119].

Table 4.1 The concentration ratio of solar energy collectors [109,119].

Tracking Mechanism	Collector Type	Focal Type	C	Operating temperature range (°C)
Stationary	Flat-plate collector	Flat	1	30-80
	Evacuated tube	Flat	1	50-200
	Compound parabolic	Focal line	1-5	60-240
Single-axis	Compound parabolic	Focal line	5-15	60-300
	Parabolic Trough	Focal line	30-100	60-400
	Linear fresnel	Focal line	10-40	60-250
	Cylindrical trough	Focal line	15-50	60-300
Two-axis	Parabolic dish	Focal point	1000-2000	Over 1800
	Heliostat field	Focal point	300-1500	Up to 2000

4.2.1 Solar Radiation Geometry

For solar applications, one needs to reasonably predict the solar position in the sky at any time of a day and a year. The solar altitude angle α_s and the azimuth angle γ_s are two basic variables for the solar position:

- The solar altitude angle, α_s, is the angle between the line to the sun's center and a horizontal plane relative to the earth [127].
- The solar azimuth angle, γ_s, is the angle between the projection of the line of sun beam onto the horizontal surface and an arbitrary axis on the surface [128]. The reference arbitrary axis is usually the due south for the Northern Hemisphere [109]. It is to be cited that displacements east of south are negative and west of south are positive [127].

In Figure 4.12 [127,129], two angles related to the sun position and the angles β, γ, Θ, and Θ_z are shown that are to be defined.
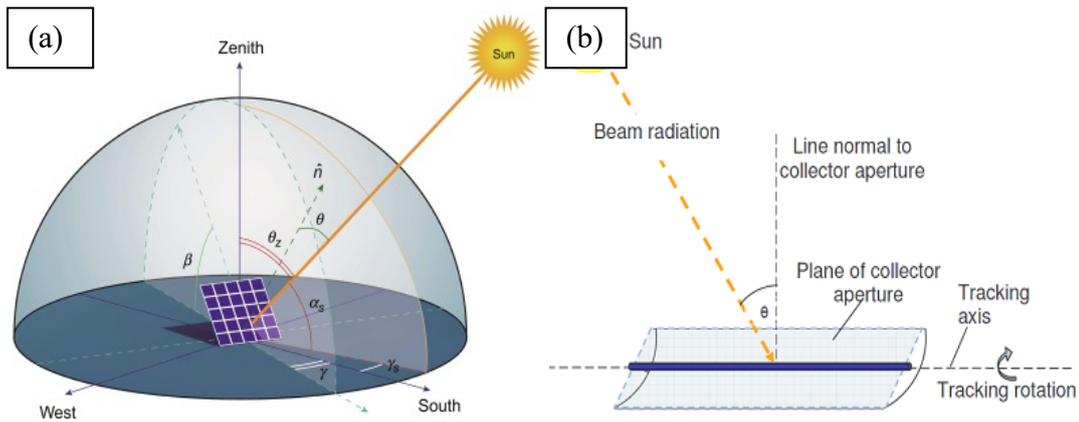
Figure 4.12 (a) Solar and PV module characteristic angles [129]; (b) Angle of incidence on a parabolic trough collector [127].

Θ_z, the zenith angle, is the angle between the sun's rays and the vertical line relative to the earth [130]. The zenith angle is the complement of altitude angle:

$$\theta_z + \alpha_s = \frac{\pi}{2} \tag{4.1}$$

γ, the surface azimuth angle, shows the angle between the normal to the solar panels and true south in degrees. In other words, this angle is measured according to the equator. An azimuth value of zero means that the panel is facing the equator in both northern and southern hemispheres [109].

β, the tilt angle or surface slope, is the angle between the solar panel's surface and the horizontal plane relative to the earth [127]. β ranges between $0°$ and $180°$. When $β > 90°$, the surface faces downward [128].

Θ, the angle of incidence, as shown in figure 4.12b, is the angle between the sun's rays and the normal line to the PV (photovoltaic) surface [109]. Incidence angle is the relationship between the sun's position in the sky and the orientation of the collectors for a given location [127].

Another angle that is needed to be defined is declination angle δ. The earth axis of rotation (the polar axis) is tilted on its axis at an angle of 23.45° from the ecliptic axis. Ecliptic axis is the normal axis to the ecliptic plane, which is the plane of orbit of the earth around the sun. Declination angle is the angular position of the line connecting the sun's center to the Earth center with respect to the projection of this line on the plane of the equator (north positive). Declinations north of the equator are positive and those south are negative. This angle varies throughout a year. As shown in Figure 4.13 shows the declination angle during the equinoxes and the solstices [124].
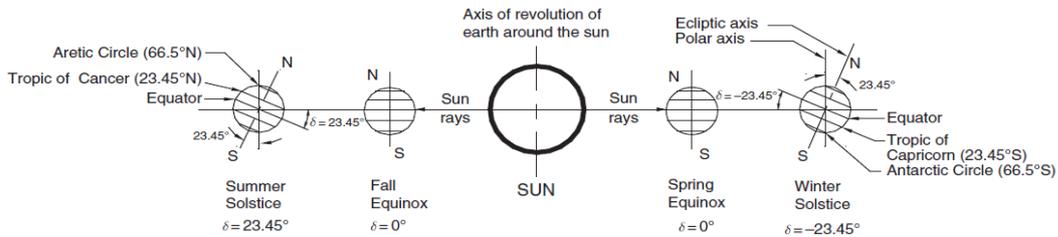
Figure 4.13 Yearly variation of solar declination [124].

The declination angle δ in degrees is calculated by the following equation for any day of the year (N) [129]:

$$\delta = 23.45° \sin\left[\frac{360°}{365°} \cdot (284 + N)\right] \tag{4.2}$$

where N = the day number of the year, from 1 (corresponding to January 1) to 365 (corresponding to December 31).

4.2.2   Solar Radiation Components

Since solar rays pass through the atmosphere and the clouds to reach the ground, a portion of the solar heat is scattered and absorbed by the atmosphere, and reflected back into the space. Solar radiation is the integration of solar irradiance over a period. The total solar irradiance is the aggregate of direct beam radiation, diffuse radiation and the reflected radiation [109,127]. In Figure 4.15 [129], components of solar radiation are represented. While non-concentrating solar collectors can use both direct and indirect radiation, concentrating solar collectors use direct irradiance.
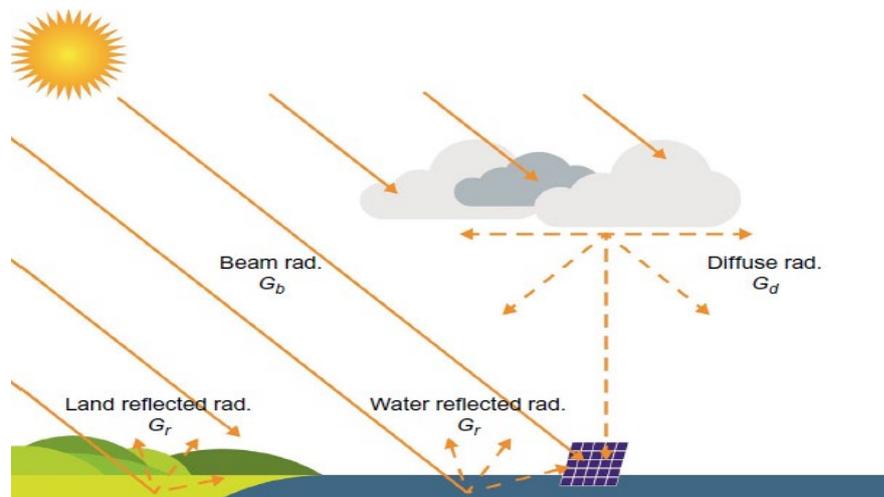
Figure 4.14 Solar radiation components striking the ground and the PV panel [129].

- Direct Normal Insolation (DNI) or direct beam radiation is the flux of the unscattered and direct normal light from the sun that reaches the flat surface of the earth that is perpendicular to the sun's rays.

- The diffuse radiation is the amount of solar energy that reaches the earth's surface after being scattered by atmosphere, clouds and particles. Diffuse

radiation ranges between 30% of the solar radiation on clear sky days and 80% on cloudy days.

Incident radiation is the spectral radiative solar heat flux that strikes the specific surface. Incident diffuse radiation is the portion of the diffuse radiation that strikes the surface. Extraterrestrial horizontal radiation is the amount of solar radiation on a horizontal surface at the top of the atmosphere that is the summation of total amount of direct and diffuse solar radiation received on a horizontal surface [109]. Global horizontal radiation is the addition of the direct radiation and the diffuse radiation on the horizontal plane [129].

4.3   Heliostat Field with Central Receiver

Due to the advantages of heliostats with central receiver, a heliostat field is modeled in this thesis. According to the Table 4.1, the highest operation temperatures can be achieved using heliostat fields. To elaborate, a heliostat field is made up of individual heliostats demonstrated in Figure 4.16 [124] that follow the Sun in two axes and concentrate the solar arrays onto a receiver area located on top of a tower. By absorbing the solar radiation in a receiver, it is feasible to convert it into heat by energy conversion devices.

Figure 4.15 Heliostats developed by eSolar [124].

A heat transfer fluid (HTF), a fluid or gas, is used to transport heat in the system. Criteria for choosing a suitable HTF are heat capacity, thermal conductivity, reached outlet temperature, and heat flux density [124]. Water/steam was a commonly used HTF consumed in steam cycles [131]. However, several problems of using water as HTF in the solar cycles are the storage, corrosion effect, and the transient behavior of water/steam at changing weather conditions. Nowadays, the molten salt is an appealing choice of an HTF and can only be used in closed solar power cycles [132]. Air as HTF has the advantage of being environmentally benign and free and the highest fluid outlet temperature can be achieved. Air can be operated in both open and closed solar power cycles [133].

As mentioned previously, the heliostat field concentrates the solar beams onto a receiver presented in Figure 4.17 (b). Not all of the radiation reaches the surface because of the atmosphere attenuation and spillage losses due to the dilution of light. Further, not all of the radiation is absorbed due to the reflectivity ratio of the receiver material. Wind velocity induces forced convection at the absorber surface. Other thermal losses from the receiver are natural convection, forced convection induced by wind velocity, conduction and radiation from the receiver to the environment. Thermal losses also take place in the piping process of the heat transport of the HTF. Figure 4.17 (a) displays different loss mechanisms at the receiver [124].
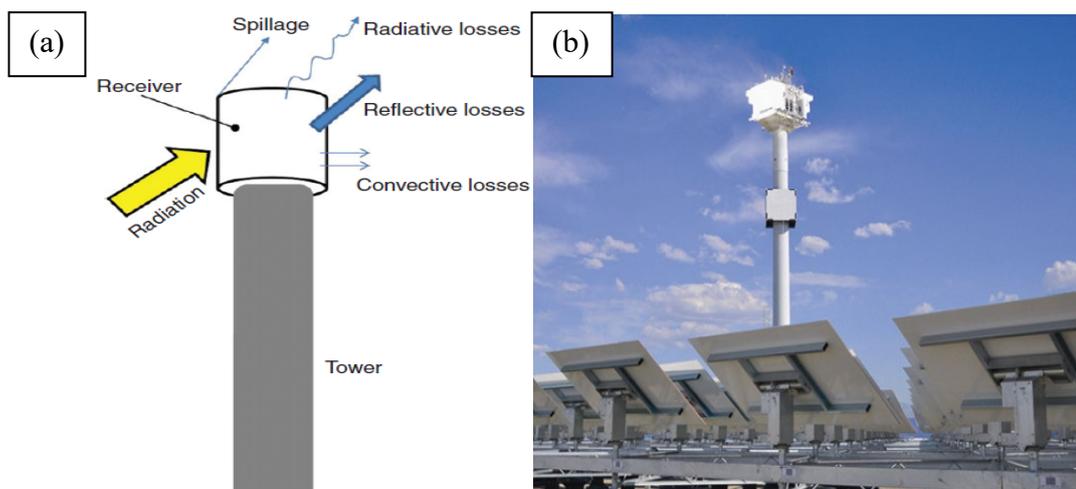
Figure 4.16 (a) Energy balance of a solar receiver [124]; (b) Solar receiver system of eSolar [124].

Receiver efficiency may be defined as [124]:

$$\eta_{receiver} = \eta_{sp}\eta_{abs}\eta_{rad}\eta_{conv}\eta_{cond} \tag{4.3}$$

where η_{sp}, η_{abs}, η_{rad}, η_{conv}, and η_{cond} are efficiences based on receiver spillage, absorption, radiation, convection, and conduction losses, respectively.

4.3.1   Pressurized Air Receiver

The receiver type used in this thesis is a pressurized air receiver with the advantage of the higher achievable efficiency at temperatures above $700^{\circ C}$ [134]. The high-temperature pressurized solar air receiver is designed for heating compressed air to the entrance conditions of a gas turbine in the pressure range 4 to 30 bar and temperature range $800^{\circ C}$-$1200^{\circ C}$ to generate power [135].

CHAPTER 5

FORMULATION

5.1   Thermodynamic Analysis of the Cement Plant

There are two basic laws in thermodynamics that are used in the thermodynamic analysis of the cement plant, the first one is Conservation of Mass law and the second one is the First Law of Thermodynamics in a control volume.

Conservation of mass equation, commonly termed as the continuity equation, shows that the rate of change of mass within a control volume is the subtraction of the output mass flowrate from the input mass flowrate.

$$\frac{dm_{C.V.}}{dt} = \sum_{i=1}^{n} \dot{m}_{in,i} - \sum_{i=1}^{n} \dot{m}_{out,i} \qquad (5.1)$$

where $\dot{m}$ stands for mass flowrate and the subscript "C.V." stands for control volume, "in" for input and "out" for output.

The first law of thermodynamics is an expression of the conservation of energy i.e. energy cannot be created or destroyed; it only changes from one form to another. Similarly, any rate of change of energy in the control volume is caused by the rate of input or output energy of the control volume. The general form of the first Law of thermodynamics equation is:

$$\frac{dE_{C.V.}}{dt} = \dot{Q}_{C.V.} - \dot{W}_{C.V.} + \sum_{i=1}^{n} \dot{m}_{in,i} h_i - \sum_{i=1}^{n} \dot{m}_{out,i} h_i \qquad (5.2)$$

where $\dot{Q}_{C.V.}$ is heat transfer rate to the control volume, $\dot{W}_{C.V.}$ rate of work of the control volume done on its environment, h is the total enthalpy; and the subscript "C.V." stands for the control volume, "in" stands for input and "out" for output [136].

41

In this thesis, the input and output mass flow rates of each unit are adopted from [30]. The energy analyses in the process are performed by using the first law of thermodynamics. The specific heat capacities have been calculated for each of the input and output materials with respect to their temperatures and constituent materials [137].

In order to analyze the units thermodynamically, the following assumptions are made:

- The system is assumed as a steady state, steady flow process.

- The temperature of the environment is taken as the actual ambient conditions using the Weather Data sub library of TRNSYS.

- Kinetic and potential energy changes are negligible.

- The gases inside the whole plant are assumed to be ideal gases.

- The combustion reaction in the kiln is complete in the conventional and hybridized cement plant.

- The shaft work in the units is produced by electrical energy.

- The lower heating value (LHV) of the fuel is used because there is no secondary condenser after the combustion chamber and it is assumed that the water vapor generated from burning fuel is discharged in the exhaust stream [138].

5.1.1   Mass and energy balance equations

In order to find mass and energy balances in a steady state flow process, the following balance equations are applied. The mass balance is expressed as:

$$\sum_{i=1}^{n} \dot{m}_{in,i} = \sum_{i=1}^{n} \dot{m}_{out,i} \tag{5.3}$$

where the subscript "in" stands for input and "out" for output.

$$\dot{Q}_{C.V.} - \dot{W}_{C.V.} = \sum_{i=1}^{n} \dot{m}_{out,i} h_i - \sum_{i=1}^{n} \dot{m}_{in,i} h_i \tag{5.4}$$

The first law efficiency is the ratio of transferred energy to the actual amount of energy input, which is:

$$\eta_1 = \frac{\sum_{i=1}^{n} \dot{E}_{out,i}}{\sum_{i=1}^{n} \dot{E}_{in,i}} \tag{5.5}$$

The specific heat of incompressible substances such as liquids and solids does not change with temperature or pressure during a process. Furthermore, the constant volume and constant pressure specific heats are identical. Therefore, both specific heats can be represented by a "c".

$$c_v = c_p = c \tag{5.6}$$

In incompressible substances, the specific heats depend only on temperature. Correspondingly, the internal energy change of a system with incompressible substances that remain in single phase during a process can be determined by the average specific heat. The change in internal energy of solids and liquids can be expressed as:

$$\Delta U = m c_{ave} \Delta T \tag{5.7}$$

where c_{ave} is the average specific heat at the average temperature [139].

Since the pressure drop across the units are low enough to be neglected, the enthalpy change is equal to the internal energy change of a material. So, the enthalpy change of materials with respect to the ambient conditions can be expressed as:

$$\Delta h_{in} = c_{avg} \left(T_1 - T_0 \right) \tag{5.8}$$

$$\Delta h_{out} = c_{avg} \left(T_2 - T_0 \right) \tag{5.9}$$

where T_1 and T_2 are the input and output temperatures of the materials and T_0 is the ambient temperature.

When incompressible substances with different specific heat values are mixed, the temperature of the mixture can be calculated as:

$$T_{mix} = \frac{\sum\limits_{i=1}^{n} \dot{m}_i c_i T_i}{\sum\limits_{i=1}^{n} \dot{m}_i c_i} \qquad (5.10)$$

The specific heat value of the mixture, neglecting the enthalpy of mixing, is calculated as:

$$c_{mix} = \frac{\sum\limits_{i=1}^{n} \dot{m}_i c_i (T_i - T_0)}{\sum\limits_{i=1}^{n} \dot{m}_i . (T_{mix} - T_0)} \qquad (5.11)$$

5.2   Heliostat Solar Field with Central Receiver

The power supplied by the heliostat field in the TRNSYS model is [140]:

$$\dot{Q}_{receiver} = A_{field} . \rho_{field} . I . \eta_{field} . \Gamma \qquad (5.12)$$

with the total heliostat surface A_{field}, reflectivity ρ_{field}, direct normal radiation I, the heliostat field efficiency η_{field}, and a control parameter Γ standing for the fraction of the field in track.

The efficiency of the steady-state pressurized air receiver is obtained by [140]:

$$\eta_{receiver} = \eta_{opt} - \varepsilon . \sigma . \frac{A_{abs}}{P_{rad}} . \overline{T}_{abs}^4 , \qquad (5.13)$$

$$\overline{T}_{abs} = 0.5(T_{air,in} - T_{air,out}) + 273.15 \qquad (5.14)$$

using the optical efficiency of the absorber η_{opt}, emissivity of absorber ε, Stefan-Boltzmann coefficient σ, fraction of aperture area of the receiver for absorption A_{abs}, inlet and outlet temperature of air $T_{air,in}$ and $T_{air,out}$.

CHAPTER 6

TRNSYS MODELS

This chapter consists of three major sections. The first is an introduction to TRNSYS software. The second is building a conventional cement plant model located in Gaziantep and analyzing the mass and energy balances in TRNSYS. The final section includes modeling of a solar integrated cement plant in TRNSYS.

6.1   TRNSYS

TRNSYS (TRaNsient System Simulation) program is a software that is developed primarily at The University of Wisconsin and is an extendible and flexible simulation environment for the transient simulation of systems [141]. The standard libraries of the TRNSYS simulation studio contain around 60 components in different domains: electrical, hydronics, HVAC, controllers, storage systems, loads and structures, solar equipment, etc. This list can be completed by additional libraries such as STEC (Solar Thermal Electric Components) library [140], and TESS (Thermal Energy Systems Specialists) library [142], but also one can add custom-made components using Fortran, C or C++ programming languages. STEC library is developed by DLR (German Aerospace Centre) and Sandia National Laboratory and consists of Rankine and Brayton sublibraries, concentrating solar thermal systems (central receiver, heliostat field, and parabolic trough models), and storage systems. In addition, TRNSYS can call external programs like Microsoft Excel and MATLAB. Components used in the simulation studio are selected from components toolbar and added to the workspace. For modeling a larger system, components are connected to each other. Each Type is described by a mathematical model in the TRNSYS simulation engine. The software has useful documentations such as full description of Types, mathematical reference for Types, examples and tutorials. Figure 6.1

shows the graphical interface of the simulation studio. When the system is configured, the TRNSYS input file (a text file known as the "deck" file) can be created and the simulation launched directly from the simulation studio. Each type has a variable table consisting of the parameters and inputs that can be modified by the user. The output tab shows the outputs of a component that can be inputs to another component. Figure 6.2 shows the Variable Information Window of a cooling tower component. The outputs of the first component are connected inputs of second model by Link Mode menu command. Figure 6.3 displays how a sample connection is created [143].

Figure 6.1 The TRNSYS Simulation Studio: Model of a solar domestic hot water system

Figure 6.2 Cooling tower Variable Table

Figure 6.3 A sample connection

The simulation engine is programmed in Fortran and each component type has a source code. After running the simulation, all the information of the input file is called by the TRNSYS executable, "TRNExe.exe", which implements the output sub library to plot or print the results of the simulation.

6.2   A Conventional Cement Plant Model (Model-1)

In the first section, a model of a cement plant is created using components from the main, TESS and STEC libraries. The schematic flow diagram of the cement plant shown in Figure 6.4, is modeled in TRNSYS. A schematic of the model in the TRNSYS simulation studio is presented in Figure 6.4. Information flows are indicated by connections between two components [68].
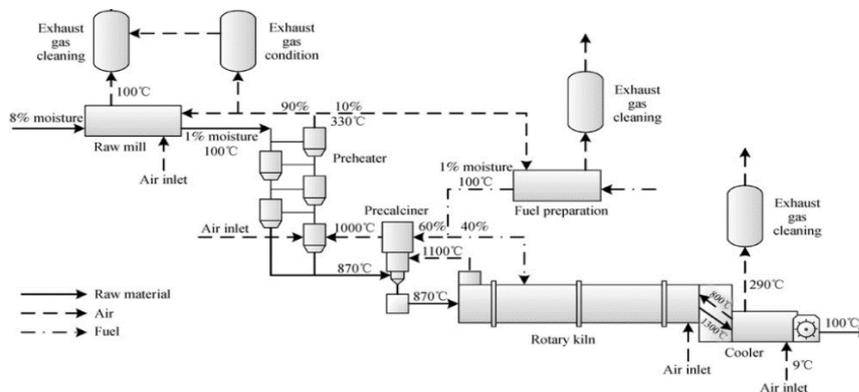
Figure 6.4 General flow diagram for a cement plant [68],
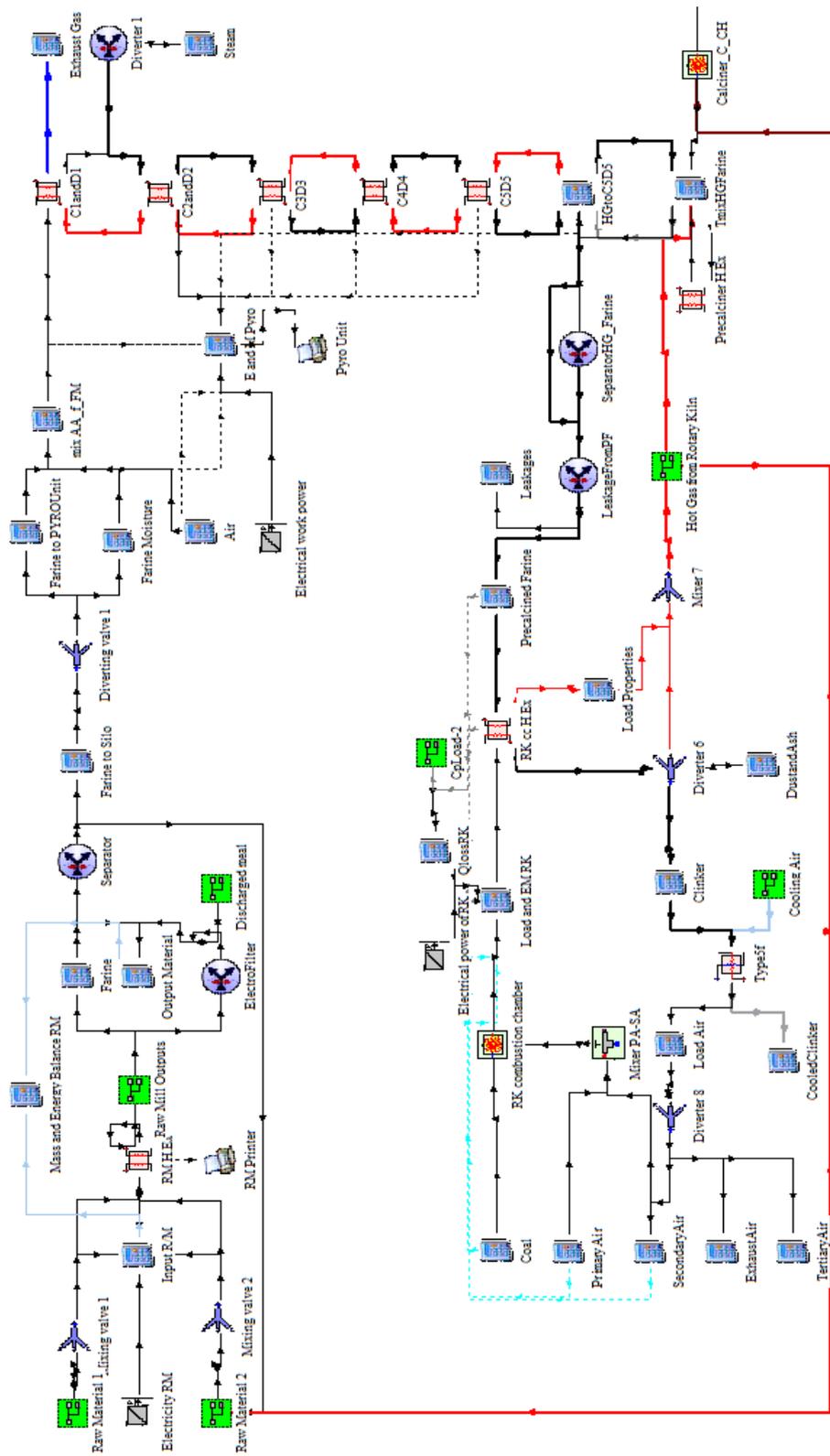
Figure 6.5 TRNSYS diagram of a conventional cement plant

It is important to specify the required variables for each component while creating a simulation studio. The user double clicks on the component icon to change the parameters, inputs, derivatives and view the outputs. A screen shot of the parameter window with tabs for the Input, Output, and Comment is shown in Figure 6.6.
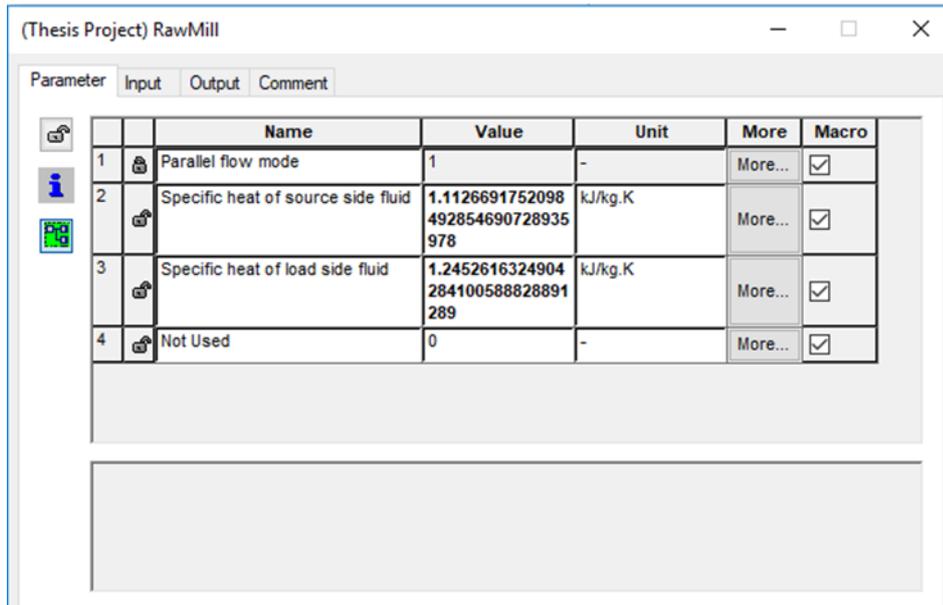
Figure 6.6 Parameters Window

Information flow occurs using a link between two components. By double-clicking on the link, the user can see the details of the link. To specify the connection between two components, the user connects the outputs of the first component to the required inputs of the second component. Additionally, users can only connect variables of the same dimension, i.e. 'temperature' to 'temperature of the same dimension'.

Raw materials, leaking air, hot gas from rotary burner and return material from raw mill are mixed using mixers. The mixture enters the raw mill and exchanges heat in the mill modeled by a heat exchanger. The electrical work power is supplied by a power conditioning component. A portion of the output is discharged using a fan. The other portion rests in the silo until being sucked by the preheating unit. With the aim of warming up to desired temperature, "farine" and the "moisture of farine" along with the "ambient air" enter the tower from top and the "hot gas from the

49

precalciner" enters the tower from the bottom of the tower. The tower is modeled using five counter-flow heat exchangers. The heated material exiting the fifth cyclone and the "hot gas from the kiln", and the hot gas, "tertiary air" from the cooler enter the precalciner chamber. The precalciner is modeled as a combination of a "combustion chamber", Type 426 from STEC library, and a heat exchanger. "Coal" is fed into the combustion chamber along with the "tertiary air". After being separated from the "leakages", using diverter, the "precalcined farine" that is the output of the precalciner chamber, continues its way to the rotary kiln. The rotary kiln is modeled as a combination of a combustion chamber, Type 426 from STEC library, and a heat exchanger as displayed in the Figure 6.7 [144]. The fuel burns in air incoming to the combustion chamber, then the precalcined farine is heated by the air inside the heat exchanger.
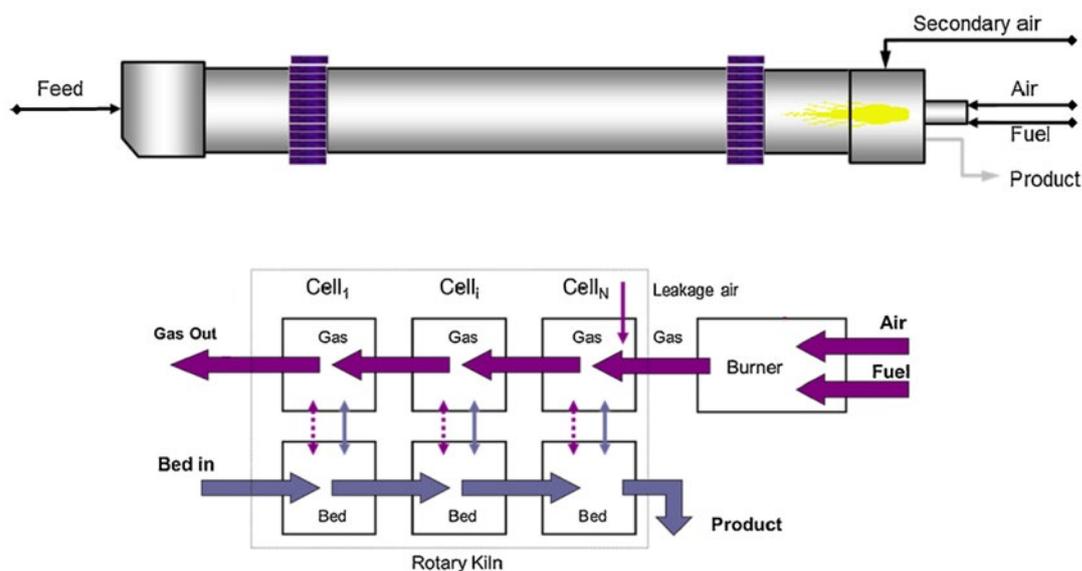
Figure 6.7 Model scheme of the counter current rotary kiln [144].

The mixer, Type 303 from STEC library, mixes "primary air" and "secondary air" exiting the cooler". "Coal" is fed into the combustion chamber burnt by primary and secondary air. The hot gas from the kiln is separated to three parts using the separator. A proportion of it moves to the raw mill, the other moves to the precalciner and the remaining moves away by a fan. The "clinker" is then cooled by the "cooling air"

supplied by the fans inside a cross-flow heat exchanger (both fluids mixed). Equation "cooled clinker" gives out the ultimate temperature of the cooled clinker. Equations "energy and mass balance" calculate the energy and mass balance at each time step. Utilized types of the components used in the model are listed in Table 6.1.

Table 6.1 List of the components in TRNSYS model

Name	Type	Note
Raw Materials	Equation	Showing input materials' flowrates and temperatures
Mixing valve 1	Type 649	Mixing input materials into a single mass flow
Mixing valve 2	Type 649	Mixing input materials into a single mass flow
Power of RM	Type 175b	Modeling the electrical charge of RM
Input RM	Equation	Calculating input temperatures and total energy
RM H.Ex	Type 5a	Heat exchange between the materials
RM Mixer	Type 11h	Mixing the outputs
Tmix RM	Equation	Calculating the mixture's temperature
Grit Separator	Type 11f	Splitting the outputs with a user-defined proportion
M and E RM	Equation	Calculating the mass and energy balances
Outnput RM	Equation	Calculating total output energy
Separator	Type 11f	Separating the return material form source output
Electrofilter	Type 11f	Separating steam form the load output
DM Fan	744	Blowing the discharged outputs away
Farine to the silo	Equation	Calculating the flowrate and temperature
Steam RM	Equation	Calculating the flowrate and temperature
DM RM	Equation	Calculating the flowrate and temperature
Diverting valve 1	647	Showing the farine moisture and farine

Table 6.1 (Continued)

Farine to PYRO	Equation	Calculating the flowrate and temperature
Farine Moisture	Equation	Calculating the flowrate and temperature
mix AA_FM	Equation	Calculating the mixture's properties
Ambient air	Equation	Calculating the flowrate and temperature
Power of Pyro	Type 175b	Modeling a power conditioning unit
Mixer 3	Type 649	Mixing the source flows of pyroprocessing unit
C_iD_i	Type 5b	Cyclone heat exchangers
Steam	Equation	Calculating the flowrate and temperature
Exhaust Gas	Equation	Calculating the flowrate and temperature
Diverter 1	Type 11f	Diverting the steam from farine
T_source2	Equation	Calculating the source temperature
T_S_HG	Equation	Calculating temperature of the source and HG
HG to C_5D_5	Equation	Calculating Hot Gas temperature
Calciner_C_Ch	Type 426	Combustion chamber of the precalciner
Precalciner	Type 5a	Heat exchange in the precalciner
TmixHGFarine	Equation	Calculating the mixture's temperature
HGfromFarine	Type 11f	Separating hot gas and precalcined farine
LeakageFromPF	Type 11f	Separating leakages and precalcined farine
PrecalcinedFarine	Equation	Calculating the flowrate and temperature
Coal	Equation	Calculating the flowrate and temperature
Primary Air	Equation	Calculating the flowrate and temperature
PA-SA	Type 303	Mixing Primary and Secondary Air
RKcomb.chamber	Type 426	Combustion chamber of the rotary kiln

Table 6.1 (Continued)

Load	Equation	Evaluating the combustion chamber's output
Electricity	Type 175b	Modeling the shaft work of the kiln
CpLoad	Equation	Calculating the specific heat of RK's load
RK cc H.Ex	Type 5b	Heat exchange in the RK
Load Properties	Equation	Calculating the flowrate and temperature
Diverter 3 and 4	Type 647	Diverting the outputs of RK cc H.Ex
HotGasRK	Equation	Calculating the flowrate and temperature
Diverter 3-2, 4_2	Type 11f	Splitting the hot gas output of RK
Discharging fan	Type744	Discharging the exhaust gases
HG from RK	Equation	Calculating the flowrate and temperature
Clinker	Equation	Calculating the flowrate and temperature
Supply Fan	Type 642	Providing cooling air
Cooling Air	Equation	Calculating the flowrate and temperature
Grate Cooler	Type 5f	Cooling the clinker
Load Air	Equation	Calculating the output air's properties
Diverter 5	Type 647	Splits the air load
SecondaryAir	Equation	Calculating the flowrate and temperature
TertiaryAir	Equation	Calculating the flowrate and temperature
ExhaustAir	Equation	Calculating the flowrate and temperature
CooledClinker	Equation	Calculating the flowrate and temperature

6.2.1   Types and Connections

6.2.1.1   Equations of Raw Materials

The first components are the equations inserted to identify the input mass flowrates, temperatures and specific heats, which are put in two macros in the TRNSYS model. Figure 6.8 shows an equation window with input and output boxes. The input values of mass flowrates, specific heats, and temperatures used in this section are constant and have been obtained from [30] as represented in Table A.1. Here, for calculating the outputs using input values, equations can be defined. The sensible heat of inputs are calculated by Equation (5.7). Table 6.2 displays the output connections of these equations.
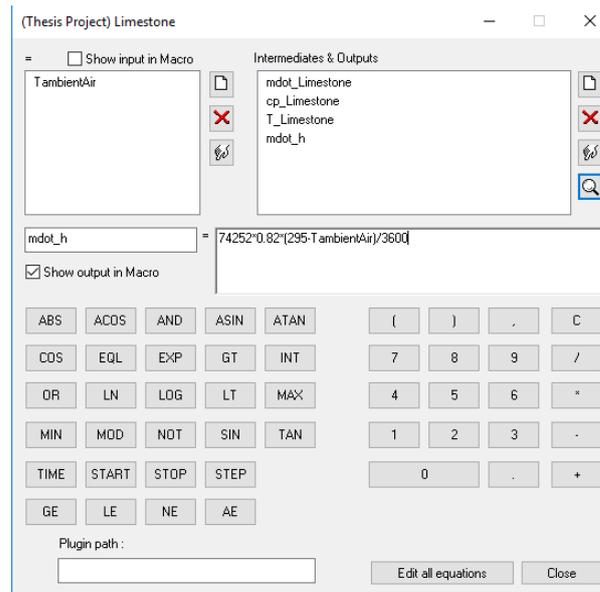
Figure 6.8 An equation window

$T_{ambient}$ is considered constant and equal to 290K. Thus, fourteen constant input equations are inserted into the model. Mass flowrates and temperature outputs of the equations are inputs for the mixers.

54

Table 6.2 Material equations' output

Limestone Equation Output	To	Input
Mass flowrate of limestone	Mixing valve 1	Flowrate at Inlet-1
Temperature of limestone	Mixing valve 1	Temperature at Inlet-1
Mass flowrate of Dust	Mixing valve 2	Flowrate at Inlet-1
Temperature of Dust	Mixing valve 2	Temperature at Inlet-1

The rest of the equations of raw materials are connected to the inputs of mixing valves in the same way as presented in the Table 6.2. Limestone, moisture of limestone, marl, moisture of marl, clay, moisture of clay, iron ore, and moisture of iron ore are inside the macro and get mixed up in the valve 1. Bauxite, moisture of bauxite, gas from RK, return material from separator, leaking air and dust are inside the macro_2 and get mixed up in valve 2.

6.2.1.2   Mixing valves 1 and 2

Each mixing valve can combine up to 100 individual streams into a single outlet mass flow. Valve 1, mixes 8 inputs and valve 2 mixes the remaining. In the Table 6.3 and 6.4, output connections of both of the valves are shown. Following equations indicate the mass flowrate of each mixing valve's output:

$$\dot{m}_{valve1\ output} = \sum \dot{m}_i = \dot{m}_l + \dot{m}_{ml} + \dot{m}_m + \dot{m}_{mm} + \dot{m}_c + \dot{m}_{cm} + \dot{m}_{io} + \dot{m}_{iom} \qquad (6.1)$$

$$\dot{m}_{valve2\ output} = \sum \dot{m}_i = \dot{m}_b + \dot{m}_{mb} + \dot{m}_g + \dot{m}_r + \dot{m}_{la} + \dot{m}_d \qquad (6.2)$$

where subscripts l, ml, m, mm, c, cm, io, iom, b, mb, g, r, la, and d stand for limestone, moisture of limestone, marl, moisture of marl, clay, moisture of clay, iron ore, moisture of iron ore, bauxite, moisture of bauxite, gas from RK, return material from separator, leaking air, and dust, respectively.

Table 6.3 Mixing valve 1 output connections

Mixing valve 1 output	To	Input
Outlet Temperature	RM H.Ex	Source side inlet temperature
Outlet Flowrate	RM H.Ex	Source side flow rate
Outlet Temperature	Input RM	Temp1
Outlet Flowrate	Input RM	mdotin1

Table 6.4 Mixing valve 2 output connections

Mixing valve 2 output	To	Input
Outlet Flowrate	RM H.Ex	Source side flow rate
Outlet Flowrate	Input RM	Mdotin2

Since the specific heats of the inputs of the mixing valve 2, are not the same value, the temperature of mixture is calculated using Equation (5.10):

$$T_{mix2} = \frac{(\dot{m}_b c_b T_b) + (\dot{m}_{mb} c_{mb} T_{mb}) + (\dot{m}_g c_g T_g) + (\dot{m}_r c_r T_r) + (\dot{m}_{la} c_{la} T_{la}) + (\dot{m}_d c_d T_d)}{(\dot{m}_b c_b) + (\dot{m}_{mb} c_{mb}) + (\dot{m}_g c_g) + (\dot{m}_r c_r) + (\dot{m}_{la} c_{la}) + (\dot{m}_d c_d)}$$
$$\approx 518.925 \tag{6.3}$$

6.2.1.3   Electricity RM

This component is used to generate the required power for the raw mill unit, which is 3250kW according to the Table A.1. Figure 6.9 displays the input tab of this component.
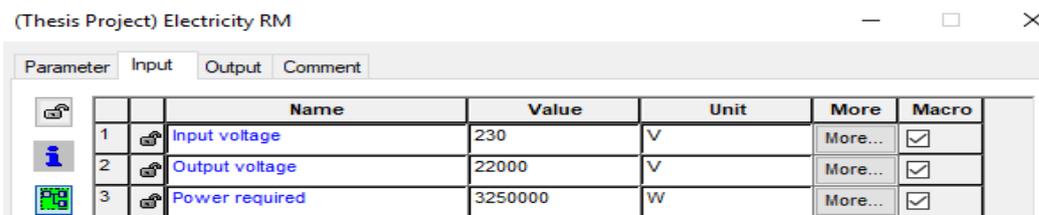
Figure 6.9 Electricity RM component inputs

6.2.1.4 Input RM

This equation is linked to the input materials of the raw mill unit. It also calculates the input energy to the unit as shown in Figure 6.10.
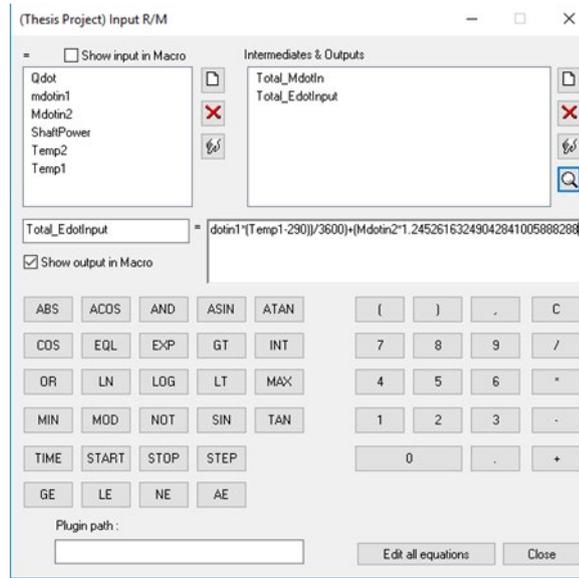
Figure 6.10 Input RM equation

6.2.1.5 Raw mill heat exchanger

A parallel flow heat exchanger (RM H.Ex) is used in this section. The output of mixing valve 1 is the cold side (source) material that enters the heat exchanger and the output flow of mixing valve 2 is the hot side (load) material. The source fluid is warmed up by the hot side fluid. Specific heat of source and load side fluids are calculated using Equation (5.11) with $T_{ambient}$=290K. Details of this component are listed in Table 6.5 and 6.6.

Since the temperatures of the inputs of mixing valve 1 are identical, Equation (5.11) reduces to:

$$c_{mix1} = \frac{((\dot{m}_l c_l) + (\dot{m}_{ml} c_{ml}) + (\dot{m}_m c_m) + (\dot{m}_{mm} c_{mm}) + (\dot{m}_c c_c) + (\dot{m}_{cm} c_{cm}) + (\dot{m}_{io} c_{io}) + (\dot{m}_{iom} c_{iom})}{\dot{m}_l + \dot{m}_{ml} + \dot{m}_m + \dot{m}_{mm} + \dot{m}_c + \dot{m}_{cm} + \dot{m}_{io} + \dot{m}_{iom}}$$

$$\approx 1.1127 \tag{6.4}$$

And the specific heat of the second mixture is:

$$c_{mix2} = \frac{(\dot{m}_b c_b (T_b - 290)) + (\dot{m}_{mb} c_{mb} (T_{mb} - 290)) + (\dot{m}_g c_g (T_g - 290)) + (\dot{m}_r c_r (T_r - 290)) + (\dot{m}_{la} c_{la} (T_{la} - 290)) + (\dot{m}_d c_d (T_d - 290))}{(\dot{m}_b + \dot{m}_{mb} + \dot{m}_g + \dot{m}_r + \dot{m}_{la} + \dot{m}_d)(T_{mix} - 290)}$$
$$\approx 1.2453 \tag{6.5}$$

Overall heat transfer coefficient (UA) of exchanger is related to its thermal performance. This coefficient is calculated as:

$$\dot{Q} = UA\Delta T_m, \tag{6.6}$$

$$\Delta T_m = \frac{\left(T_{h_2} - T_{c_2}\right) - \left(T_{h_1} - T_{c_1}\right)}{\ln\left(\dfrac{T_{h_2} - T_{c_2}}{T_{h_1} - T_{c_1}}\right)} \tag{6.7}$$

where $\dot{Q}$ is heat transfer rate of the heat exchanger, and ΔT_m is the log mean temperature difference. In the equations, the subscripts c_1, c_2, h_1, and h_2 stand for input cold fluid, output cold fluid, input hot fluid, and output hot fluid, respectively.

Table 6.5 Parameters and inputs of RM heat exchanger

Parameter	Value	Unit
Specific heat of source side fluid	1.1127	kJ/kgK
Specific heat of load side	1.2453	kJ/kgK
Input	**Value**	**Unit**
Load side inlet temperature	518.9245	K
Overall heat transfer coefficient of exchanger	80000	kJ/hK

Table 6.6 Raw Mill Heat Exchanger Outputs

RM H.Ex output	To	Input
Source side outlet temperature	Tmix RM	TSource
Source side flow rate	Tmix RM	MdotSource
Source side flow rate	RM Mixer	Flow rate at inlet 1

Table 6.6 (Continued)

Load side outlet temperature	Tmix RM	TLoad
Load side flow rate	Tmix RM	MdotLoad
Load side flow rate	RM Mixer	Flow rate at inlet 2
Heat transfer rate	Printer	RM Heat transfer

6.2.1.6   RM Mixer

The mixer, mixes the source and load side fluids to get a homogenized mixture. Table 6.7 indicates the outlet connections of it.

Table 6.7 RM Mixer Outputs

RM Mixer output	To	Input
Outlet flow rate	Grit Separator	Inlet flow rate

6.2.1.7 T_{mix} RM

The equation calculates the temperature of mixture using (5.10). The equation window and output connections are shown in Figure 6.11 and Table 6.8, respectively.

Table 6.8 T_{mix} equation outputs

RM H.Ex output	To	Input
T_{mix} RM	Grit Separator	Inlet temperature
T_{mix} RM	Online Plotter	T_{mix} RM
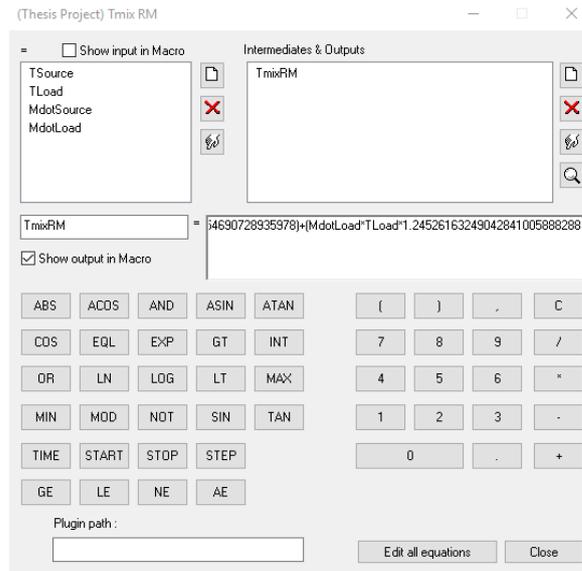
Figure 6.11 T$_{mix}$ equation window

6.2.1.8 Grit separator

According to the raw mill output mass flowrates adopted from [30], represented in Table A.2, the input control signal value is calculated. Table 6.9 shows the outputs of the separator.

$$Control\ Signal = \frac{\dot{m}_{farine}}{\dot{m}_{Total}} \simeq 0.6498 \tag{6.8}$$

Table 6.9 Grit separator outputs

Grit separator output	To	Input
Temperature at outlet 1	ElectroFilter	Inlet temperature
Flow rate at outlet 1	ElectroFilter	Inlet flow rate
Temperature at outlet 2	Farine	Temp_Farine
Flow rate at outlet 2	Farine	mdot_Farine

6.2.1.9   Farine

This equation calculates the sensible heat of farine that is one of the products of raw mill unit and transfers the farine's temperature and mass flowrate to the other units. Figure 6.12 and Table 6.10 show the details of this equation.
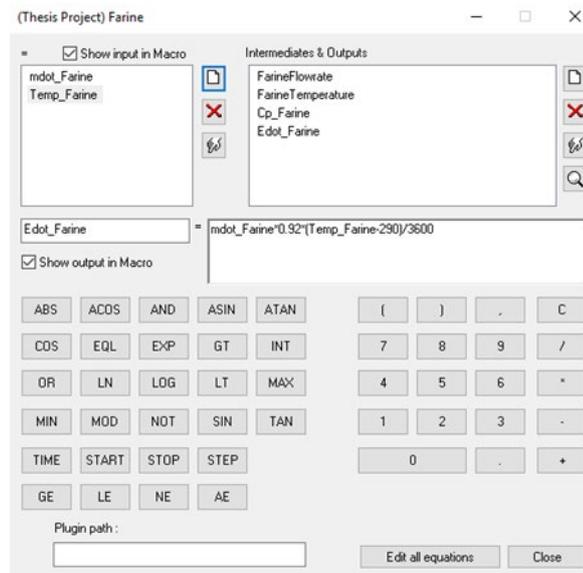
Figure 6.12 "Farine" equation

Table 6.10 "Farine" outputs

Farine output	To	Input
Farine Temperature	Separator	Inlet temperature
Farine Flowrate	Separator	Inlet flow rate
Farine Flowrate	Output Material	mdotFarine
Edot_Farine	Output Material	Edot_Farine

6.2.1.10   Separator

This component operates similar to the Grit Separator. The input control signal value is calculated and the details of this component are displayed in Table 6.11.

$$Control\ Signal = \frac{\dot{m}_{Return\ material}}{\dot{m}_{farine}} \simeq 0.1671 \tag{6.9}$$

Table 6.11 Separator outputs

Separator output	To	Input
Temperature of Farine2	Diverting valve1	Farine2 temperature
Flow rate of Farine2	Diverting valve1	Farine2 flow rate
Temperature of Return Material	Return Material	RM temperature
Flow rate of Return Material	Return Material	RM flow rate

6.2.1.11 Diverting valve 1

This valve splits the farine into three mass flows. Table 6.12 displays the output connections of this component. The fractions are calculated by the inlet mass flowrate values of the pyroprocessing tower from Table A.3.

$$Fraction\ of\ Flow\ to\ Outlet\ \text{-}1 = \frac{\dot{m}_{Farine\ to\ PYRO\ Unit}}{\dot{m}_{farine2}} \simeq 0.9572$$

$$Fraction\ of\ Flow\ to\ Outlet\ \text{-}2 = \frac{\dot{m}_{Moisture\ of\ Farine}}{\dot{m}_{farine2}} \simeq 0.0312$$

$$Fraction\ of\ Flow\ to\ Outlet\ \text{-}3 = \frac{\dot{m}_{FarineSilo}}{\dot{m}_{farine2}} \simeq 0.0116 \tag{6.10}$$

Table 6.12 Diverting valve outputs

Diverting valve 1 output	To	Input
Outlet Temperature-1	Farine to PYRO	Temp Farine2
Outlet Flowrate-1	Farine to PYRO	Mdot Farine2
Outlet Temperature-2	Farine Moisture	T_MF
Outlet Flowrate-2	Farine Moisture	Mdot_MF
Outlet Temperature-3	Farine Silo	FS temperature
Outlet Flowrate-3	Farine Silo	FS flow rate

6.2.1.12 Electro Filter

This component operates like the previous component. The output connections of it are listed in Table 6.13. Control signal input of this component is calculated as:

$$Control\ Signal = \frac{\dot{m}_{steam}}{\dot{m}_{Total} - \dot{m}_{farine}} \simeq 0.1712 \tag{6.11}$$

Table 6.13 Electro Filter outputs

Electro Filter output	To	Input
Temperature of Discharged Material	DM RM	DM temperature
Flow rate of Discharged Material	DM RM	DM flowrate
Temperature of Steam	Steam RM	Steam temperature
Flow rate of Steam	Steam RM	Steam flowrate

6.2.1.13 Steam RM and Discharged Materials RM

These equations are the outputs of Electro Filter. The output connections of them are represented in Table 6.14 and 6.15

Table 6.14 Steam RM outputs

Electro Filter output	To	Input
Temperature of Steam	Output Material	Steam temperature
Flow rate of Steam	Output Material	Steam flowrate
Sensible heat of Steam	Output Material	Edot_Steam

Table 6.15 Discharged Materials RM outputs

Discharged Materials RM output	To	Input
Temperature of DM RM	Output Material	DM RM temperature
Flow rate of DM RM	Output Material	DM RM flowrate
Flow rate of DM RM	DM Fan	Outlet Flowrate

Table 6.15 (Continued)

Sensible heat of DM RM	Output Material	Edot_ DM RM

6.2.1.14 Output Material and Mass and Energy Balance RM (M. and E. RM)

These equations calculate the total mass and energy rates. Table 6.16 and 6.17 present the output connections of them.

Table 6.16 Output Material equation outputs

Output Material equation output	To	Input
Total_mdotOutput	M. and E. RM	mdotOut
Total_EdotOutput	M. and E. RM	EdotOut

Table 6.17 Mass and Energy Balance RM outputs

M. and E. RM equation output	To	Input
Mass flowrate Balance	Printer	MdotT_RM
Energy Balance	Printer	EdotT_RM

6.2.1.15 Farine to PYRO Unit and Moisture of Farine

These equations calculate the sensible heat of the farine and moisture of farine entering the pyroprocesing unit. Specific heats of them are obtained from Table A.3. The output connections of them are listed in the Table 6.18.

Table 6.18 Farine to PYRO Unit and Moisture of Farine outputs

Farine to PYRO Unit Eqn. output	To	Input
mdot_FarineInPYRO	mix AA_f_FM	Mdot_Farine2
T_FarineInPYRO	mix AA_f_FM	T_Farine2
c_p_ FarineInPYRO	mix AA_f_FM	c_pFarine2

Table 6.18 (Continued)

Farine to PYRO Unit Eqn. output	To	Input
Mdot Moisture of Farine	mix AA_f_FM	Mdot_MF
T Moisture of Farine	mix AA_f_FM	Temp_ MF
c_p_ Moisture of Farine	mix AA_f_FM	c_p_ MF

6.2.1.16 Ambient Air

The properties of the ambient air that leaks into the pyroprocessing tower are in the Table A.3. This equation has constant outputs that are inputs for the other units as represented in the Figure 6.13 and Table 6.19.
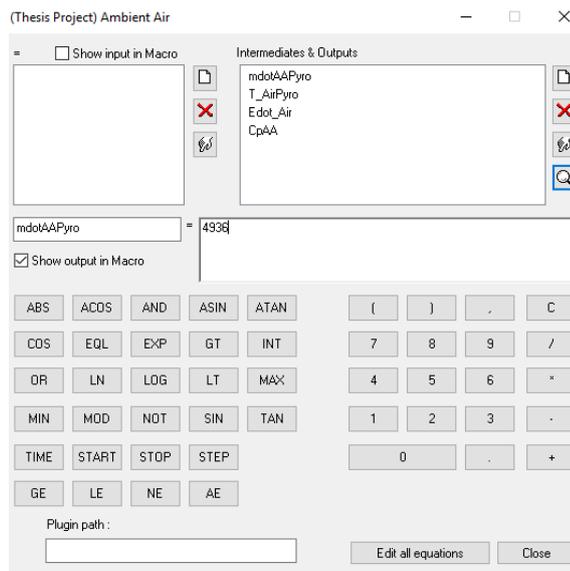
Figure 6.13 Ambient Air equation

Table 6.19 Ambient Air equation outputs

Ambient Air Equation output	To	Input
Mdot AA Pyro	mix AA_f_FM	Mdot_AA
T Air Pyro	mix AA_f_FM	Temp_ AA
c_p_ AA	mix AA_f_FM	c_p_ AA

6.2.1.17 mix AA_f_FM

This equation calculates the temperature and specific heat of the source mixture of the pyroprocessing unit by equations (5.10) and (5.11). The equation window and the output connections of this equation are displayed in Figure 6.14 and Table 6.20.
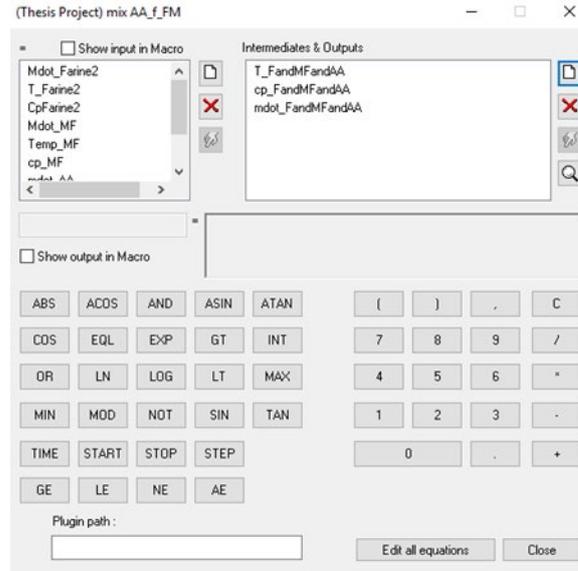
Figure 6.14 mix AA_f_FM equation

Table 6.20 mix AA_f_FM equation

mix AA_f_FM equation output	To	Input
T_FandMFandAA	C_1 and D_1	Source side inlet temperature
mdot_FandMFandAA	C_1 and D_1	Source side flow rate
Farine to PYRO Unit Eqn. output	**To**	**Parameter**
c_p_FandMFandAA	C_1 and D_1	Specific heat of source side fluid

6.2.1.18   Type 175b

This component is used to generate the required electrical power for the pyroprocessing unit, which is 5000kW according to the Table A.3.

Figure 6.15 Type 175b

6.2.1.19 C_1 and D_1

Since the flow of the hot gas and the source mixture move in the opposite directions, each cyclone and its corresponding duct have been modeled as a countercurrent heat exchanger. The preheater tower is a multi-stage five-cyclone pyroprocessing unit. The specific heat of the source and load side fluids are adopted from [30], Table A.3, and the heat exchange rate in this cyclone is calculated using Table A. 8, represented in Table A. 9. The net heat exchange rate in the first cyclone is 3,169.84 kW. According to the Equation (6.6), the overall heat transfer coefficient of the exchanger is calculated. The input and parameter values and output connections are shown in Table 6.21.

Table 6.21 Parameters and inputs of C_1 and D_1 heat exchanger

Parameter	Value	Unit
Specific heat of source side fluid	1.253	kJ/kgK
Specific heat of load side	1.55	kJ/kgK
Input	**Value**	**Unit**
Overall heat transfer coefficient of exchanger	52175	kJ/hK
C_1 and D_1 output	**To**	**Input**
Source side outlet temperature	TSource2	TS1

Table 6.21 (Continued)

Source side flow rate	TSource2	mdotS1
Source side outlet temperature	Diverter 1	InletTemp.
Source side flow rate	Diverter 1	Inlet flowrate
Source side outlet temperature	TSource2	TS1
Source side flow rate	TSource2	mdotS1
Load side outlet temperature	Exhaust Gas	mdotEG
Load side flow rate	Exhaust Gas	ToutEG
Heat transfer rate	E and M Pyro	Edot_C1D1

6.2.1.20 Exhaust Gas

This equation gives information about the outlet gas of the preheating tower. Specific heat coefficient of it is adopted from Table A.4. Figure 6.16 shows the equation window and Table 6.22 represents the outlet connections of this component.
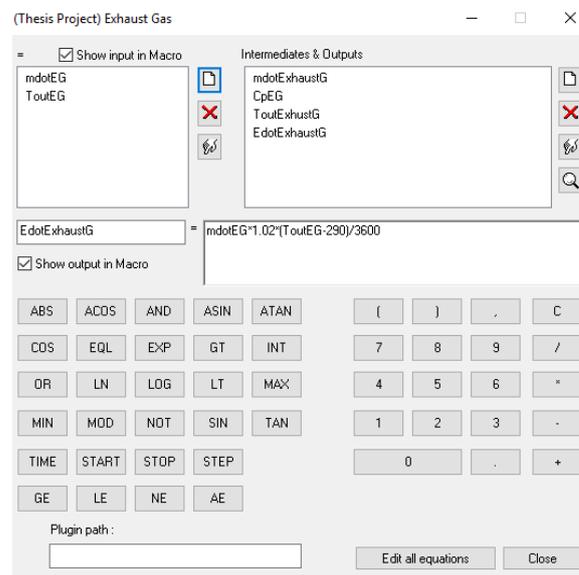
Figure 6.16 Exhaust Gas equation window

Table 6.22 Exhaust Gas equation outputs

Exhaust Gas Eqn. output	To	Input
mdotExhaustG	E and M Pyro	Mdot_EG
ToutExhaustG	E and M Pyro	T_EG

6.2.1.21   Diverter 1

This component splits farine's steam produced by evaporation of the moisture of farine in the first cyclone from the source fluid of the C_1 and D_1. The control signal value for this component is calculated using the output mass flowrates of the preheating tower derived from Table A.4. Moreover, Table 6.23 shows the output connections of this component.

$$Control\ Signal = \frac{\dot{m}_{steam}}{\dot{m}_{FarinetoPYRO} + \dot{m}_{FarinetoMoisture} + \dot{m}_{ambient}} \simeq 0.0707 \qquad (6.12)$$

Table 6.23 Diverter 1 outputs

Diverter 1 output	To	Input
Temperature at outlet 1	TSource2	TS2
Flow rate at outlet 1	TSource2	mdotS2
Temperature at outlet 2	Steam	Tsteam
Flow rate at outlet 2	Steam	mdotS

6.2.1.22   Steam

Specific heat coefficient and mass flowrate of steam are given in Table A.4. Steam equation calculates the sensible heat of it using the inputs as displayed in the Figure 6.17. Table 6.24 shows the outlet connections of this equation.

Table 6.24 Steam equation outputs

Steam equation output	To	Input
mdotSteam	E and M Pyro	MdotSteam2
EdotSteam	E and M Pyro	EdotSteam2
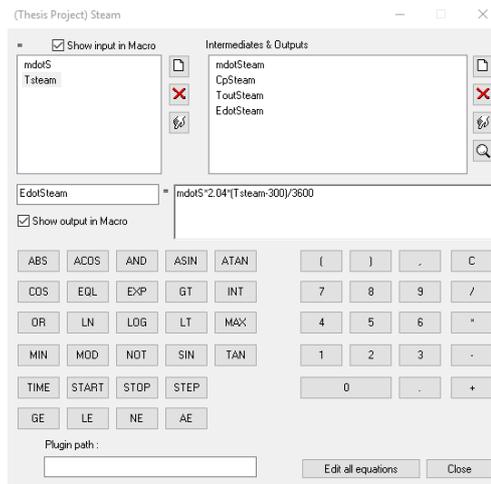
Figure 6.17 Steam equation

6.2.1.23 Temperature of Source$_2$ (TSource2)

This equation calculates the sensible heat of the source fluid entering C_2 and D_2 (source$_2$), after being separated from the steam. As a result, temperature of source$_2$ is calculated as shown in Figure 6.18, and Table 6.25 shows the outlet connections of this equation.

Table 6.25 TSource2 equation outputs

TSource2" equation output	To	Input
T_Source2	C_2 and D_2	Source side inlet temperature
mdot_Source2	C_2 and D_2	Source side flow rate
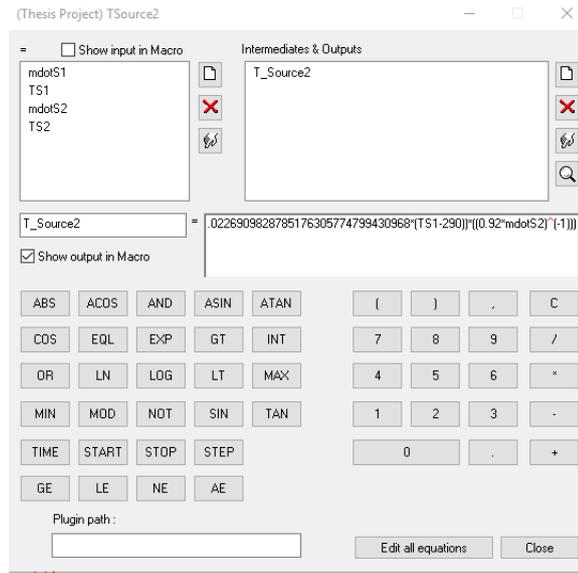
Figure 6.18 TSource2 equation

6.2.1.24 C₂ and D₂

Similar to the heat exchanger "C_1 and D_1", since the flow of the hot gas and the source mixture move in the opposite directions, second cyclone and its corresponding duct are modeled as a countercurrent heat exchanger. The rate of heat exchange in this cyclone is adopted from Table A. 9. The net heat exchange rate in this cyclone is 4,810.023 kW. According to the Equation (6.6), overall heat transfer coefficient of the exchanger is calculated. The inputs, parameter values and output connections are represented in Table 6.26.

Table 6.26 Parameters and inputs of C_2 and D_2 heat exchanger

Parameter	Value	Unit
Specific heat of source side fluid	0.92	kJ/kgK
Specific heat of load side	1.02	kJ/kgK
Input	**Value**	**Unit**
Overall heat transfer coefficient	59227.6	kJ/hK

Table 6.26 (Continued)

C_2 and D_2 output	To	Input
Source side outlet temperature	T_HG_S	T_S2to3
Source side flow rate	T_HG_S	m_S2to3
Load side outlet temperature	C_1 and D_1	Load side inlet temperature
Load side flow rate	C_1 and D_1	Load side flow rate
Heat transfer rate	E and M Pyro	Edot_C2D2

6.2.1.25   T_HG_S

This equation transfers the information of source side fluid to "C_3 and D_3" and calculates the temperature of the load fluid entering "C_2 and D_2" that has undergone several chemical reactions, as shown in Figure 6.19. In addition, Table 6.27 displays the outlet connections of this equation.

Table 6.27 T_HG_S equation outputs

T_HG_S equation output	To	Input
T_HGin2	C_2 and D_2	Load side inlet temperature
mdotHotGasinCD2	C_2 and D_2	Load side flow rate
T_Farine3	C_3 and D_3	Source side inlet temperature
mdotFarine3	C_3 and D_3	Source side flow rate
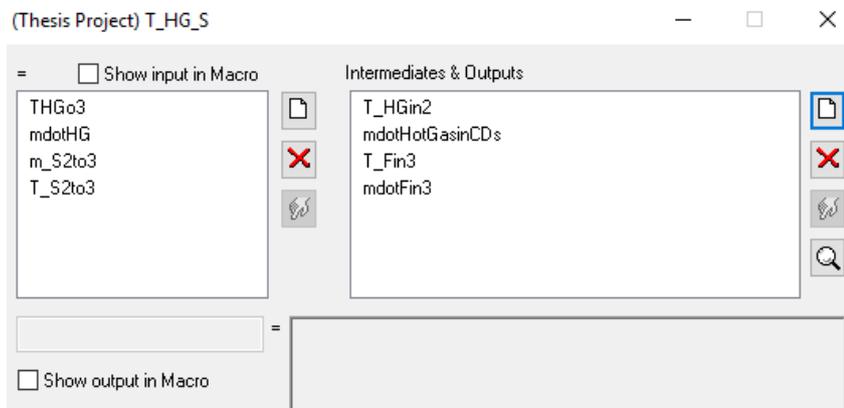
Figure 6.19 T_HG_S equation window

6.2.1.26 C_3 and D_3

Similar to heat exchanger "C_1 and D_1" and "C_2 and D_2", the third cyclone and its corresponding duct are modeled as a countercurrent heat exchanger. The essential data used to model the component are provided in Table A.3 and Table A. 9. The net heat exchange rate in this cyclone is 7,873.803 kW. The overall heat transfer coefficient of the exchanger is calculated by Equation (6.6). The inputs, parameter values and output connections of this component are represented in Table 6.28.

Table 6.28 Parameters and inputs of C_3 and D_3 heat exchanger

Parameter	Value	Unit
Specific heat of source side fluid	0.92	kJ/kgK
Specific heat of load side	1.55	kJ/kgK
Input	**Value**	**Unit**
Overall heat transfer coefficient	193396.1	kJ/hK
C_3 and D_3 output	**To**	**Input**
Source side outlet temperature	C_4 and D_4	Source side outlet temperature
Source side flow rate	C_4 and D_4	Source side flow rate
Load side outlet temperature	T_HG_S	THGo3
Load side flow rate	T_HG_S	mdotHG
Heat transfer rate	E and M	Edot_C3D3

6.2.1.27 C_4 and D_4

Similar to the previous heat exchangers "C_i and D_i", the fourth cyclone and its corresponding duct are modeled as a countercurrent heat exchanger. The net heat exchange rate in this cyclone is 8,861.357 kW. According to the Equation (6.6), overall heat transfer coefficient of the exchanger is calculated. The input and parameter values and output connections are shown in Table 6.29.

Table 6.29 Parameters and inputs of C_4 and D_4 heat exchanger

Parameter	Value	Unit
Specific heat of source side fluid	0.92	kJ/kgK
Specific heat of load side	1.55	kJ/kgK
Input	**Value**	**Unit**
Overall heat transfer coefficient	172387.34	kJ/hK

Table 6.29 (Continued)

C_4 and D_4 output	To	Input
Source side outlet temperature	C_5 and D_5	Source side outlet temperature
Source side flow rate	C_5 and D_5	Source side flow rate
Load side outlet temperature	C_3 and D_3	Load side inlet temperature
Load side flow rate	C_3 and D_3	Load side flow rate
Heat transfer rate	EandM Pyro	Edot_C4D4

6.2.1.28 C_5 and D_5

The fifth cyclone and its corresponding duct are modeled as a countercurrent heat exchanger. According to the Equation (6.6), the overall heat transfer coefficient of the exchanger is calculated. The input and parameter values and output connections are shown in Table 6.30.

Table 6.30 Parameters and inputs of C_5 and D_5 heat exchanger

Parameter	Value	Unit
Specific heat of source side fluid	0.92	kJ/kgK
Specific heat of load side	1.55	kJ/kgK
Input	**Value**	**Unit**
Overall heat transfer coefficient	180000	kJ/hK
C_5 and D_5 output	**To**	**Input**
Source side outlet temperature	HGtoC$_5$D$_5$	TFarineC5D5
Source side flow rate	HGtoC$_5$D$_5$	mdotFarineC5D5
Load side outlet temperature	C_4 and D_4	Load side inlet temperature

Table 6.30 (Continued)

Load side flow rate	C_4 and D_4	Load side flow rate
Heat transfer rate	EandM Pyro	Edot_C5D5

6.2.1.29 Hot Gas to C₅D₅

This equation passes information of source side fluid to the Separator of HG and Farine (S_HG_F) and calculates the temperature of the hot gas entering C_5 and D_5, as shown in Table 6.17. In addition, Table 6.31 shows the outlet connections of this equation.
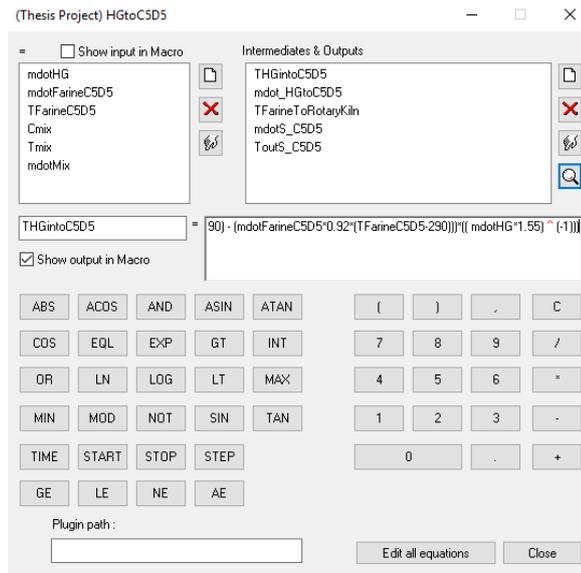
Figure 6.20 Hot Gas to C_5D_5 equation window

Table 6.31 Hot Gas to C_5D_5 equation outputs

Hot Gas to C₅D₅ equation output	To	Input
THGintoC5D5	C_5 and D_5	Load side inlet temperature
mdot_HGtoC5D5	C_5 and D_5	Load side flow rate
ToutS_C5D5	T_{mix}HGFarine	ToutFCD5
mdotS_C5D5	T_{mix}HGFarine	mdotFCD5

Table 6.31 (Continued)

THGintoC5D5	E and M Pyro	THG
mdot_HGtoC5D5	E and M Pyro	MHG
TFarineToRotaryKiln	LeakageFromPF	Source side flow rate

6.2.1.30   Mass and Energy Balance RM Pyroprocessing Tower

This equation calculates the energy rate and mass balances of the pyroprocessing unit, as shown in Figure 6.21. Moreover, Table 6.32 shows the outlet connections of this equation.
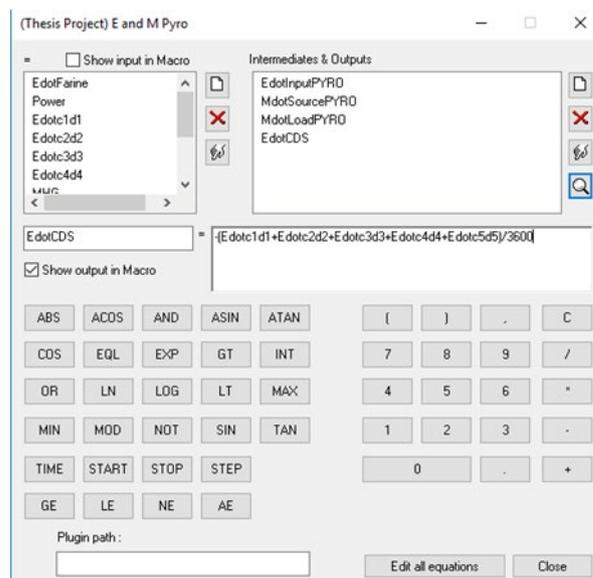
Figure 6.21 E and M Pyro equation

Table 6.32 E and M Pyro equation outputs

E and M Pyro equation output	To	Input
EdotInputPYRO	Printer	EdotInputPYRO
EdotCDs	Printer	EdotCDs
MdotSourcePYRO	Printer	MdotSourcePYRO
MdotLoadPYRO	Printer	MdotLoadPYRO

6.2.1.31 Calciner_C_Ch

This component is the combustion chamber of the precalciner and describes an adiabatic combustion chamber for fuels. This model can operate in two modes, in the first case, the coal is burnt and the outlet temperature of the chamber is the output. However, in the second mode, for a given outlet temperature the required fuel mass flow rate is calculated . The fuel used in this model is coal. The user specifies the lower heating value and the mass ratio of the fuel elements in parameter tab of the proforma window, as demonstrated in Figure 6.22. The user obtains fuel elements of the coal consumed in the rotary kiln from Table A.5, which are considered the same as the coal consumed in precalcination unit. The output connections of this component are displayed in the Table 6.33. 60% of the fuel mass flowrate consumed in the rotary kiln is consumed in the precalciner that is the component's input value as shown in Figure 6.23, thus:

$$\dot{m}_{precalciner\ fuel} = 0.6\dot{m}_{RK\ fuel}, \tag{6.13}$$

$$\dot{m}_{precalciner\ fuel} = 0.6 \times 7200 = 4320 \ (\text{kg/h}) \tag{6.14}$$

Mass ratio of each content of the coal is calculated as:

$$mass\ ratio = \frac{\dot{m}_{each\ content}}{\dot{m}_{Total}} \tag{6.15}$$

Figure 6.22 Parameter tab of Calciner_C_CH
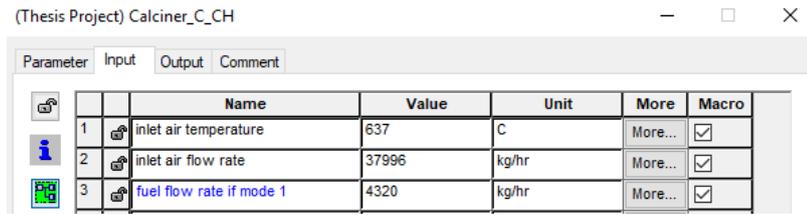
Figure 6.23 Input tab of Calciner_C_CH

Table 6.33 Calciner_C_Ch outputs

Calciner_C_Ch output	To	Input
Outlet temperature	TmixHGFarine	ToutCombustion
Outlet mass flow combustion air	TmixHGFarine	MoutCombustion
Outlet enthalpy	TmixHGFarine	HcombustionAir

6.2.1.32   T$_{mix}$ HG and Farine

This equation calculates the properties of the mixture of farine and hot gas coming from rotary kiln. Furthermore, this equation passes through the information of calciner combustion chamber to the prementioned heat exchanger, as shown in Figure 6.24. In addition, Table 6.34 shows the outlet connections of this equation.
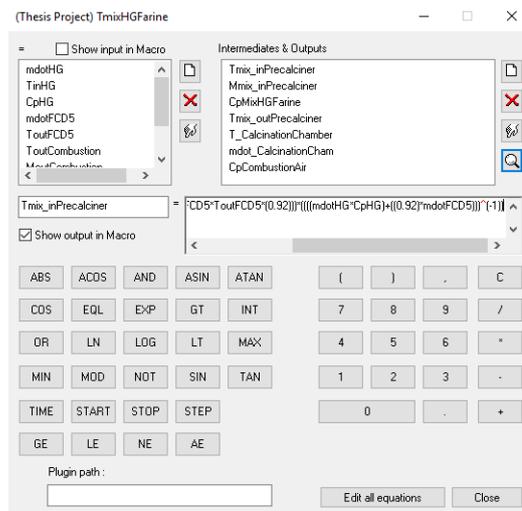
Figure 6.24 T$_{mix}$ HG and Farine equation

78

Table 6.34 T_{mix} HG and Farine equation outputs

T_{mix}HG and Farine equation output	To	Input
Tmix_inPrecalciner	Precalciner H.Ex	Source side inlet temperature
Mmix_inPrecalciner	Precalciner H.Ex	Source side flow rate
Tmix_inPrecalciner	HGtoC5D5	Tmix
Mmix_inPrecalciner	HGtoC5D5	mdotMix
CpMixHGFarine	HGtoC5D5	Cmix
Mmix_inPrecalciner	SeparatorHG_Farine	Inlet flow rate
T_CalcinationChamber	Precalciner H.Ex	Load side inlet temperature
mdot_CalcinationCham	Precalciner H.Ex	Load side flow rate
Tmix_outPrecalciner	HGtoC5D5	Tmix
T_{mix}HG and Farine equation output	**To**	**Parameter**
CpMixHGFarine	Precalciner H.Ex	Specific heat of source side
CpCombustionAir	Precalciner H.Ex	Specific heat of load side

6.2.1.33   Precalciner H.Ex

A parallel flow heat exchanger is used to model the heat exchange between hot gas-farine mixture and combustion air. Here, the mixture undergoes chemical and physical changes being exposed to the combustion air. Table 6.35 shows the output connections of this unit.

Table 6.35 Precalciner H.Ex outputs

Precalciner H.Ex output	To	Input
Source side outlet temperature	TmixHGFarine	TmixoutPrecalciner

6.2.1.34 Separator HG_Farine

This separator is used to separate the mixture of farine and hot gas which were precalcined in the precalcination unit. Table 6.36 demonstrates the outputs of this component. Control signal of this component is calculated as:

Table 6.36 Separator HG_Farine outputs

Separator HG_Farine output	To	Input
Flow rate at outlet 2	HGtoC5D5	mdotHG
Flow rate at outlet 1	TmixHGFarine	LeakageFromPF

6.2.1.35 Diverter of Leakage from PF

This diverter is used to split the farine into two fluids precalcined farine and leakages. The outputs of this component is presented in Table 6.37. Using the information presented in Table A.3 and Table A.4, the control signal of this component is calculated as:

$$Control\ Signal = \frac{\dot{m}_{Precalcined\ farine}}{\dot{m}_{Farine\ to\ PYRO\ Unit} + \dot{m}_{Moisture\ of\ Farine} + \dot{m}_{Ambient\ Air} - \dot{m}_{Steam} - \dot{m}_{hot\ gas}} \simeq 0.816$$

(6.16)

Table 6.37 Diverter of Leakage from PF outputs

Diverter of Leakage from PF output	To	Input
Flow rate at outlet 1	Leakages	mdotLeakage
Temperature at outlet 1	Leakages	Tleakages
Flow rate at outlet 2	Precalcined Farine	mdotPF
Temperature at outlet 2	Precalcined Farine	TPF

6.2.1.36 Precalcined Farine

This equation transfers the temperature and mass flowrate values of the precalcined farine to the rotary kiln heat exchanger, RK cc H.Ex, and Table 6.38 calculates the sensible energy of it. Figure 6.25 shows the equation window and represents the outlet connections of this equation.

Table 6.38 Precalcined Farine equation outputs

Precalcined Farine equation output	To	Input
mdotFarineRK	RK cc H.Ex	Source side flow rate
TFarineRK	RK cc H.Ex	Source side inlet temperature
EdotFarineRK	E and M Pyro	EdotFarineRK
mdotFarineRK	M and E RK	mdotFarineRK
EdotFarineRK	M and E RK	EdotFarineRK
Precalcined Farine equation output	**To**	**Parameter**
CpFarineRK	RK cc H.Ex	Specific heat of source side
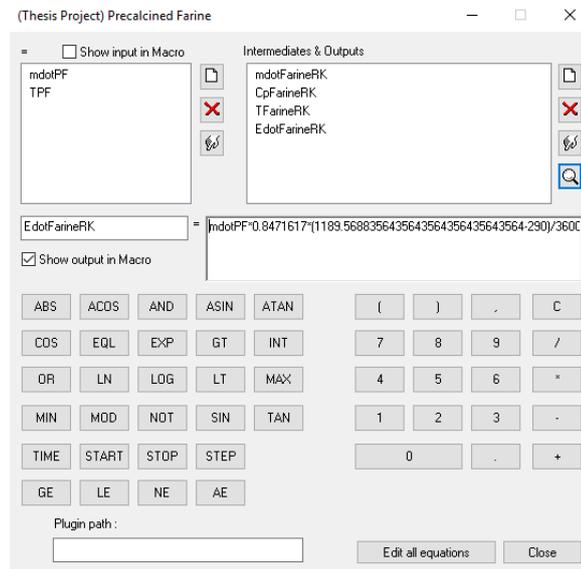
Figure 6.25 Precalcined farine equation window

6.2.1.37 Leakages

This equation receives the temperature and mass flowrate values of leakages in order to calculate the sensible energy of this material. Figure 6.26 shows the equation window and Table 6.39 represents the outlet connections of this equation.

Table 6.39 Leakages equation outputs

"Leakages" equation output	To	Input
Edotleak	E and M Pyro	Edotleakages
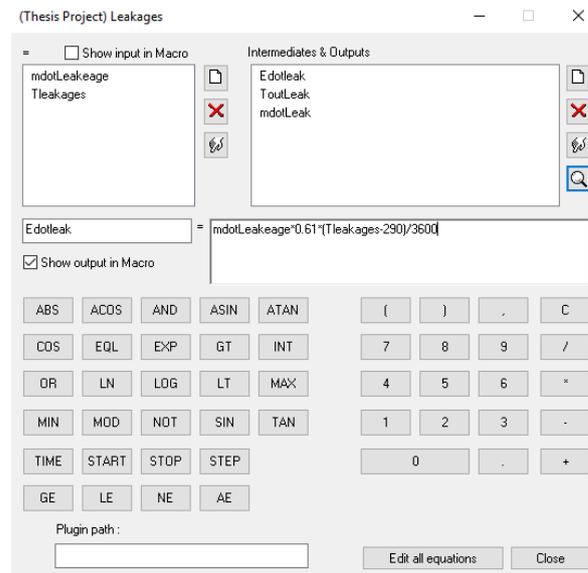
Figure 6.26 Leakages equation window

6.2.1.38 Coal

This equation transfers the coal's properties obtained from Table A.5. Table 6.40 represents the outlet connections of this equation.

Table 6.40 Coal equation outputs

Coal equation output	To	Input
mdotCoal	RK combustion chamber	fuel flow rate if mode 1
EdotinCoal	Load	Edotcoal
mdotCoal	M and E RK	mdotCoal
EdotinCoal	M and E RK	EdotinCoal
mdotLHV	M and E RK	mdotLHV

6.2.1.39 Primary Air

This equation transfers the temperature and mass flowrate values of primary air adopted from Table A.5. Moreover, temperature and specific heat values of the secondary air and primary air mixture are calculated by equations (5.10) and (5.11). Figure 6.27 shows the equation window and Table 6.41 represents the outlet connections of this equation.
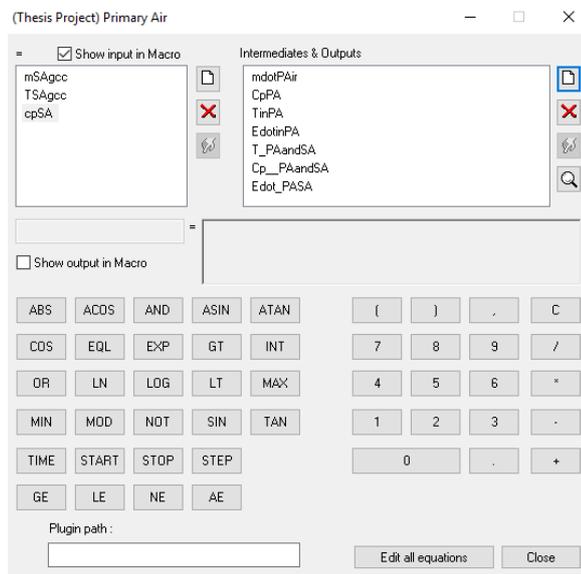
Figure 6.27 Primary Air equation

Table 6.41 Primary Air equation outputs

Primary Air equation	To	Input
mdotPAir	Mixer PA-SA	cold inlet flow rate
CpPA	Mixer PA-SA	Cold inlet heat capacity
TinPA	Mixer PA-SA	Cold inlet temperature
T_PAandSA	Mixer PA-SA	Setpoint temperture
EdotinPA	E and M Pyro	EdotinPA
mdotPAir	E and M Pyro	mdotPAir
EdotinPA	Load	EdotPA

6.2.1.40　Mixer PA-SA

This component mixes two flows with different specific heats and calculates the cold flowrate required to achieve the setpoint temperature. The cold fluid is the primary air, the hot fluid is the secondary air, and the setpoint temperature is the calculated value for the mixture of the primary and secondary air. The outputs of this component are:

Table 6.42 Mixer PA-SA equation outputs

Mixer PA-SA equation output	To	Input
outlet temperature	RK combustion	inlet air temperature
outlet flow rate	RK combustion	inlet air flow rate

6.2.1.41　Combustion chamber

This component is the combustion chamber of the rotary kiln and is the same component used in the precalcination unit. Similarly, the fuel used in this model is coal. Fuel element ratios and the lower calorific heat are previously indicated in Figure 6.22. Output connections of this component are presented in Table 6.43.

Table 6.43 RK combustion chamber outputs

RK combustion chamber output	To	Input
Outlet temperature	Load	TcombChm
Outlet mass flow combustion air	Load	mdotOUTComb
Fuel heat flow	Load	Qdotcoalcombustion
Outlet enthalpy	Load	HcombChm

6.2.1.42 Load

This equation transfers the temperature and mass flowrate values of combustion chamber's outlet fluid to the rotary kiln's heat exchanger. In addition, temperature of the secondary air, primary air and combustion air mixture is calculated by Equation (5.10). This component calculates the input energy rate of load fluid of the heat exchanger. Figure 6.28 shows the equation window and represents the outlet connections of this equation.
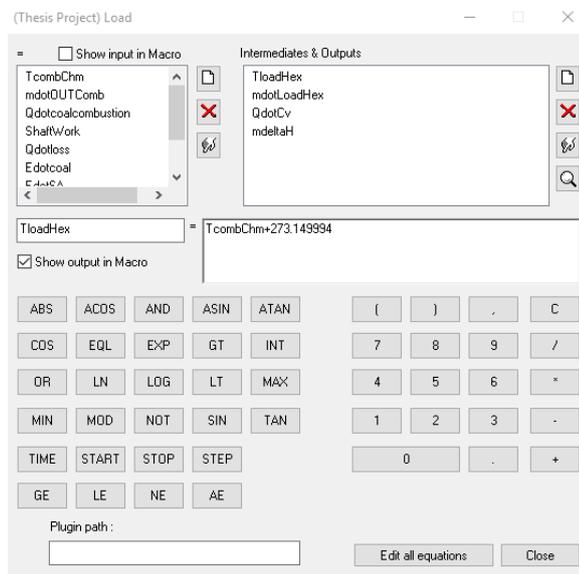
Figure 6.28 Load equation

Table 6.44 Load equation outputs

"Load" equation output	To	Input
TloadHex	RK cc H.Ex	Load side inlet temperature
mdotLoadHex	RK cc H.Ex	Load side flow rate
TloadHex	CpLoad	Tload
mdotLoadHex	CpLoad	mdotLoad
QdotCv	CpLoad	Qcv
mdeltaH	CpLoad	SensibleHeat

6.2.1.43 C_p Load

This equation calculates the sensible heat of combustion chamber's outlet fluid. Table 6.45 represents the outlet connections of this equation and Figure 6.29 shows the equation window.

Table 6.45 C_p Load equation outputs

C_p Load equation output	To	Parameter
Cp	RK cc H.Ex	Specific heat of load side fluid
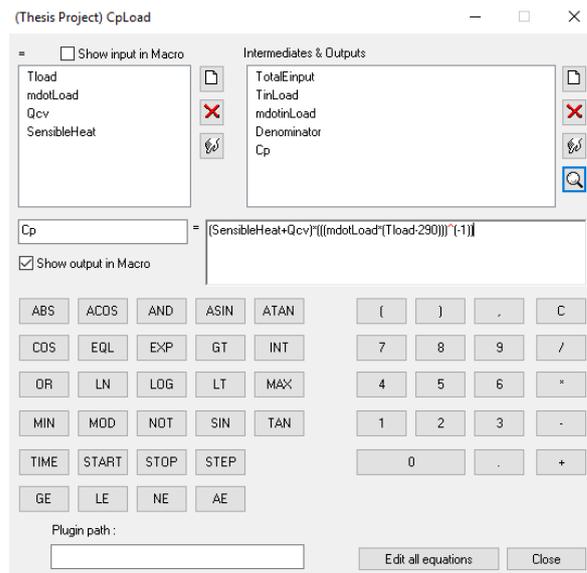
Figure 6.29 C_p Load equation

86

6.2.1.44   RK cc H.Ex

As shown in the Figure 6.7, the source and load fluids of the heat exchanger move in opposite directions relative to each other. As a result, the heat exchanger of the rotary kiln is modeled as a countercurrent heat exchanger. According to the Equation (6.6), the overall heat transfer coefficient of the exchanger is calculated. The input and parameter values and output connections are shown in Table 6.46.

Table 6.46 RK cc H.Ex heat exchanger

Parameter	Value	Unit
Specific heat of source side fluid	0.8472	kJ/kgK
Specific heat of load side	0.5713	kJ/kgK
Input	**Value**	**Unit**
Overall heat transfer coefficient	38893.93	kJ/hK
RK cc H.Ex output	**To**	**Input**
Source side outlet temperature	Diverter 6	Inlet Temperature
Source side flow rate	Diverter 6	Inlet Flowrate
Load side outlet temperature	Load Properties	Tload
Load side flow rate	Load Properties	mload
Heat transfer rate	E and M RK	Edot_ RKccH.Ex

6.2.1.45   Load Properties

This equation transfers the mass flowrate value of RK_cc_heat exchanger's load fluid to Diverter 7. In addition, it calculates the temperature of the hot gas leaving the rotary kiln. For this, the heat coefficient of the output hot gas of rotary kiln is obtained from Table A.6. Figure 6.30 and Table 6.47 display the equation window and the outlet connections of this equation, respectively.

Table 6.47 Load Properties equation outputs

Load Properties equation output	To	Input
TloadtoTHG	Mixer 7	Temperature at Inlet-
mdotLoad	Mixer 7	Flowrate at Inlet-1
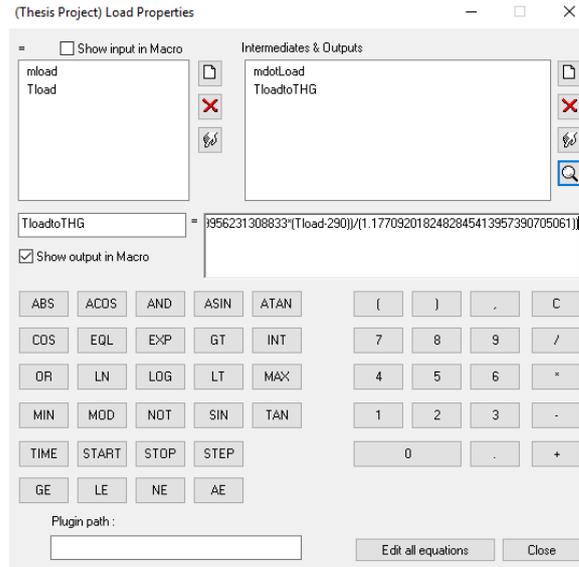
Figure 6.30 Load Properties equation window

6.2.1.46 Mixer 7

This valve mixes the hot gas exiting Load Properties equation box and the hot gas proportion of source load of "RK cc heat exchanger". Table 6.48 shows the output connections of this component.

Table 6.48 Mixer 7 outputs

Mixer 7 output	To	Input
Outlet Temperature	Farine to PYRO	THGRK
Outlet Flowrate	Farine Silo	mdotHotGasRK

6.2.1.47   Hot Gas RK

This equation transfers the properties of hot gas leaving the rotary kiln and calculates the sensible heat of it. Figure 6.31 shows the equation window and Table 6.49 represents the outlet connections of this equation.
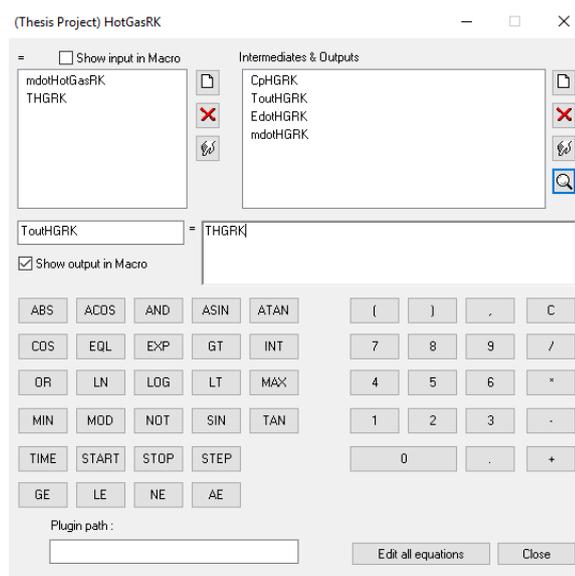
Figure 6.31 Hot Gas RK equation window

Table 6.49 Hot Gas RK equation outputs

Hot Gas RK equation output	To	Parameter
ToutHGRK	Diverter 4	Inlet temperature
mdotHGRK	Diverter 4	Inlet flow rate
EdotHGRK	M and E RK	EdotHGRK

6.2.1.48   Diverter 4

This diverter splits the outlet hot gas of rotary kiln into two mass flows. The control signal is calculated by the mass flowrate values of hot gas inlet of raw mill and hot

gas output of rotary kiln listed in the Table A.1 and Table A.6, respectively. Table 6.49 represents the output connections of this component.

$$\text{Control signal} = \frac{\dot{m}_{hot\ gas\ to\ RM}}{\dot{m}_{hot\ gas\ leaving\ RK}} \simeq 0.497 \tag{6.17}$$

Table 6.50 Diverter 4 outputs

Diverter 4 output	To	Input
Flow rate at outlet 1	Diverter 5	Inlet flow rate
Flow rate at outlet 2	GasfromRK	mdotHGINRK

6.2.1.49 Diverter 5

This component splits the input hot gas into two mass flowrates. The control signal is calculated by the mass flowrates of the hot gas entering and exiting the pyroprocessing tower, which are listed in Table A.3 and Table A.4 , respectively. Table 6.51 shows the output connections of this component.

$$\text{Control signal} = \frac{\dot{m}_{hot\ gas\ toPyroUnit}}{\dot{m}_{hot\ gas\ leaving\ RK} - \dot{m}_{hot\ gas\ RM}} \simeq 0.988 \tag{6.18}$$

Table 6.51 Diverter 5 output

Diverter 5 output	To	Input
Flow rate at outlet 1	Type744	Inlet flow rate
Temperature at outlet 1	Type744	Inlet temperature
Flow rate at outlet 2	HG fromRotaryBurner	mdotHGRKtoPYRO
Temperature at outlet 2	HG fromRotaryBurner	THG_RKtoPYRO

6.2.1.50   HG from Rotary Burner

This equation transfers the properties of hot gas input of pyroprocessing tower and calculates temperature of it. Figure 6.32 shows the equation window and Table 6.52 represents the outlet connections of this equation.

Table 6.52 HG fromRotaryBurner equation output

HG from Rotary Burner equation output	To	Input
MdotHG	TmixHGFarine	mdotHG
T_HGRKtoPYRO	TmixHGFarine	TinHG
CpHG	TmixHGFarine	CpHG
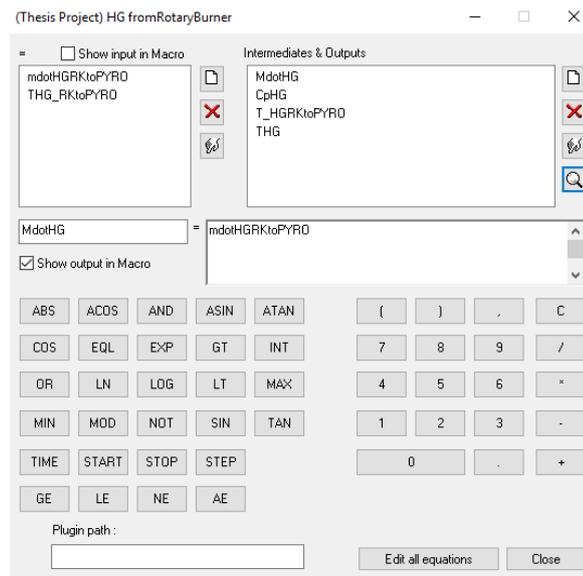
Figure 6.32 HG fromRotaryBurner equation window

6.2.1.51   Diverter 6

This diverter splits source fluid leaving "RK cc heat exchanger" into three mass flows shown in the Table 6.53. The control signal is calculated by the outlet mass flowrate values of the rotary kiln listed in Table A.6.

$$\text{Fraction of Flow to Outlet -1} = \frac{\dot{m}_{Clinker}}{\dot{m}_{Precalcined\ Farine}} \simeq 0.621$$

$$\text{Fraction of Flow to Outlet -2} = \frac{\dot{m}_{Dust\ and\ Ash}}{\dot{m}_{Precalcined\ Farine}} \simeq 0.123 \qquad (6.19)$$

$$\text{Fraction of Flow to Outlet -3} = 1 - \left(\frac{\dot{m}_{Clinker}}{\dot{m}_{Precalcined\ Farine}} + \frac{\dot{m}_{Dust\ and\ Ash}}{\dot{m}_{Precalcined\ Farine}}\right)$$

Table 6.53 Diverter 6 outputs

Diverter 6 output	To	Input
Outlet Flowrate-1	Clinker	mdotClinker
Outlet Temperature-1	Clinker	TclinkeroutRK
Outlet Flowrate-2	DustandAsh	mdotDAsh
Outlet Temperature-2	DustandAsh	TDAsh
Outlet Flowrate-3	Mixer 7	Flowrate at Inlet-2
Outlet Temperature-3	Mixer 7	Temperature at Inlet-2

6.2.1.52 Clinker

This equation transfers the properties of clinker to grate cooler unit. Table 6.54 shows the details of this component.

Table 6.54 Clinker equation outputs

Clinker equation output	To	Input
TinClinkerRK	GCC	Source temperature
mdotClinkerRK	GCC	Source side flow rate
mdotClinkerRK	E and M GCC	mdotClinker
EdotClinkerRK	E and M GCC	EdotClinker

Clinker equation output	To	Parameter
CpClinkerRK	GCC	Specific heat of source side fluid

6.2.1.53 Cooling Air

This equation transfers the properties of the cooling air to the grate cooler unit using values from Appendix Table A.7. Table 6.55 represents the outlet connections of this equation.

Table 6.55 Cooling Air equation outputs

Cooling Air" equation output	To	Input
TinmdotCoolingAir	GCC	Load side temperature
mdotCoolingAir	GCC	Source side flow rate
mdotCoolingAir	E and M GCC	mdotCoolingAir
EdotCoolingAir	E and M GCC	EdotCoolingAir
"Cooling Air" equation output	**To**	**Parameter**
CpCoolingAir	GCC	Specific heat of source side fluid

6.2.1.54 GCC

The grate cooler is modeled as a cross-current fully mixed heat exchanger. According to the Equation (6.6) and the unit's output properties, the overall heat transfer coefficient of the exchanger is calculated. The inputs and parameter values and output connections of the heat exchanger are listed in Table 6.56.

Table 6.56 GCC heat exchanger outputs

Parameter	Value	Unit
Specific heat of source side fluid	0.847	kJ/kgK
Specific heat of load side	0.99	kJ/kgK
Input	**Value**	**Unit**
Overall heat transfer coefficient	38893.93	kJ/hK
GCC output	**To**	**Input**
Source side outlet temperature	CooledClinker	TCClinker
Source side flow rate	CooledClinker	mdotCClinker

Table 6.56 (Continued)

Load side outlet temperature	Load Air	TinLoadAir
Load side flow rate	Load Air	mdotLoadAir

6.2.1.55 Cooled Clinker

This equation shows the properties of cooled clinker leaving "GCC". Figure 6.33 shows the equation window and Table 6.57 represents the outlet connections of this equation.
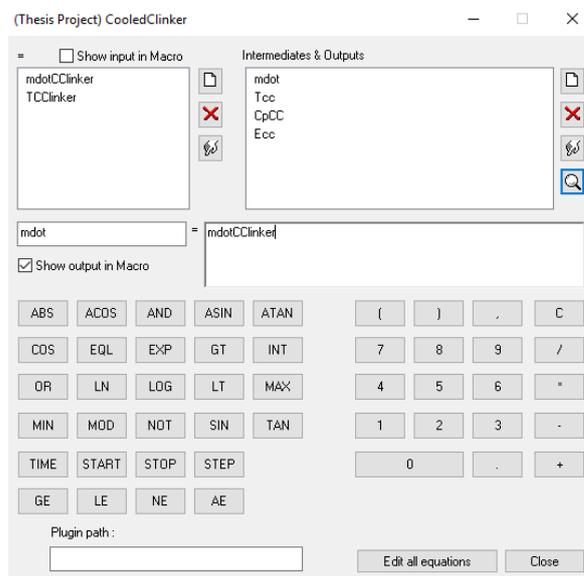
Figure 6.33 Cooled Clinker equation window

Table 6.57 Cooled Clinker equation outputs

Cooled Clinker equation output	To	Input
mdot_CClinker	E and M GCC	mdot_CClinker
T_Cclinker	E and M GCC	T_Cclinker
Edot_Cclinker	E and M GCC	Edot_Cclinker
T_Cclinker	Printer	T_Cclinker

6.2.1.56 Load Air

This equation transfers the properties of the heated load fluid of the grate cooler heat exchanger to the diverter. Table 6.58 and Figure 6.34 display the edtails of this equation component.

Table 6.58 Load Air equation outputs

Load Air equation output	To	Input
Mdot_loadAir	Diverter 8	Inlet Flowrate
TinloadAir	Diverter 8	Inlet Temperature
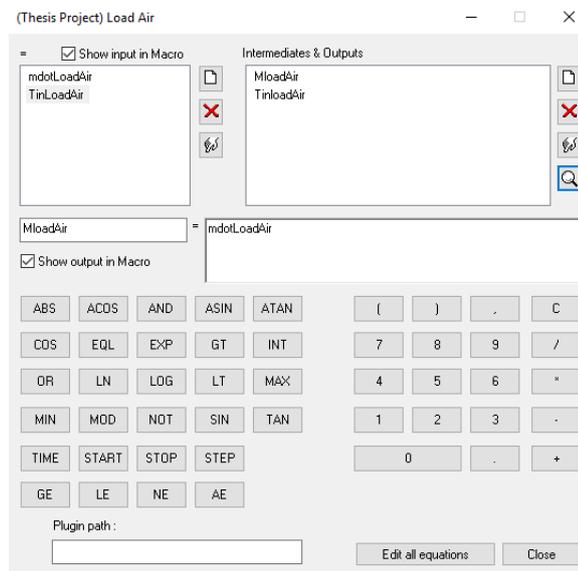
Figure 6.34 Load Air equation

6.2.1.57 Diverter 8

This diverter splits the load fluid leaving the grate cooler unit into three mass flows. Table 6.59 shows the output connections of this component. The control signals of this component are calculated by the outlet mass flowrates of the air listed in Appendix Table A.7.

$$\text{Fraction of Flow to Outlet -1} = \frac{\dot{m}_{Secondary\ Air}}{\dot{m}_{Cooling\ Air}} \simeq 0.2532$$

$$\text{Fraction of Flow to Outlet -2} = \frac{\dot{m}_{Tertiary\ Air}}{\dot{m}_{Cooling\ Air}} \simeq 0.323$$

$$\text{Fraction of Flow to Outlet -3} = \frac{\dot{m}_{Exhaust\ Air}}{\dot{m}_{Cooling\ Air}} \simeq 0.4235 \tag{6.20}$$

Table 6.59 Diverter 8 outputs

Diverter 8 output	To	Input
Outlet Flowrate-1	SecondaryAir	mdotSA
Outlet Temperature-1	SecondaryAir	TSA
Outlet Flowrate-2	TertiaryAir	mdotTA
Outlet Temperature-2	TertiaryAir	TTA
Outlet Flowrate-3	ExhaustAir	mdotEA
Outlet Temperature-3	ExhaustAir	TEA

6.2.1.58 Secondary Air

This equation transfers the properties of secondary air derived from Appendix Table A.7 to the Mixer PA-SA. Figure 6.35 shows the equation window and Table 6.60 represents the outlet connections of this equation.

Table 6.60 Secondary Air outputs

Secondary Air equation output	To	Input
mdot_SA	Mixer PA-SA	Hot flow rate
Tin_SA	Mixer PA-SA	Hot inlet temperature
c_p_SA	Mixer PA-SA	specific heat capacity
mdot_SA	E and M GCC	mdot_SA
Edot_SA	E and M GCC	Edot_SA
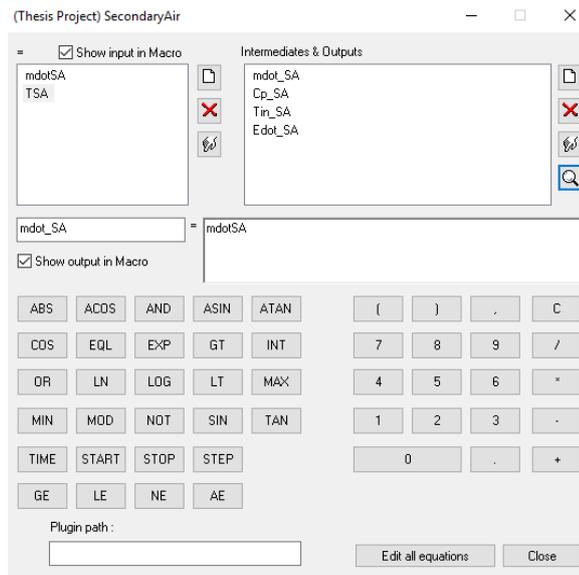
Figure 6.35 Secondary Air equation

6.2.1.59   Tertiary Air

This equation shows the properties of tertiary air leaving the grate cooler unit and transfers its properties to the precalciner. Figure 6.36 and Table 6.61 represent the details of this equation.
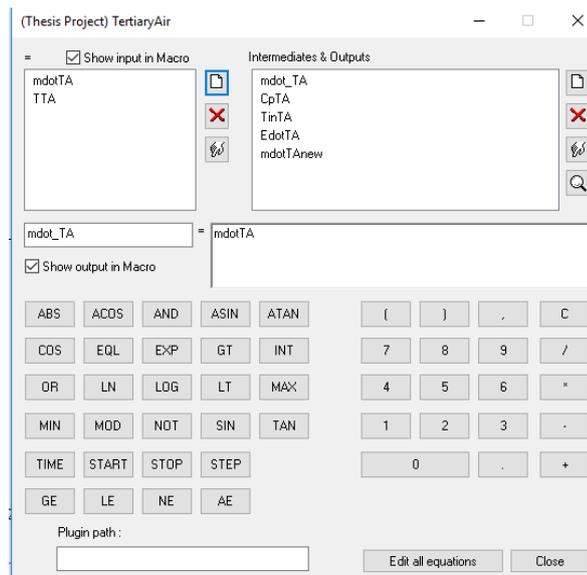
Figure 6.36 Tertiary Air equation window

Table 6.61 Tertiary Air equation output

Tertiary Air equation output	To	Input
mdot_TA	E and M GCC	mdot_TA
Edot_TA	E and M GCC	Edot_TA
TinTA	Calciner_C_CH	inlet air temperature
mdot_TA	Calciner_C_CH	inlet air flow rate

6.2.1.60   Exhaust Air

This equation shows the properties of tertiary air. Figure 6.37 demonstrates the equation window and Table 6.62 represents the outlet connections of this equation.
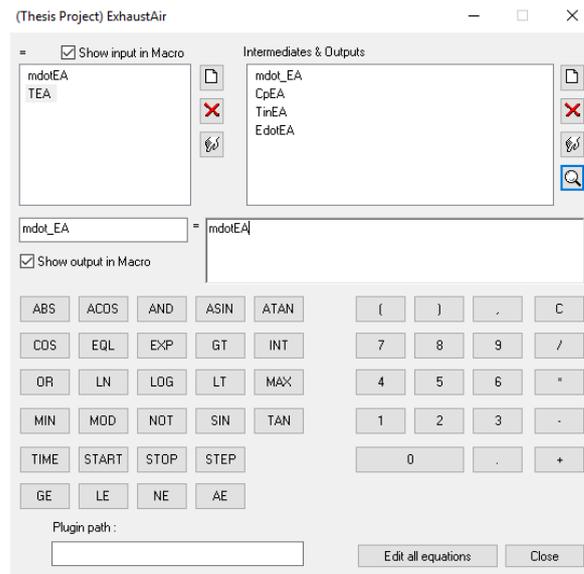
Figure 6.37 Exhaust Air equation

Table 6.62 Exhaust Air outputs

Exhaust Air equation output	To	Input
mdot_EA	E and M GCC	mdot_EA
EdotEA	E and M GCC	EdotEA

6.3 Solar-integrated TRNSYS Model of the Cement Plant

In the second section of this chapter, solar-based models of the cement plant are created by hybridizing the system.

6.3.1 Solar-integrated TRNSYS Model of the Conventional Cement Plant (Model-2)

A schematic of the model in the TRNSYS simulation studio is presented in Figure 6.38. The conventional plant model is compressed into several macros and a solar based power plant is added to the model. The model consists of a heliostat solar field with 1000 heliostats of size 100 m^2 each. Solar DNI and azimuth and zenith angles are given by a weather file, which contains weather data for a whole year.
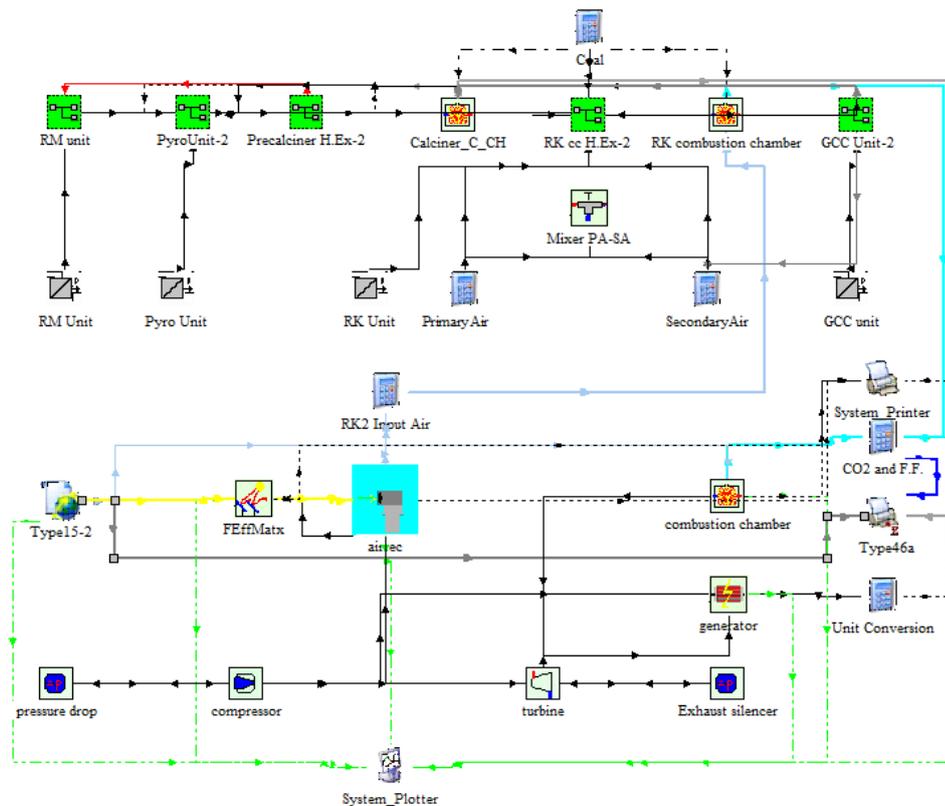
Figure 6.38 TRNSYS Layout of the Solar-integrated Cement Plant

The heliostats concentrate the sunlight onto an air receiver, which is fed by a compressor. After the receiver, there is an equation box that mixes the input air mixture of the rotary kiln with the solar-heated air and uses the warm air to feed the rotary kiln and the combustion chamber. The chamber in the solar model raises the air temperature to $1100^{\circ C}$ in order to feed a gas turbine. The turbine provides the essential power of a generator to produce electricity. The additional components utilized in the new model are listed in Table 6.63. Afterwards, the components and their connections are desribed in detail.

Table 6.63 List of the components in TRNSYS model

Name	Type	Note
Weather data	15-2	Importing TMY2 weather data
Type16g	16g	Interpolating radiation data
Heliostat field (EffMatx)	394	Modeling a heliostat field
Pressurized air receiver	422	Modeling an air receiver
Compressor	424	Compressing the air
Pressure drop	429	Calculating the pressure loss
RK_2 Input Air	Equation	Calculating the air properties
Combustion chamber	426	Modeling a combustion chamber
Tmix RM	Equation	Calculating mixture's temperature
Turbine	427	Modeling a gas turbine
Generator	428	Calculating the electric output
CO_2 and F.F.	Equation	Calculating mass flowrate
Plotter	65	Calculating the electrical output in kW
Printer	25	Saving output data
Printegrator	46a	Integrating and printing a transient input

6.3.1.1 Weather data

This component reads meteorological data at regular time intervals from an external weather data file for Gaziantep-Turkey and sends the outputs to other TRNSYS components as represented in Table 6.64.

Table 6.64 Weather data outputs

Weather data output	To	Input
Direct normal radiation	Heliostat field	Direct insolation
Wind velocity	Heliostat field	wind speed
Total horizontal radiation	Type16g	mdotDAsh
Direct normal radiation	Type16g	TDAsh
Slope of surface	Type16g	Flowrate at Inlet-2
Azimuth of surface	Type16g	Azimuth of surface
Dry bulb temperature	RK2 Input Air	Tenv
Direct normal radiation	Plotter	Right axis variable-3

6.3.1.2 Type16g

This component can compute radiation on tilted surfaces. The output connections are demonstrated in Table 6.65.

Table 6.65 Type16g outputs

Type 16g output	To	Input
Solar zenith angle	FEffMatx	solar zenith angle
Solar azimuth angle	FEffMatx	solar azimuth angle

6.3.1.3 Heliostat field (EffMatx)

This type models a solar concentrator field and evaluates its performance by a user-provided efficiency matrix for solar azimuth and zenith angles. The connections and

parameters of this component are listed in Table 6.66. The fundamental parameter values of the area for each heliostat and number of collector units are extracted from [145] and [146].

Table 6.66 EffMatx outputs

EffMatx parameter	Value	Unit
No of zenith angle data points	7	-
No of azimuth angle data	9	-
No of concentrator units	1000	-
Mirror surface area	100	m^2
av reflectivity	0.95	-
EffMatx output	**To**	**Input**
Power to receiver	Air Receiver	solar input power
Power to receiver	Printegrator	Input to be printed-10
Power to receiver	Plotter	Left axis variable-1

6.3.1.4   Air Receiver

This component can calculate the outlet temperature, pressure and enthalpy depending on the essential inlet conditions provided. According to [147], since the aperture area of the receiver is normally 30 to 50 m^2, the area is consideered 40 m^2. The details of this type is tabulated in Table 6.67.

Table 6.67 Air Receiver parameters and outputs

Air receiver parameter	Value	Unit
Optical efficiency	0.95	-
Receiver aperture	40	m^2
Emissivity of absorber	1	-
Air Receiver output	**To**	**Input**
air outlet temperature	RK2 Input Air	ToutRec
air outlet pressure	RK2 Input Air	PoutRec
air outlet mass flow	RK2 Input Air	mdotoutRec

Table 6.67 (Continued)

air outlet enthalpy	RK2 Input Air	HoutRec
air outlet temperature	Plotter	Right axis variable-2
air outlet temperature	Printer	Input to be printed-8
overload	FEffMatx	on/off control

6.3.1.5 Compressor

According to the [145], air is compressed by a compressor to 15 bar. Thus, the compression ratio is assumed 15 for the air that is fed through the compressor at 1 bar. Then, the air feeds the receiver at 200 tonnes/h. The outputs of this type is displayed in Table 6.68.

Table 6.68 Compressor outputs

Compressor output	To	Input
outlet temperature	Air Receiver	temperature cooling air
outlet pressure	Air Receiver	air inlet pressure
outlet enthalpy	Air Receiver	air inlet enthalpy
outlet mass flow working air	Air Receiver	air inlet mass flow
outlet temperature	Turbine	temperature cooling air
outlet mass flow cooling air	Turbine	mass flow cooling air
outlet enthalpy	Turbine	enthalpy cooling air
actual compressor power	Generator	Compressor shaft work
total outlet mass flow	Pressure drop	inlet mass flow
outlet pressure	Pressure drop	inlet pressure
outlet temperature	Pressure drop	inlet temperature

6.3.1.6   Pressure drop and Pressure drop 2

These models calculate the pressure loss with consideration of the actual load values and the outlet pressure is fed through the compressor and the turbine as represented in Table 6.69.

Table 6.69 Pressure Drop outputs

Pressure Drop output	To	Input
outlet temperature	Compressor	inlet air temperature
outlet pressure	Compressor	inlet pressure
Pressure Drop 2 output	**To**	**Input**
relative pressure drop	Turbine	relative pressure drop

6.3.1.7   RK$_2$ Input Air

This equation serves as a mixer and unit converter. To elaborate, primary, secondary and the air from the receiver are mixed and the properties of the mixture are evaluated. Furthermore, the unit of power produced by the heliostats is converted into kW. The details of this component are demonstrated in Table 6.70 and Figure 6.39.
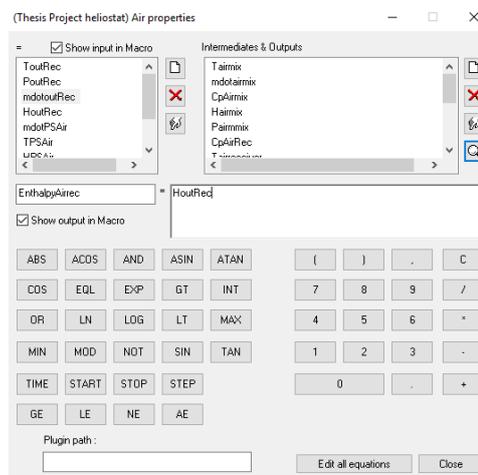
Figure 6.39 RK$_2$ Input Air equation window

Table 6.70 RK2 Input Air outputs

RK₂ Input Air output	To	Input
Tairmix	printer	Input to be printed-1
mdotairmix	printer	Input to be printed-2
CpAirmix	printer	Input to be printed-3
TairmixtoTurbine	Combustion chamber	inlet air temperature
PairmixtoTurbine	Combustion chamber	inlet air flow rate
mdotairmixtoTurbine	Combustion chamber	inlet pressure
HairmixtoTurbine	Combustion chamber	inlet enthalpy
TairmixtoRK	RK Combustion chamber	inlet air temperature
PairmixtoRK	RK Combustion chamber	inlet air flow rate
mdotairmixtoRK	RK Combustion chamber	inlet pressure
HairmixtoRK	RK Combustion chamber	inlet air temperature

6.3.1.8   Combustion chamber

This type simulates an adiabatic combustion chamber for fuels. The parameters of this component are considered identical to the quantities mentioned in Figure 6.22. This model works in mode-2 in order to calculate the fuel mass flow required to give out a specified outlet temperature. The output connections of the component are listed in Table 6.71.

Table 6.71 Combustion Chamber outputs

Combustion Chamber output	To	Input
Outlet temperature	Turbine	temperature combustion air
Outlet pressure	Turbine	inlet pressure
Outlet mass flow combustion air	Turbine	mass flow combustion air
CO_2 mass ratio	Turbine	CO_2 mass ratio
H_2O mass ratio	Turbine	H_2O mass ratio
SO_2 mass ratio	Turbine	SO_2 mass ratio
Air mass ratio	Turbine	Air mass ratio
Airnitrogen mass ratio	Turbine	Airnitrogen mass ratio

Table 6.74 (Continued)

Outlet enthalpy	Turbine	inlet enthalpy working air
Outlet temperature	Plotter	Right axis variable-1
Fuel mass flow	CO_2 and F.F.	FF-2
Outlet mass flow CO_2	CO_2 and F.F.	CO_2-2

6.3.1.9   Turbine

This type is a gas turbine and calculates the outlet conditions from the inlet conditions specified by the user. The output connection of this component are displayed in Table 6.72.

Table 6.72 Turbine outputs

Turbine output	To	Input
Outlet temperature	Pressure drop 2	inlet temperature
Outlet pressure	Pressure drop 2	inlet pressure
Outlet mass flow	Pressure drop 2	inlet mass flow
Actual turbine power	Generator	Total turbine power

6.3.1.10   Generator

This type is designed to work with a gas turbine. It calculates the net electric output and thermal efficiency. The details of the model are shown in Table 6.73.

Table 6.73 Generator outputs

Generator output	To	Input
Electric output	Clinker	mdotClinker
Electric output	Plotter	Left axis variable-2
Electric output	Printegrator	Temperature at Inlet-2

106

6.3.1.11 CO$_2$ and F.F.

This equation sums up the fossil fuel mass flowrate in the combustion chambers (Rotary kiln's combustion chamber and turbine's combustion chamber) and the CO$_2$ emission mass flowrate of them and sends the outputs to the plotter. The outputs of the equation are listed in Table 6.74.
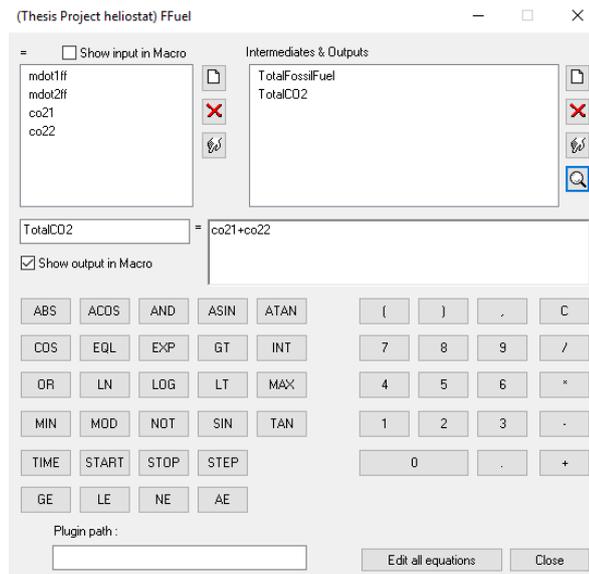
Figure 6.40 CO$_2$ and F.F. equation outputs

Table 6.74 CO$_2$ and F.F. equation outputs

CO$_2$ and F.F. equation output	To	Input
mdotFossilFuel	Plotter	Right axis variable-7
mdot CO$_2$	Plotter	Right axis variable-8
mdotFossilFuel	Printegrator	TotalFossilFuel
mdot CO$_2$	Printegrator	Total CO$_2$

6.3.2 Solar-integrated TRNSYS Model of the Conventional Cement Plant With A Preheater before Pyroproprocessing Unit (Model-3)

In this model, a preheater is added to the solar-integrated plant described in section 6.3.1. A schematic of the model in the TRNSYS simulation studio is presented in Figure 6.41. The solar field model is identical to the field that is mentioned in section 6.3.1 with an increased air mass flowrate in the air-receiver. Several components are added to the system in order to preheat the farine that is the product of the raw mill unit using the solar-heated air from the air receiver. To elaborate, 75000 kg/h air from the air receiver is used to supply the hot load side fluid of the preheater.
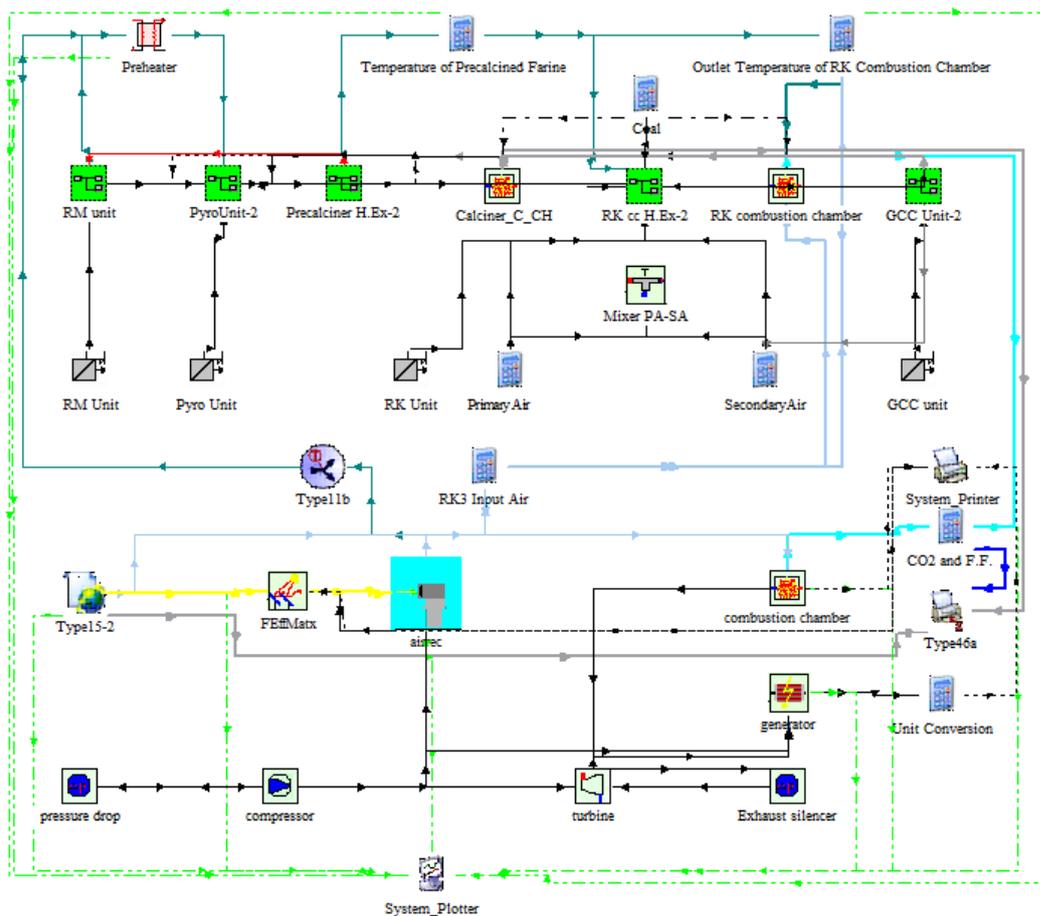
Figure 6.41 TRNSYS Layout of the Solar-integrated Cement Plant with a solar-based preheater

The farine as the source side fluid of the preheater is heated and fed to the pyroprocessing tower. Temperature of the precalcined farine that exits the precalciner is calculated and plotted. The precalcined farine continues its way to the rotary kiln unit. Since the temperature of the precalcined farine has increased in comparison with the plant without a preheater, less energy is required to run the clinkerization process. The energy rate difference is calculated and the output temperature of the rotary kiln's combustion chamber needed to stabilize the input energy of the rotary kiln. Finally, total fossil fuel consumption and CO_2 emission are calculated. The additional components utilized in the model are listed in Table 6.75 and their connections are described in detail.

Table 6.75 List of the components in TRNSYS model

Name	Type	Note
RK_3 Input Air	Equation	Calculating the air properties
Tempering Valve	11b	Modeling a temperature controlled valve
Preheater	15b	Preheating the farine
Temperature of Precalcined Farine	Equation	Sending the temperature of the precalcined farine to plotter
Outlet Temperature of RK Combustion Chamber	Equation	Calculating the outlet temperature of the combustion chamber

6.3.2.1 RK_3 Input Air

Similar to the "RK_2 Input Air" equation, primary, secondary and the air from the diverter are mixed and the properties of the mixture are calculated. Furthermore, the equation transforms the essential data to the other components. The additional output connections of this component are listed in Table 6.76.

Table 6.76 RK$_3$ Input Air outputs

RK$_3$ Input Air output	To	Input
C$_p$_AirReceiver	Outlet Temperature of RK Combustion Chamber	C$_p$AirtoRK
mdotAirtoRK	Outlet Temperature of RK Combustion Chamber	mdotAirtoRK
T_AirMix	RK combustion chamber	inlet air temperature
mdotAirtoRK	RK Combustion chamber	inlet air flowrate

6.3.2.2   Tempering Valve (Type 11b)

This component models a temperature controlled liquid flow diverter. It sends the solar-heated airflow from air-receiver through outlet 1 when T$_{\text{out Air Receiver}} < 600^{\circ C}$. The inputs and outputs of the component are displayed in Table 6.77.

Table 6.77 Tempering Valve (Type 11b) inputs and outputs

Tempering Valve input	Value	Unit
Inlet flowrate	75000	kg/h
Setpoint temperature	600	C
Tempering Valve output	**To**	**Input**
Temperature at outlet-1	Preheater	Load-side temperature
Flowrate at outlet-1	Preheater	Load-side flowrate

6.3.2.3   Preheater

A heat exchanger is added to the system in order to preheat the farine (at about 391K) that enters the pyroprocessing unit with solar-heated air from tempering valve. Temperature profile of the farine leaving the preheater is plotted to evaluate how much it is increased. The output connections of the component are listed in Table 6.78.

Table 6.78 Preheater outputs

Preheater output	To	Input
Source side outlet temperature	Pyroprocessing Unit	Source side temperature
Source side outlet flowrate	Pyroprocessing Unit	Source side flowrate
Source side outlet temperature	Plotter	Source side temperature

6.3.2.4 Temperature of Precalcined Farine

This equation calculates the temperature of the precalcined farine using the sensible heat of the steam and leakages that separates from the precalcined farine. Afterwards, it sends the calculated temperature of the precalcined farine that comes out of the precalciner to the plotter in order to compare the result with its temperature in the conventional cement plant model. The details of the equation are presented in Figure 6.42 and Table 6.79. Furthermore, the calculated temperature is sent to the "Outlet Temperature of RK Combustion Chamber" equation to evaluate the energy balances in the rotary kiln.

$$T_{\mathrm{Pr}ecalcined\ farine} = \frac{T_{ambient} + ((\dot{m}_{Source} \times (T_{Source} - T_{ambient}) \times c_{p_{source}}) - (\dot{m}_{Steam} \times c_{p_{source}} \times (T_{Source,Out(C_1 and D_1)} - T_{ambient}))}{\dot{m}_{\mathrm{Pr}ecalcined\ farine(19')} \times c_{p_{\mathrm{Pr}ecalcined\ farine(19')}}}$$

$$T_{\mathrm{Pr}ecalcined\ farine} = \frac{290 + ((138481 \times (T_{Source} - 290) \times 1.253) - (9791 \times 1.253 \times (T_{Source,Out(C_1 and D_1)} - 290))}{105000 \times 0.847}$$

(6.21)

where $\dot{m}_{Source}$ and T_{Source} stand for the properties of the source fluid that exit the pyroprocessing tower in Model-3, $c_{p_{source}}$ and $\dot{m}_{Steam}$ for the specific heat value of the source side fluid of the pyroprocessing unit and the mass flowrate of steam released from C_1 and D_1, $c_{p_{\mathrm{Pr}ecalcined\ farine(19')}}$ and $\dot{m}_{\mathrm{Pr}ecalcined\ farine(19')}$ for the specific heat value and mass flowrate of precalcined farine derived from the results of Model-1. $T_{Source,Out(C_1 and D_1)}$ is the outlet temperature of the source side fluid of the C_1 and D_1 in Model-3.
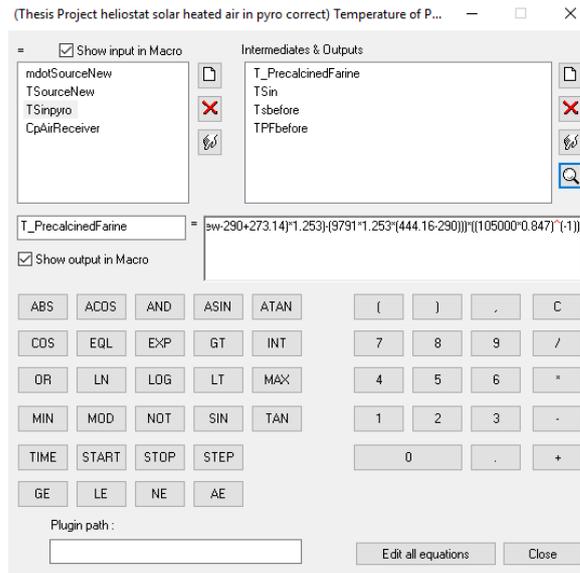
Figure 6.42 Temperature of Precalcined Farine equation window

Table 6.79 Temperature of Precalcined Farine output

Temperature of Precalcined Farine output	To	Input
T_PrecalcinedFarine	Pyroprocessing Unit	T_PrecalcinedFarine
T_PrecalcinedFarine	Plotter	T_PrecalcinedFarine

6.3.2.5 Outlet Temperature of RK Combustion Chamber

This equation is added to evaluate the energy balances in the rotary kiln and calculate the outlet temperature of the rotary kiln's combustion chamber. The equation window is shown in Figure 6.43 and the output connections of this equation are listed in Table 6.80.

$$T^{\circ C}_{Out,RK\ Combustion\ Chamber} = \frac{(\dot{m}_{Precalcined\ farine(19')} \times c_{p_{Precalcined\ farine(19')}} \times (T_{Precalcined\ farine(19')} - T_{Precalcined\ farine})) + ((\dot{m}_{Air\ to\ RK} \times c_{p_{Air\ to\ RK}} \times (T^{\circ C}_{Air\ to\ RK} - T^{\circ C}_{ambient})))}{\dot{m}_{Air\ to\ RK} \times c_{p_{Air\ to\ RK}}} + T^{\circ C}_{ambient}$$

$$T^{\circ C}_{Out,RK\ Combustion\ Chamber} = \frac{(105000 \times 0.847 \times (1189.6 - T_{Precalcined\ farine})) - (\dot{m}_{Air\ to\ RK} \times c_{p_{Air\ to\ RK}} \times (1850 - 16.85))}{\dot{m}_{Air\ to\ RK} \times c_{p_{Air\ to\ RK}}} + 16.85$$

(6.22)

where $\dot{m}_{\mathrm{Pr}ecalcined\ farine(19')}$, $c_{p_{\mathrm{Pr}ecalcined\ farine(19')}}$ and $T_{\mathrm{Pr}ecalcined\ farine(19')}$ stand for the properties of the precalcined farine derived from the results of Model-1, $T_{\mathrm{Pr}ecalcined\ farine}$ is the temperature that is calculated from equation (6.21) for Model-3, $\dot{m}_{Air\ to\ RK}$ and $c_{p_{Air\ to\ RK}}$ are derived from the air-receiver and they are the same for Model-2 and Model-3.
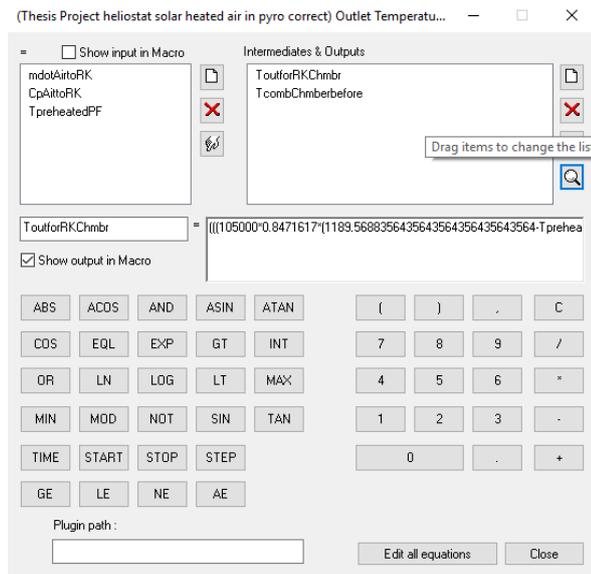
Figure 6.43 Outlet Temperature of RK Combustion Chamber equation window

Table 6.80 Outlet Temperature of RK Combustion Chamber equation outputs

Outlet Temperature of RK Combustion Chamber	To	Input
T out for RK combustion chamber	RK combustion chamber	Outlet temperature if mode-2
Source side outlet temperature	Plotter	Source side temperature

CHAPTER 7

RESULTS AND DISCUSSION

Results are obtained by connecting desired outputs to online plotters and/or printers to save them in Excel format. Before running the models, some changes can be made to the TRNSYS settings, Figure 7.1 and Figure 7.2. These changes include simulation start and stop time, time step, tolerance integration and convergence.
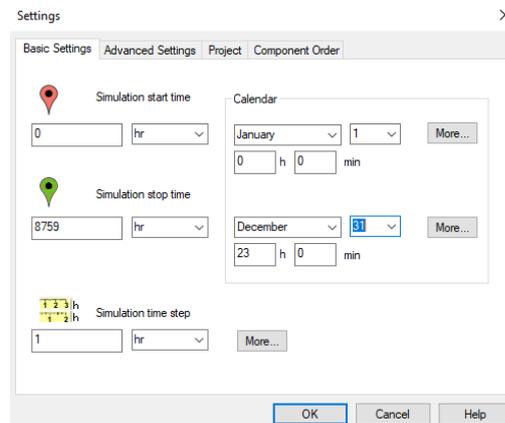
Figure 7.1 TRNSYS settings window
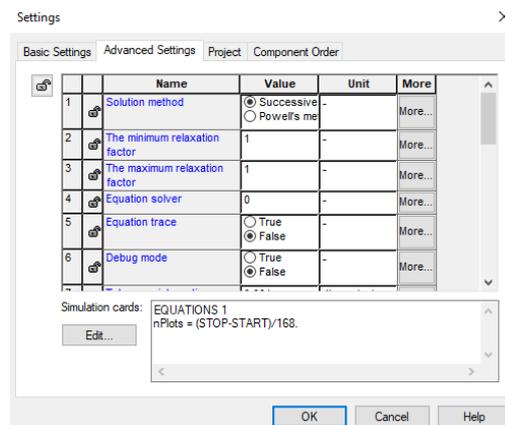
Figure 7.2 TRNSYS settings window

Simulation start and stop time are set according to the hours of a year from a calendar but the time step is fixed at 0.125 hour. In addition, both tolerance integration and convergence are set to 0.01 to reduce running time. The conventional and solar-integrated models are run for a full year.

7.1   Conventional Cement Plant Model (Model-1)

The TRNSYS model described in section 6.2 simulates the main units of a cement plant and is run assuming the ambient temperature to be constant and equal to 290K. Figure 7.3 indicates a schematic of mass and energy flows of each unit of the reference cement plant in [30]. On the other hand, Figure 7.4 represents the identical mass and energy flow diagram in the raw mill (Unit-2), pyroprocessing tower (Unit-3), rotary kiln (Unit-4) and grate clinker cooler (Unit-6) of the TRNSYS model. The results of the modeled units (Units 2,3,4, and 6) of the plant are listed and compared with the on-site data from [30] provided in the appendix. A.
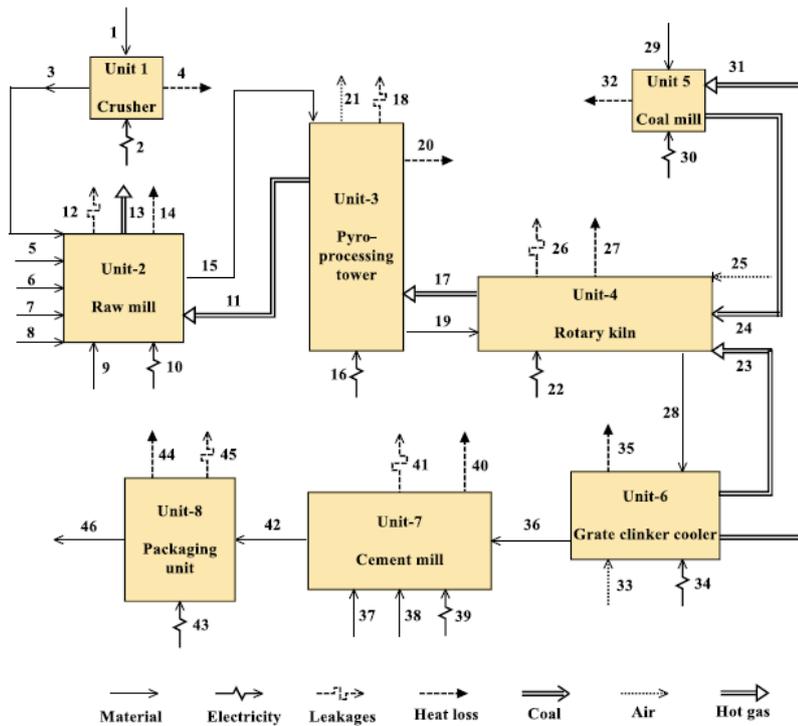
Figure 7.3 The schematic of an actual cement manufacturing plant [30].

116
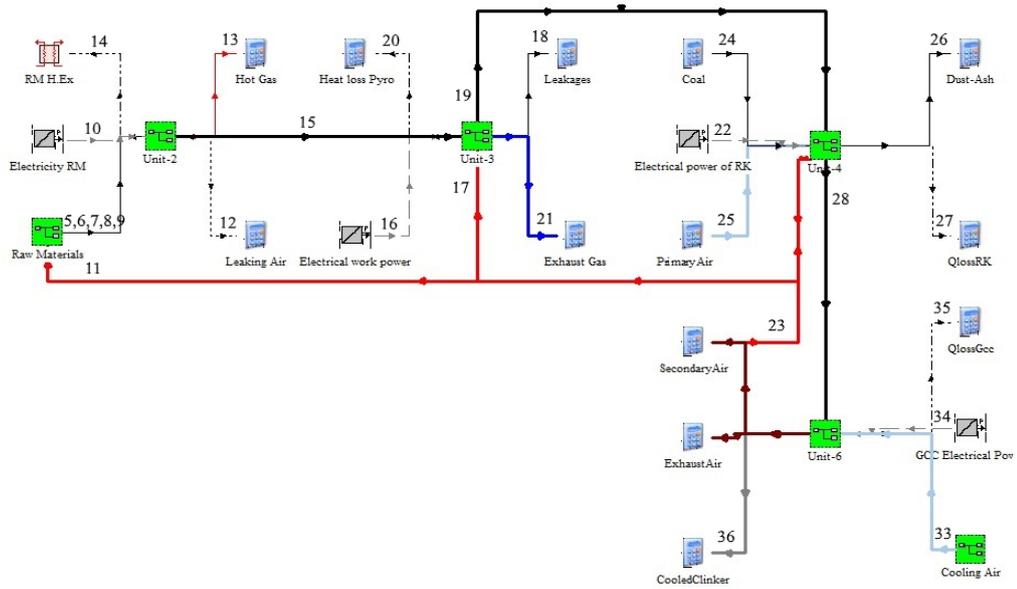
Figure 7.4 The schematic of the TRNSYS model of a cement manufacturing plant

7.1.1 Raw Mill Unit (Unit-2)

The inlet materials of the raw mill are mixed into two input flows. The inlets and outlets of the unit are displayed in Table 7.1.

Table 7.1 Results of the Raw Mill Unit (Unit-2)

Unit-2 Inputs		$\dot{m}$ (kg/h)	T (K)	c_p (kJ/kgK)	$\dot{m}\Delta h$ (kW)		
5,6,7,8,9,11	Raw meal 1	148,559	295	1.1127	229.6		
	Raw meal 2	101,096	518.92	1.2453	8,005.4		
10	Electrical work [30]				3250		
	TOTAL	249,655			11,485		
Unit-2 Outputs		$\dot{m}$ (kg/h)	T (K)	c_p (kJ/kgK)	$\dot{m}\Delta h$ (kW)	T [30] (K)	c_p [30] kJ/kgK
18	Leaking air	4,058	391.81	1.166	133.81	380	1.01
13	Steam	15,028	391.81	1.166	495.55	380	2.01
	Hot Gas	68,346	391.81	1.166	2,187.8	380	1.45
15	Farine	162,223	391.81	1.166	5,349.3	380	0.92

Table 7.1 (Continued)

14	Heat loss				3257.8		
	TOTAL	249,655	391.81	1.166	11,490		
	$\dot{Q}_{Total\ RM}$				3257.8		

The variations in the specific heat and temperature value of the results and the actual data are due to the mixing of the output materials and mechanism of the heat exchanger component in TRNSYS, respectively. The component does not consider heat loss through the walls of the exchanger. Thus, the temperature of the outlets in the model are greater than the actual values.

7.1.2   Pyroprocessing Tower (Unit-3)

The inputs and outputs of the pyroprocessing tower are shown in Table 7.2.

Table 7.2 Results of the pyroprocessing unit (Unit-3)

Unit-3 Inputs		$\dot{m}$ (kg/h)	T (K)	c_p (kJ/kgK)	$\dot{m}\Delta h$ (kW)	T [30] (K)	c_p [30] (kJ/kgK)
Farine		129332	391.81	1.166	4264.7	354	0.92
Moisture of farine [30]		4213	290	4.19	0	300	4.19
Ambient Air [30]		4936	290	1.01	0	300	1.01
15′	Mixture	138481	378.5	1.253	4264.7		
17	Hot gas	66346	1725	1.55	40991.7	1725	1.55
16	Electrical work [30]				5000		
	TOTAL	204827			50256.4		
Unit-3 Outputs		$\dot{m}$ (kg/h)	T (K)	c_p (kJ/kgK)	$\dot{m}\Delta h$ (kW)	T [30] (K)	c_p [30] (kJ/kgK)
18	Leakages	23,690	290	1.253	0	300	0.61
19	Farine	105000	898.32	1.253	22,227.3	1011	1.01
21	Steam	9791	444.16	1.253	525.25	300	2.04
	Exhaust gas	66,346	523.23	1.55	6,662.4	523	1.02

<div align="center">Table 7.2 (Continued)</div>

20	Heat loss		20,848
	TOTAL	204827	50262.9
	$\dot{Q}_{Total\ PT}$		24714.9

*15′ stands for the mixture of the farine, moisture of farine, and leaking air, which correlate with the source fluid flowing through the pyroprocessing tower.

First of all, though the ambient temperature of the pyroprocessing tower is considered to be 290K, the actual value is 300K. Consequently, the results of the simulation differ the reference values of the outputs. The outlet values of Unit-3 are recorded after the input materials flow through five cyclones and a precalciner. The variations in the specific heat values of the outputs are because the input fluids are mixed. The difference in the temperature of the farine (19) is ascribed to the fact that the chemical changes are not evaluated in the model created in this thesis. However, the sensible energy of TNSYS output for (19) is equal to the actual value. The results of (18), (20), (21) attained are in good agreement with the experimental data.

7.1.3   Rotary Kiln (Unit-4)

The results of the rotary kiln unit are listed in Table 7.3. The specific heat values used in Unit-4 are given in Table A.5. Besides, the specific heat value of the output farine of the pyroprocessing tower that continues its way to the rotary kiln, changes due to chemical reactions. The temperature of the precalcined farine (19′) from Table 7.3 is calculated using the properties of farine (19) from Table 7.2 using equation (5.8). According to the e-mail correspondence with A. Atmaca (personal communication, December 17, 2019), since the measurements of each unit have been collected at different times and under various production conditions, there are mismatchments in the mass flowrate of the secondary air provided in the literature, Table A.5 and Table A.7. In order to solve this problem, the initial values of the secondary and primary air are modified in a way that the input mass flowrate and energy rate do not differ from the values gained from [30]. Considering (23) and (25)

in Table 7.3, it is clear that the mass flowrate of secondary and primary air have been decreased and increased, respectively.

Table 7.3 Results of the rotary kiln unit (Unit-4)

Unit-4 Inputs		$\dot{m}$ (kg/h)	T (K)	c_p [30] (kJ/kgK)	$\dot{m}\Delta h$ (kW)	$\dot{m}$ [30] (kg/h)	T [30] (K)
19′	Precalcined farine	105000	1189.6	0.847	22227.3	105000	1110
23	Secondary air	50580	1182	1.09	13660.5	89511	1084
24	Coal	7200	344	1.043	112.604	7200	344
24′	Coal Combustion				63311.65		
25	Primary air	48797	908	1.154	9669.56	9866	320
22	Electrical work [30]				4341.5		
	TOTAL	211577			113323	211577	
Unit-4 Outputs		$\dot{m}$ (kg/h)	T (K)	c_p (kJ/kgK)	$\dot{m}\Delta h$ (kW)	T [30] (K)	c_p [30] (kJ/kg
26	Leakages	12885	893	1.052	2270.1	710	1.052
28	Clinker	65200	1595	0.847	20018.8	1550	0.847
17′	Hot gas	133492	1126	1.177	36486.8	1120	1.177
27	Heat loss				12220.4		
	TOTAL				110995		
	$\dot{Q}_{Total\ RK}$				40887		

Temperature of the source side fluid, which splits into two fluid flows (26 and 28), is higher compared to the measured values because the combustion air, which enforces the clinkerization process, is in a very high temperature. Comparison of the results of Unit-4 with the data from literature demonstrate good consonance.

7.1.4 Grate Clinker Cooler (Unit-6)

Mass flowrate of the input fresh air is increased in order to provide the minimum air required for burning coal in the precalciner. The inputs and outputs of Unit-6 are represented in Table 7.4.

Table 7.4 Results of the grate clinker cooler unit (Unit-6)

Unit-6 Inputs		$\dot{m}$ (kg/h)	T (K)	c_p (kJ/kgK)	$\dot{m}\Delta h$ (kW)	T [30] (K)	c_p [30] kJ/kgK
28	Clinker	65200	1595	0.847	20018.8	1595	1.21
33	Air	173226	313	0.99	1095.65	313	0.99
34	Electrical work [30]				1873		
	TOTAL	249655			22987.45		
Unit-6 Outputs		$\dot{m}$ (kg/h)	T (K)	c_p (kJ/kgK)	$\dot{m}\Delta h$ (kW)	T [30] (K)	c_p [30] (kJ/kgK
36	Clinker	65200	394	0.847	1594	390	0.88
	Air	173226	700	0.99	19233	823.32	0.99
35	Heat loss				2160		
	TOTAL	249655	391.81	1.166	22987		
	$\dot{Q}_{Total\ GCC}$				18423		

The difference in the specific heat value of the input clinker is because chemical changes are not considered in TRNSYS. Additionally, the temperature of the output air is lower than the actual value because the cross-flow heat exchanger used in the model does not have the capability of inducing more heat exchange for the specified air quantity.

7.2 Solar-Integrated Cement Plant Model

7.2.1 Ambient Conditions and Solar Irradiation

Before presenting the models' outputs, hourly ambient and radiation conditions at which the solar field operates are demonstrated. In order to run a simulation for one year and to predict the performance of the cement plant located in Gaziantep-Turkey, a typical Meteorological Year Version 2 (TMY2) of Gaziantep city is used at latitude 37.0660 0N and longitude 37.3781 0E. On the other hand, the simulation is conducted for one year using a typical Meteorological Year Version 2 (TMY2) of Upington-South Africa, at latitude 28.3953 0S and longitude 21.2368 0E in order to compare the results. The reason behind this choice is that South Africa has the finest solar resources with the annual DNI of about 2800-3000 kWh/m^2.

Figure 7.5, 7.6, and 7.7 show the direct normal solar irradiation, wind speed and dry bulb temperature for Gaziantep over one year. The annual DNI of Gaziantep is found to be 1390 kWh/m^2. According to the profiles, the peak direct normal radiation is approximately 975 W.m^{-2}. The peak ambient temperature in a year is 43$^{\circ C}$ with the maximum wind speed is 15.575 m/s.
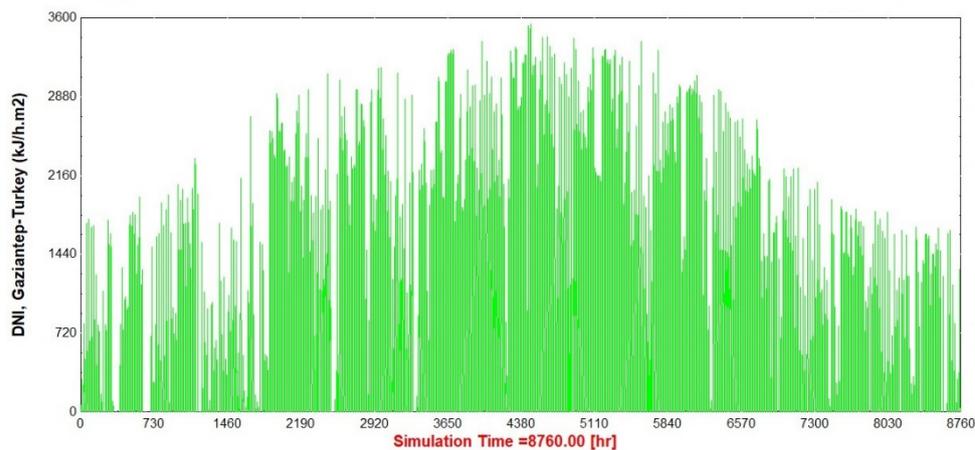
Figure 7.5 Annual DNI (kJ/h.m^2) profile, Gaziantep-Turkey
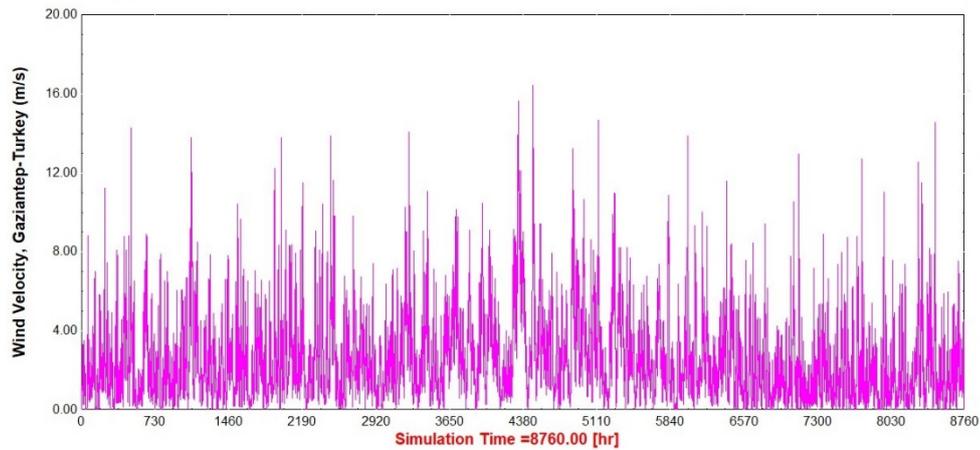
Figure 7.6 Wind velocity (m/s) profile, Gaziantep-Turkey
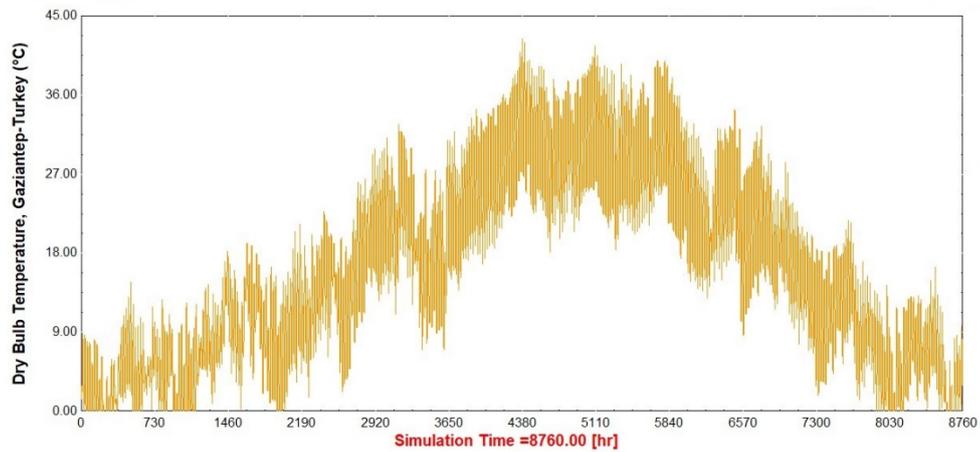
Figure 7.7 Dry bulb temperature (°C) profile, Gaziantep-Turkey

Figure 7.8, 7.9 and 7.10 show the direct normal solar irradiation, wind speed and dry bulb temperature over one year for Upington-South Africa, respectively. The peak direct normal radiation is approximately 1000 $W.m^{-2}$. This period is characterized by high ambient temperature with the peak $43^{\circ C}$ and maximum wind speed is 12.8 m/s.
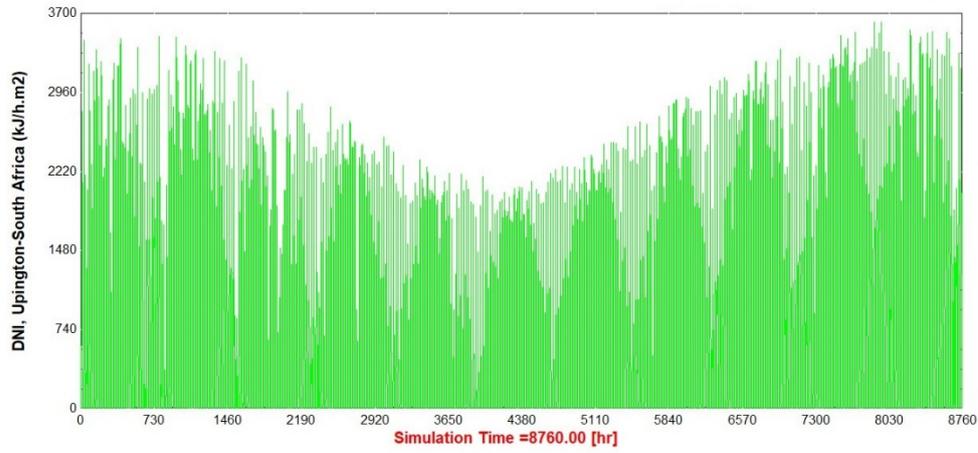
Figure 7.8 Annual DNI (kJ/h.m^2) profile, Upington-South Africa
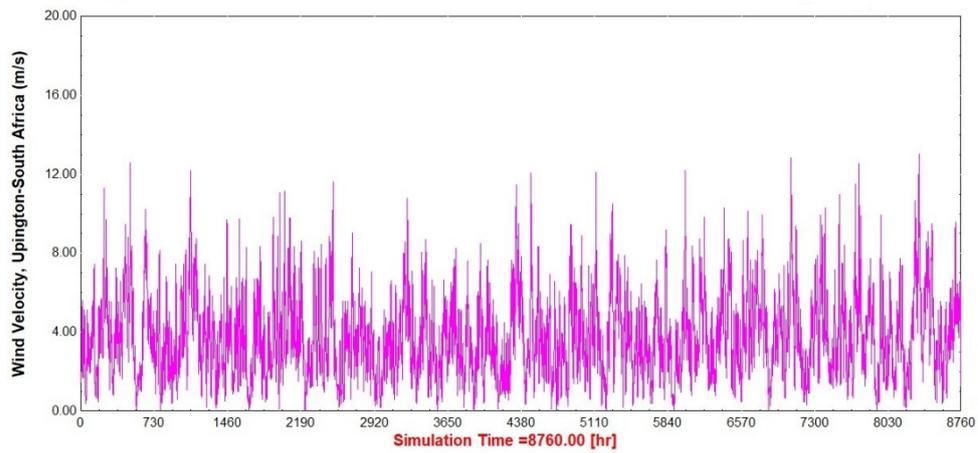
Figure 7.9 Wind velocity (m/s) profile, Upington-South Africa
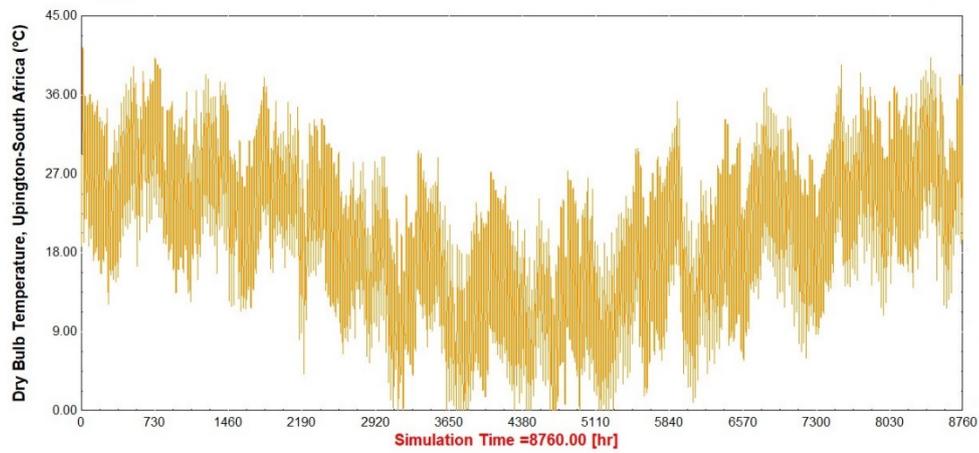
Figure 7.10 Dry bulb temperature (°C) profile, Upington-South Africa

7.2.2 Solar Thermal Electrical Power

For a hybrid cement plant, the solar field is connected with two fuel combustion systems that simulate to maintain the required process temperature for the calcination and clinkerization processes in the rotary kiln and the turbine entry when solar energy is inadequate. The electric power output of the generator is simulated at $1300^{°C}$ temperature using 1000 heliostat mirrors. The receiver aperture area and a heliostat surface area are set to 25 m^2 and 100 m^2, respectively. Solar power generated by the heliostat field is plotted for Gaziantep-Turkey, Figure 7.11, and Upington-South Africa, Figure 7.12.
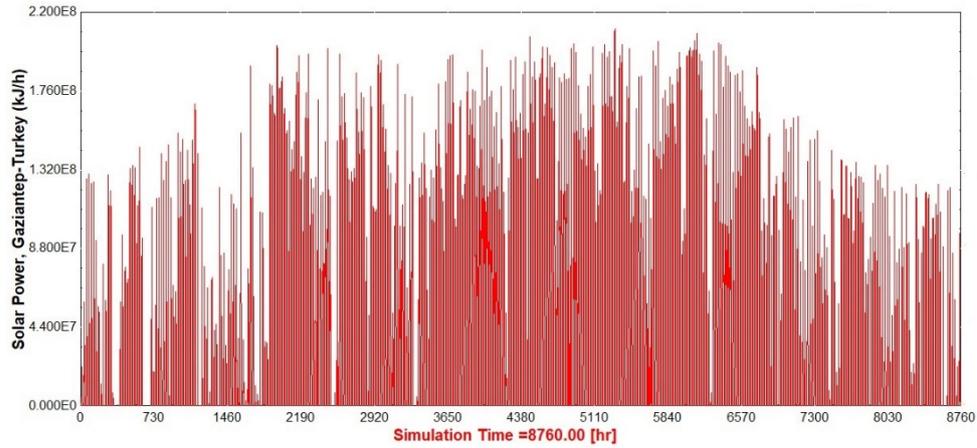
Figure 7.11 Generated power by heliostat solar field (kJ/h), Gaziantep-Turkey
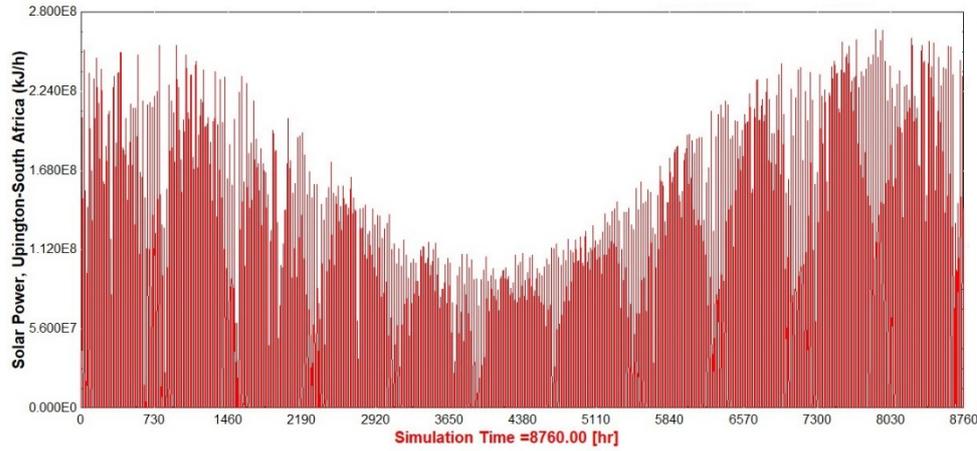
Figure 7.12 Generated power by heliostat solar field (kJ/h), Upington-South Africa

According to the results, total power generated by the solar field is 87,322 and 112,709 MWh for Gaziantep and Upington, respectively.

$$P_{(t)} = \int_0^{8760} \frac{\dot{Q}_{receiver-Gaziantep,Turkey}}{3600} dt \simeq 87322 \text{ MWh} \tag{7.1}$$

$$P_{(t)} = \int_0^{8760} \frac{\dot{Q}_{receiver-Upington,South\ Africa}}{3600} dt \simeq 112709 \text{ MWh} \tag{7.2}$$

The results prove that the solar power produced by the modeled solar field is higher in Upington-South Africa.

The solar-heated pressurized air in the receiver is partially used to produce electricity by a generator. Simulated peak electric power output is found to be 16.33 MW for Gaziantep as illustrated in Figure 7.13. Total amount of electrical energy output of the system is calculated to be 63362 MWh over one year, equation 7.3, and the average value of the power generated for a year is 7.23 MW, equation 7.4. This energy can partially supply the electrical demand of the main units of a cement plant that require 14.46 MW of electrical power.

$$P_{(t)} = \int_{0}^{8760} \frac{\dot{W}}{3600} dt \simeq 63362 \text{ MWh} \tag{7.3}$$

$$\overline{P}_{(t)} = \frac{1}{8760} \int_{0}^{8760} \frac{\dot{W}}{3600} dt \simeq 7.23 \text{ MW} \tag{7.4}$$
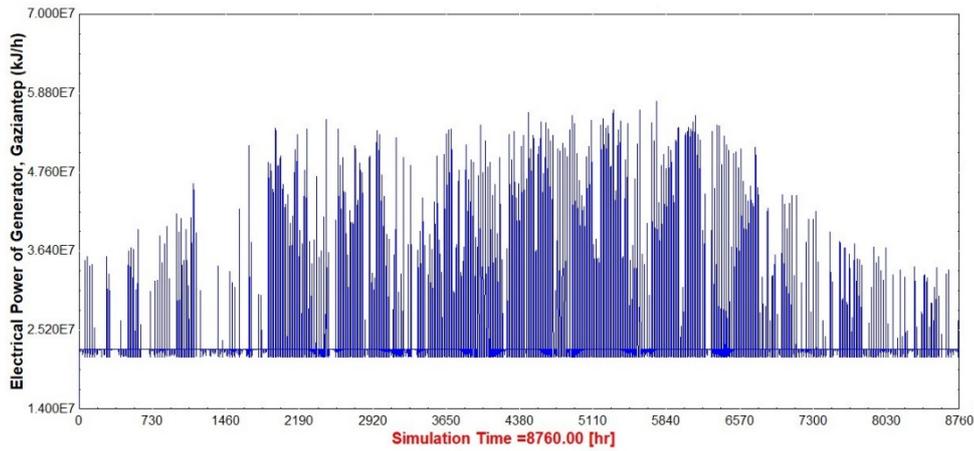
Figure 7.13 Electric power of generator (kJ/h), Gaziantep-Turkey

With the same solar model, the peak electric power output for Upington is found to be 18.27 MW, Figure 7.14. Total amount of electrical energy output of the system is 64340 MWh over one year and the average value of the power generated for a year is 7.34 MW, which are calculated from equation 7.3 and 7.4.
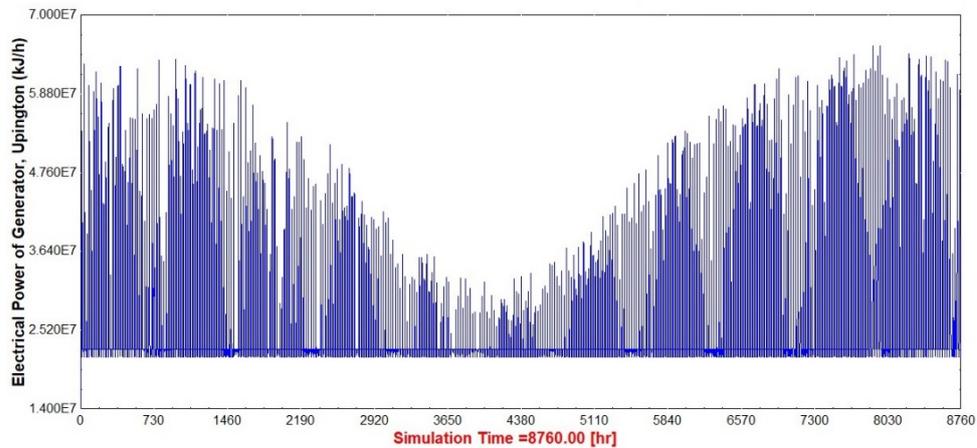
Figure 7.14 Electric power of generator (kJ/h), Upington-South Africa

It is explicit that the electrical power generated in Upington is more than the power generated under Gaziantep weather conditions. The reason for that is the higher power generation by the heliostat solar field in Upington-South Africa.

7.2.3 Solar-integrated Model of the Conventional Cement Plant (Model-2)

The steady state modeling of the cement plant proved that annually 63,072 tonnes of fossil fuel is required to produce 569,392 tonnes clinker. 62.5% of the solar-heated air provided by the air-receiver is consumed in rotary kiln in order to supply the energy of the endothermic process of the clinker formation. The results of the TRNSYS model for the solar cement plant are presented in this section.

The temperature profiles of the solar-heated air from the air-receiver for Gaziantep-Turkey, figure 7.15, and for Upington-South Africa, figure 7.16, are demonstrated. According to the plots, the air is heated solely by solar resources to the temperatures between $430^{\circ C}$ to $1360^{\circ C}$ in Gaziantep-Turkey. However, due to the better weather conditions in Upington-South Africa, the temperature ranges between $430^{\circ C}$ and $1670^{\circ C}$.
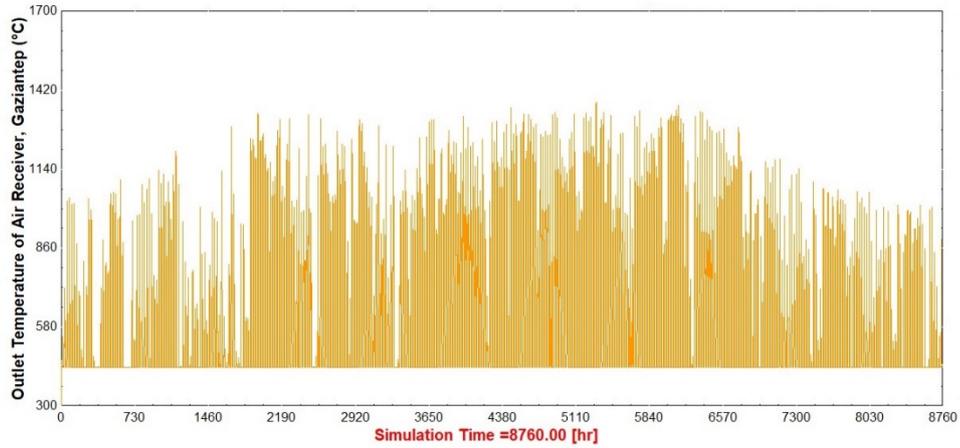
Figure 7.15 $T_{out\ Air\ Receiver}$ (°C) Profile, Gaziantep-Turkey
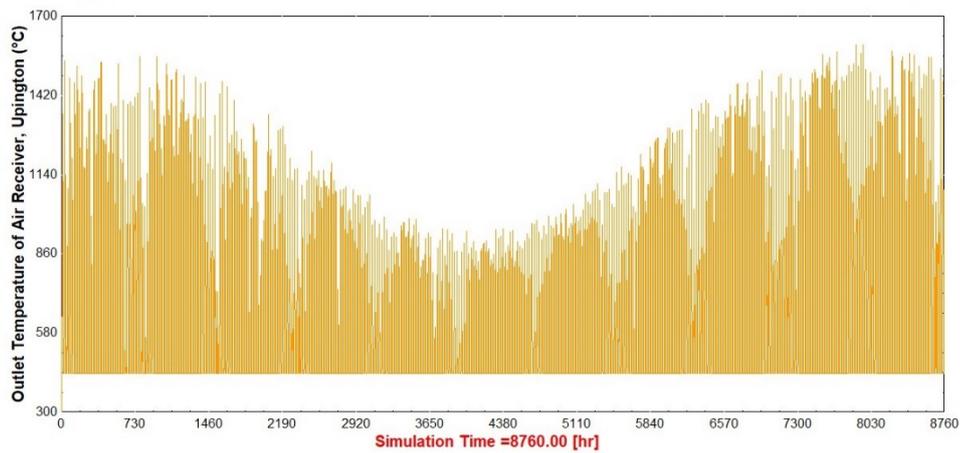
Figure 7.16 $T_{out\ Air\ Receiver}$ (°C) Profile, Upington-South Africa

Moreover, figure 7.17 and 7.18 represent the fuel consumption rates in a conventional and a solar hybridized cement plant for Gaziantep-Turkey and Upington-South Africa. As shown in the figures, the fuel mass flowrate in the rotary kiln of the conventional cement plant is 7200 kg/h. However, the fossil fuel mass flowrate in the solar cement plant is unsteady. Total fuel consumption of solar-integrated plant model is calculated:

$$m_{(t)} = \int_0^{8760} \frac{\dot{m}_{fossil\ fuel-Gaziantep,Turkey}}{1000} dt \simeq 58,800 \text{ tonnes/year} \tag{7.5}$$

129

$$m_{(t)} = \int_0^{8760} \frac{\dot{m}_{fossil\ fuel-Upington,South\ Africa}}{1000} dt \simeq 55,713\ \text{tonnes/year} \qquad (7.6)$$
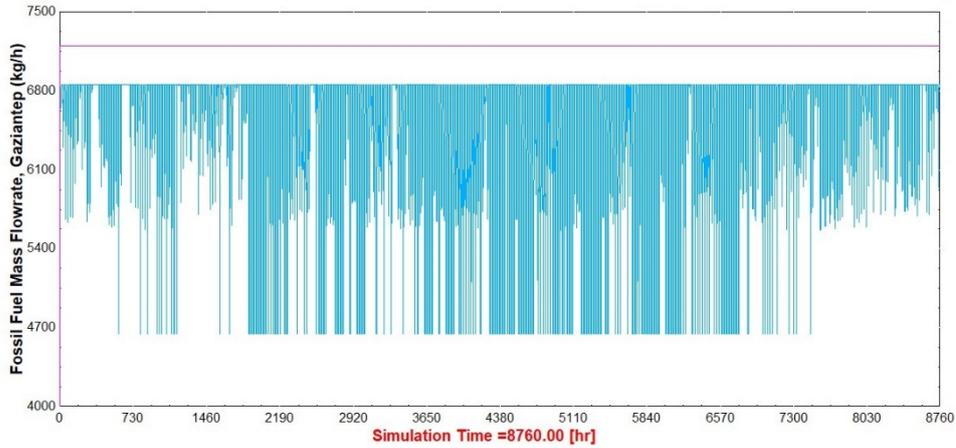
Figure 7.17 Fuel mass flowrate (kg/h) in a conventional vs. solar cement plant, Gaziantep-Turkey
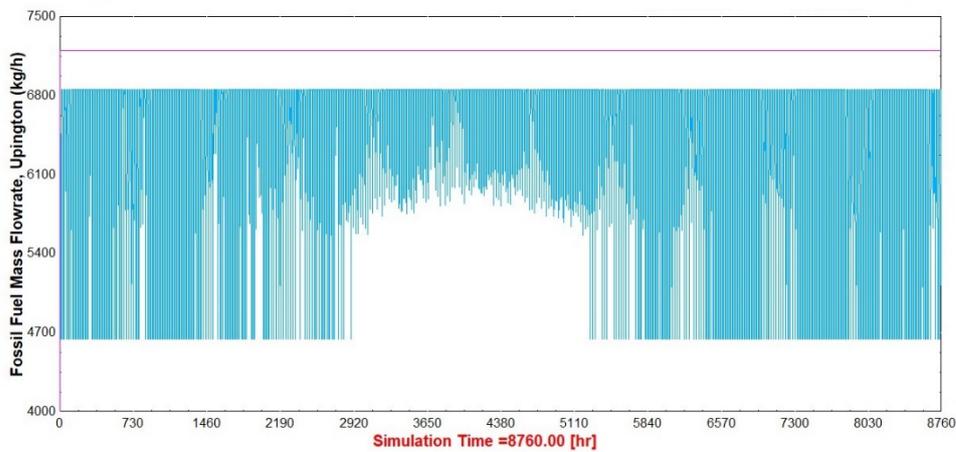
Figure 7.18 Fuel mass flowrate (kg/h) in a conventional vs. solar cement plant, Upington-South Africa

The results show that 63072 tonnes/year of fuel is consumed in a conventional cement plant, although about 58,800 tonnes/year fossil fuel (coal) is consumed in a solar cement plant (Model-2) in Gaziantep. However, coal consumption is 55,713

130

tonnes/year in Upington-South Africa, which means 3,100 tonnes/year less coal can be burnt to produce the same amount of clinker in Upington.

The ultimate aim of this thesis is to evaluate how much CO_2 emission can be mitigated in the solar-integrated cement plant (Model-2). The CO_2 emission rates are displayed in 7.12.
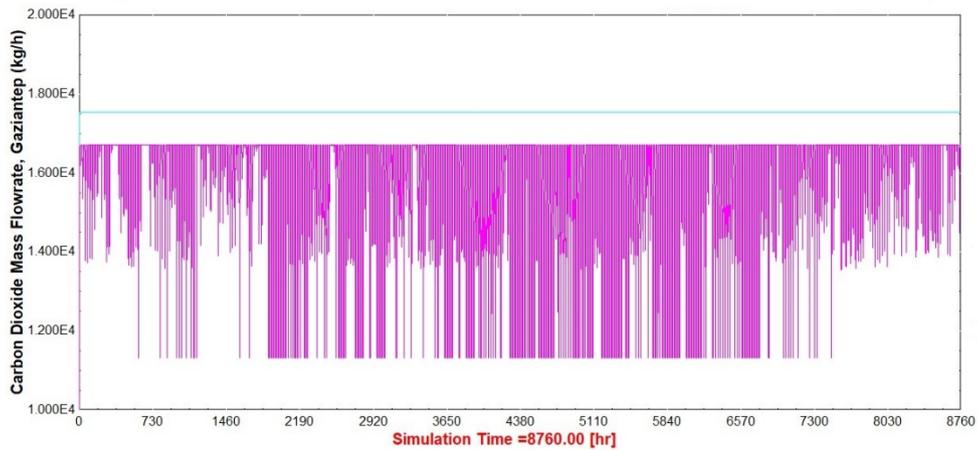
Figure 7.19 CO_2 emission flow rate in a conventional vs. a solar-hybridized cement plant, Gaziantep-Turkey
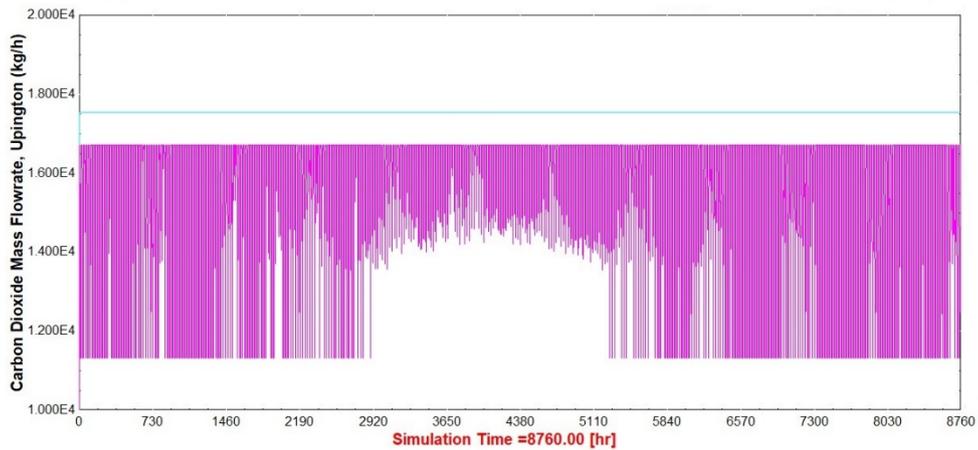
Figure 7.20 CO_2 emission flow rate in a conventional vs. a solar-hybridized cement plant, Upington-South Africa

$$m_{(t)} = \int_0^{8760} \frac{\dot{m}_{CO_2-Gaziantep,Turkey}}{1000} dt \simeq 138{,}100 \text{ tonnes/year} \qquad (7.7)$$

$$m_{(t)} = \int_0^{8760} \frac{\dot{m}_{CO_2-Upington,South\ Africa}}{1000} dt \simeq 135{,}754 \text{ tonnes/year} \qquad (7.8)$$

The results of the TRNSYS indicate that 153,665.4 tonnes/year of CO_2 is emitted to the environment in a conventional cement plant. According to the results, approximately 138,100 and 135,754 tonnes/year CO_2 is produced in a solar-integrated rotary kiln in Gaziantep-Turkey and Upingtopn-South Africa, respectively. Because, more fossil fuel is burnt in a conventional cement plant, the quantity of the CO_2 released into the atmosphere is more than the solar cement plant (Model-2). In the solar-integrad plant, Model-2, less fossil fuel is used for combustion and less carbon dioxide is released in the system.

7.2.4 Solar-integrated Model of the Conventional Cement Plant With A Preheater before Pyroproprocessing Unit (Model-3)

In this section, in addition to the consumption of solar energy in the rotary kiln (Model-2) discussed in the previous section, a proportion of the solar-heated air is used to preheat the raw meal (farine) entering the pyroprocessing tower. The results of the TRNSYS model for the second solar cement plant, Model-3, is presented.

The system is run for Gaziantep-Turkey using a typical Meteorological Year Version 2 (TMY2). Initially, the temperature profiles of the preheated farine and precalcined farine are plotted. Then, the required outlet temperature of the rotary kiln's combustion chamber is examined. Finally, total CO_2 emission and fossil fuel consumption are calculated and compared with the conventional and solar-integrated rotary kiln cement plant.
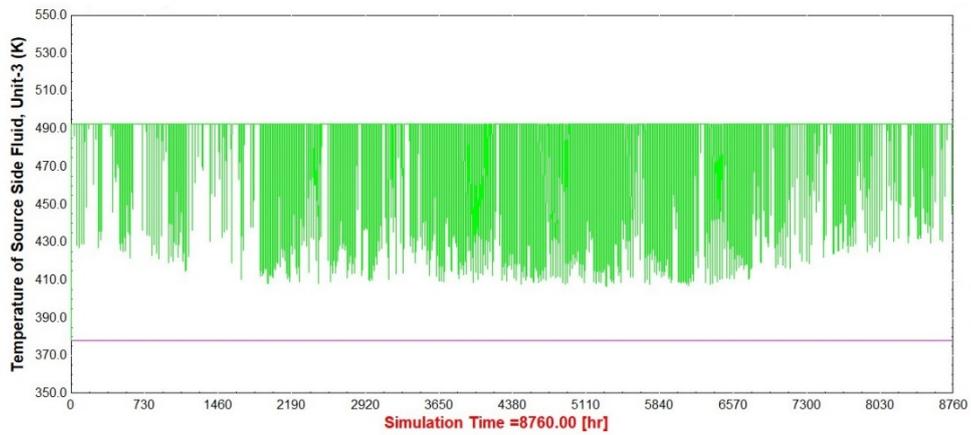
Figure 7.21 Temperature (K) profile of preheated farine, Model-3

According to the results observed in Figure 7.21, temperature of the farine that is the product of the raw mill (Unit-2), 15-Table 7.1, rises from 391.8K up to an average value of 455K.

The preheated farine continues its way to the pyroprocessing unit. Expectedly, Figure 7.22 shows that the temperature of the precalcined farine (19′) increases in comparison with its value in Table 7.3.
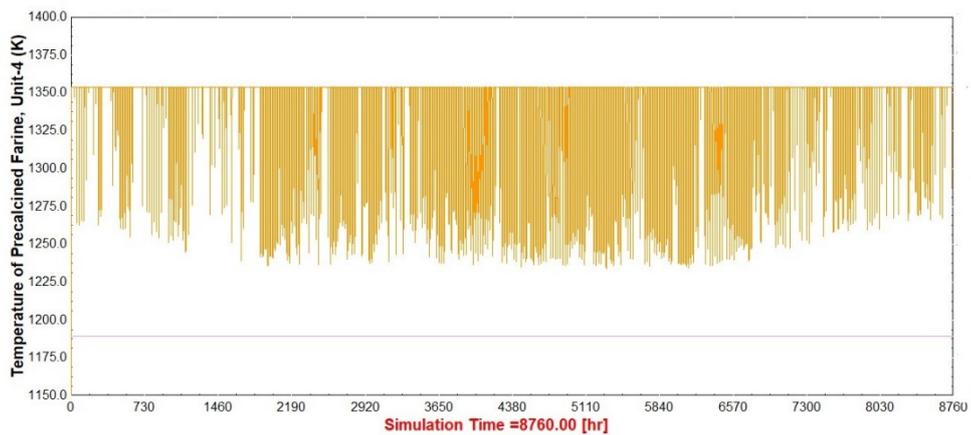
Figure 7.22 Temperature (K) profile of the precalcined farine, Model-3

133

Because of the rapid increase of the temperature of the precalcined farine from 1189.6K to temperature ranges between 1230K and 1350K, the sensible heat of the precalcined farine rises and calcination process can be completed in the pyroprocessing tower. As a result, less energy is needed to run the chemical reaction of clinker formation. The outlet temperature of the combustion chamber in the rotary kiln unit (Unit-4) is calculated and demonstrated in Figure 7.23. The results prove that the outlet temperature required decreases from $1850^{\circ C}$ to the temperature ranges between $1720^{\circ C}$ to $1820^{\circ C}$. Since the outlet temperature of the combustion chamber falls, less fossil fuel is burnt in order to reach the specified temperature. The fuel consumption mass flowrate is sketched.
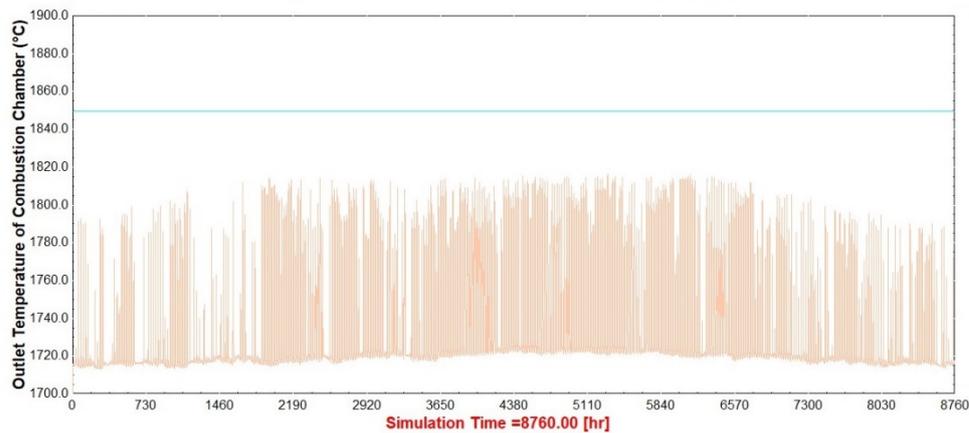
Figure 7.23 Outlet temperature of the combustion chamber (°C), Model-3

Fossil fuel consumption rate of the system is given in Figure 7.24. Total mass of the fossil fuel consumed in Model-3 is calculated.

$$m_{(t)} = \int_0^{8760} \frac{\dot{m}_{fossil\ fuel-Gaziantep,Turkey}}{1000} dt \simeq 51,805 \text{ tonnes/year} \qquad (7.9)$$

TRNSYS results indicate that 51,805 tonnes/year of fossil fuel (coal) is consumed in the solar-integrated cement plant, Model-3.
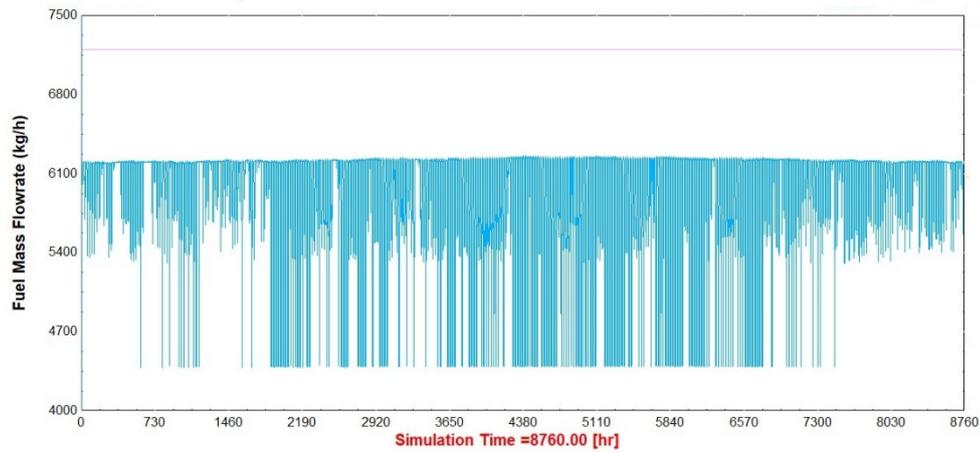
Figure 7.24 Fuel mass flowrate (kg/h), Model-3

Finally, the CO_2 emission rate of the solar-integrated cement plant (Model-3) is displayed, Figure 7.25, and total mass of the CO_2 released into the atmosphere is calculated for a year.

$$m_{(t)} = \int_0^{8760} \frac{\dot{m}_{CO_2-Gaziantep,Turkey}}{1000} dt \simeq 126{,}230 \text{ tonnes/year} \qquad (7.10)$$
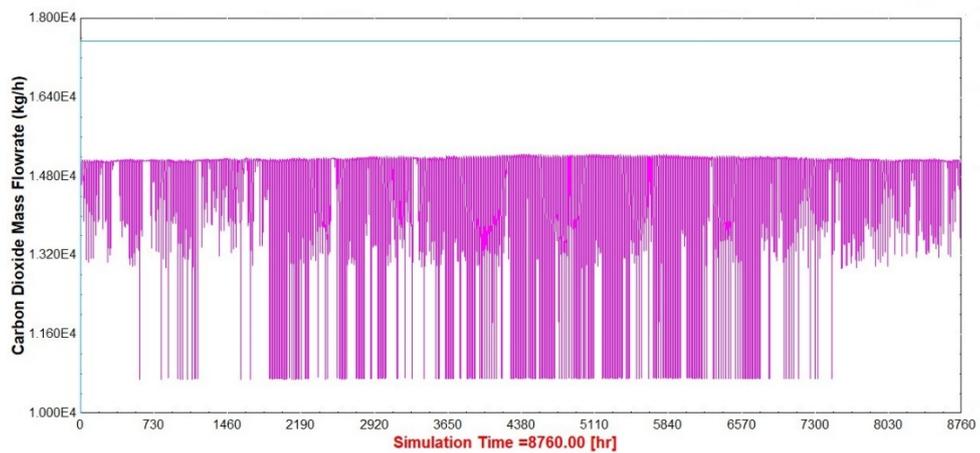
Figure 7.25 CO_2 emission flow rate, Model-3

The results of the Model-1, Model-2 and Model-3 are tabulated in order to compare the result.

Table 7.5 Results of the cement plant Mode-1, Mode-2 and Mode-3

Results	Total Fuel Consumption (tonnes/year)	Total CO_2 Emission (tonnes/year)
Model-1 Gaziantep, Turkey	63,072	153,665.4
Model-2 Gaziantep, Turkey	58,800 (-6.7%)	138,100 (-10.13%)
Model-2 Upington, South Africa	55,713 (-11.67%)	135,754 (-11.66%)
Model-3 Gaziantep, Turkey	51,80 (-17.86%)	126,230 (-17.85%)

Table 7.5 shows total fossil fuel consumed and CO_2 released over a year in the models discussed and the reduction rates are calculated. The most efficient model in the sense of mitigation in coal consumption and CO_2 emission is Model-3 with the highest reduction rates. It is proved that by using solar thermal in the most energy-intensive industry of the world, promising results are achieved.

CHAPTER 8

CONCLUSIONS AND FUTURE WORK

In this work, TRNSYS models for a conventional and two solar-based cement plants are developed. The detailed properties of the input materials of a cement industry located in Gaziantep-Turkey, are used to simulate the system. The novelty of this study is simulation of a cement plant in TRNSYS and consideration of the impacts of solar thermal energy in the fuel consumption and detrimental GHG emission rates. Primarily, a conventional cement plant (Model-1) in steady-state mode with constant input materials is simulated. In this model, the mass flowrates, temperatures, sensible heats and heat losses of the main units of the plant (Raw mill, Pyroprocessing tower, Rotary kiln, Grate clinker cooler) are examined. The results of the system shows good agreement with the experimental data. Secondly, a solar heliostat field is integrated to the rotary kiln of the model using STEC library (Model-2). Solar-heated air is mixed with the air consumed to run the combustion process in the combustion chamber of the rotary burner. The remainder of the solar-heated air is used in a gas turbine-generator model in order to produce electricity. The simulations are conducted considering the typical weather conditions for Gaziantep-Turkey and Upington-South Africa. The results show that the fuel consumption and CO_2 emissions fall by approximately 10.16% and 10.15% in Gaziantep-Turkey and %12.3 and %27.9 in Upington-South Africa for Model-2, respectively. Finally, some modifications have been made in the solar-hybridized model in order to use solar thermal in both the rotary kiln and pyroprocessing unit (Model-3). The air mass flowrate of the air-receiver is increased in order to provide the system with 75000kg/h solar-heated air in order to preheat the farine going to the pyroprocessing tower. The fuel consumption and detrimental emission rates of the plants are compared with each other in fuel consumption and detrimental emission rates. According to the results, the best results are gained in model-3 with 17.86% and

17.85% reduction in annual coal usage and CO_2 emission, respectively. Last but not least, not only does the hybridized plants supply about half of the electrical work demand of a cement plant, but also by integrating a heliostat solar field to a conventional cement plant, more than 10% decline is achieved in annual fossil fuel usage and CO_2 emission.

The presented study is a foundation and a starting point for further studies. Initially, effect of adding a rock bed solar storage system to the solar field can be considered in the fuel consumption and emission rates. Secondly, an interesting improvement could be using a secondary concentrator such as a CPC in the solar field to evaluate the performance enhancement rate of the heliostat solar field with a pressurized air receiver. Another potential future study is installing a waste heat recovery steam generator for further electrical energy production.

REFERENCES

[1]   Philip A. Alsop, *The Cement Plant Operations Handbook*, 7th ed. Tradeship Publications Ltd, 2019.

[2]   R. Woodward and N. Duffy, "Cement and concrete flow analysis in a rapidly expanding economy: Ireland as a case study," *Resour. Conserv. Recycl.*, 2011.

[3]   U.S. Geological Survey, "Mineral Commodity SummariesNo Title," 2017.

[4]   A. F. Pales, P. Levi, and T. Vass, "Tracking Industry," 2019.

[5]   R. S. González and G. Flamant, "Technical and economic feasibility analysis of using concentrated solar thermal technology in the cement production process: Hybrid approach-a case study," *J. Sol. Energy Eng. Trans. ASME*, 2014.

[6]   N. A. Madlool, R. Saidur, M. S. Hossain, and N. A. Rahim, "A critical review on energy use and savings in the cement industries," *Renewable and Sustainable Energy Reviews*. 2011.

[7]   J. V. . Sharabaroff, Alexander; Folliet, Michel; Rivas Saiz, Milagros; Shah, "IMPROVING THERMAL AND ELECTRIC ENERGY EFFICIENCY AT CEMENT PLANTS: INTERNATIONAL BEST PRACTICE," Washington, D.C, 2017.

[8]   E. Worrell, N. Martin, and L. Price, "Potentials for energy efficiency improvement in the US cement industry," *Energy*, 2000.

[9]   Moses P.M. Chinyama, "Alternative Fuels in Cement Manufacturing," in *Alternative Fuel*, M. Manzanera, Ed. 2011.

[10]   J. Sirchis, *Energy Efficiency in the Cement Industry*. Oporto: CRC Press, 1990.

[11]   M. Schuhmacher, J. L. Domingo, and J. Garreta, "Pollutants emitted by a

cement plant: Health risks for the population living in the neighborhood," *Environ. Res.*, 2004.

[12] C. Chen, G. Habert, Y. Bouzidi, A. Jullien, and A. Ventura, "LCA allocation procedure used as an incitative method for waste recycling: An application to mineral additions in concrete," *Resour. Conserv. Recycl.*, 2010.

[13] A. Gupta and M. S. Cullinen, "Analysis of the Cement Industry, Carbon War Room," Washington, D.C.

[14] Pao K. Wang, "Global Warming- Greenhouse Gases and Climate."

[15] T. R. Anderson, E. Hawkins, and P. D. Jones, "CO_2, the greenhouse effect and global warming: from the pioneering work of Arrhenius and Callendar to today's Earth System Models," *Endeavour*, 2016.

[16] Z. Utlu, Z. Sogut, A. Hepbasli, and Z. Oktay, "Energy and exergy analyses of a raw mill in a cement production," *Appl. Therm. Eng.*, 2006.

[17] A. Atmaca, M. Kanoglu, and M. Gadalla, "Thermodynamic analysis of a pyroprocessing unit of a cement plant: A case study," *Int. J. Exergy*, 2012.

[18] A. Atmaca, "ENERGY, EXERGY AND EXERGOECONOMIC ASSESSMENT OF A DRY TYPE ROTARY KILN," *ANADOLU Univ. J. Sci. Technol. A - Appl. Sci. Eng.*, 2018.

[19] T. Engin and V. Ari, "Energy auditing and recovery for dry type cement rotary kiln systems - A case study," *Energy Convers. Manag.*, 2005.

[20] A. F. Savaş and A. Kolip, "Comparative energy and exergy analyses of a serial and parallel flow four-stage cyclone pre-calciner cement plant," *Int. J. Exergy*, 2015.

[21] H. Mikulčić *et al.*, "The application of CFD modelling to support the reduction of CO 2 emissions in cement industry," *Energy*, 2012.

[22] S. Karellas, A. D. Leontaritis, G. Panousis, E. Bellos, and E. Kakaras,

"Energetic and exergetic analysis of waste heat recovery systems in the cement industry," *Energy*, 2013.

[23] Q. Yin, W. J. Du, and L. Cheng, "Optimization design of waste heat power generation systems for cement plants based on the thermal resistances analyses," *Int. J. Heat Mass Transf.*, 2018.

[24] Z. C. J.W. Wandrasz, K. Pikoń, Ed., "Waste to Energy and Environment," Department of Technologies and Installations for Waste Management Silesian University of Technology.

[25] M. Georgiopoulou and G. Lyberatos, "Life cycle assessment of the use of alternative fuels in cement kilns: A case study," *J. Environ. Manage.*, 2018.

[26] ECOFYS, "Market opportunities for use of alternative fuels in cement plants across the EU," 2016.

[27] G. Flamant *et al.*, "Solar processing of reactive particles up to 900°C, the SOLPART project," in *AIP Conference Proceedings*, 2018.

[28] SOLPART, "High temperature Solar-Heated Reactors for Industrials Production of Reactive Particulates," *European Union's Horizon 2020 research and innovation programme*, 2016. .

[29] A. Meier, N. Gremaud, and A. Steinfeld, "Economic evaluation of the industrial solar production of lime," *Energy Convers. Manag.*, 2005.

[30] A. Atmaca, "INCREASING EFFICIENCY AND REDUCING POLLUTANTS IN CEMENT INDUSTRY BY THERMODYNAMIC AND EXERGOECONOMIC METHODS," University of Gaziantep, 2014.

[31] A. Bosoaga, O. Masek, and J. E. Oakey, "CO_2 Capture Technologies for Cement Industry," in *Energy Procedia*, 2009.

[32] A. N. and J. G. Jang, "Recent Progress in Green Cement Technology Utilizing Low-Carbon Emission Fuels and Raw Materials: A Review," 2019.

[33] S. Khurana, R. Banerjee, and U. Gaitonde, "Energy balance and cogeneration for a cement plant," *Appl. Therm. Eng.*, 2002.

[34] J. S. Damtoft, J. Lukasik, D. Herfort, D. Sorrentino, and E. M. Gartner, "Sustainable development and climate change initiatives," *Cem. Concr. Res.*, 2008.

[35] W. B. Stine and M. Geyer, *Power From The Sun*. California State Polytechnic University Pomona, California 91768 USA, 2001.

[36] INSHIP Cooperative, "INSHIP project," 2017.

[37] N. A. Madlool, R. Saidur, N. A. Rahim, and M. Kamalisarvestani, "An overview of energy savings measures for cement industries," *Renewable and Sustainable Energy Reviews*. 2013.

[38] T. Gao, L. Shen, M. Shen, L. Liu, and F. Chen, "Analysis of material flow and consumption in cement production process," *J. Clean. Prod.*, 2016.

[39] A. Atmaca and N. Atmaca, "Determination of correlation between specific energy consumption and vibration of a raw mill in cement industry," *Anadolu Univ. J. Sci. Technol. Appl. Sci. Eng.*, 2016.

[40] M. Z. Sogut, Z. Oktay, and A. Hepbasli, "Energetic and exergetic assessment of a trass mill process in a cement plant," *Energy Convers. Manag.*, 2009.

[41] A. Kolip and A. F. Savas, "Energy and exergy analyses of a parallel flow, four-stage cyclone precalciner type cement plant," *Int. J. Phys. Sci.*, 2010.

[42] G. Kabir, A. I. Abubakar, and U. A. El-Nafaty, "Energy audit and conservation opportunities for pyroprocessing unit of a typical dry process cement plant," *Energy*, 2010.

[43] H. Mikulčić, E. Von Berg, M. Vujanović, P. Priesching, R. Tatschl, and N. Duić, "CFD analysis of a cement calciner for a cleaner cement production," in *Chemical Engineering Transactions*, 2012.

[44] Ü. Çamdali, A. Erişen, and F. Çelen, "Energy and exergy analyses in a rotary burner with pre-calcinations in cement production," *Energy Convers. Manag.*, 2004.

[45] W. N. Wu, X. Y. Liu, Z. Hu, R. Zhang, and X. Y. Lu, "Improving the sustainability of cement clinker calcination process by assessing the heat loss through kiln shell and its influencing factors: A case study in China," *J. Clean. Prod.*, 2019.

[46] Z. Söğüt, Z. Oktay, and H. Karakoç, "Mathematical modeling of heat recovery from a rotary kiln," *Appl. Therm. Eng.*, 2010.

[47] A. C. Caputo, P. M. Pelagagge, and P. Salini, "Performance modeling of radiant heat recovery exchangers for rotary kilns," *Appl. Therm. Eng.*, 2011.

[48] E. Mastorakos, A. Massias, C. D. Tsakiroglou, D. A. Goussis, V. N. Burganos, and A. C. Payatakes, "CFD predictions for cement kilns including flame modelling, heat transfer and clinker chemistry," *Appl. Math. Model.*, 1999.

[49] S. Wirtz, C. Pieper, F. Buss, M. Schiemann, S. Schaefer, and V. Scherer, "Impact of coating layers in rotary cement kilns: Numerical investigation with a blocked-off region approach for radiation and momentum," *Therm. Sci. Eng. Prog.*, 2020.

[50] L. G. Lauredan, H. Florian, and D. Jean, "A wall heat transfer correlation for the baffled-rotary kilns with secondary air flow and recycled materials inlet," *Exp. Therm. Fluid Sci.*, 2014.

[51] D. A. Granados, F. Chejne, J. M. Mejía, C. A. Gómez, A. Berrío, and W. J. Jurado, "Effect of flue gas recirculation during oxy-fuel combustion in a rotary cement kiln," *Energy*, 2014.

[52] M. Wang, B. Liao, Y. Liu, S. Wang, S. Qing, and A. Zhang, "Numerical simulation of oxy-coal combustion in a rotary cement kiln," *Appl. Therm. Eng.*, 2016.

[53]   A. Sagastume Gutiérrez, J. B. Cogollos Martínez, and C. Vandecasteele, "Energy and exergy assessments of a lime shaft kiln," *Appl. Therm. Eng.*, 2013.

[54]   T. J. B. Taweel, E. Sokolova, V. Sergeev, and D. B. Solovev, "Energy and Exergy Analysis of Clinker Cooler in the Cement Industry," in *IOP Conference Series: Materials Science and Engineering*, 2018.

[55]   J. U. Ahamed, N. A. Madlool, R. Saidur, M. I. Shahinuddin, A. Kamyar, and H. H. Masjuki, "Assessment of energy and exergy efficiencies of a grate clinker cooling system through the optimization of its operational parameters," *Energy*, 2012.

[56]   M. O. Amole, "PERFORMANCE EVALUATION OF A GRATE COOLER IN A CEMENT MANUFACTURING INDUSTRY IN NIGERIA," *Int. J. Sci. Eng. Appl. Sci.*, vol. 4, no. 03, April 2018, p. 14, 2018.

[57]   D. Touil, H. F. Belabed, C. Frances, and S. Belaadi, "Heat exchange modeling of a grate clinker cooler and entropy production analysis," *Int. J. Heat Technol.*, 2005.

[58]   R. Ahmad, T. A. Khan, and V. Agarwal, "Mass and Energy Balance in Grate Cooler of Cement Plant," *Int. J. Sci. Eng. Technol.*, 2013.

[59]   Q. Cao, Z. Cui, Q. Sun, and L. Cheng, "Numerical Simulation of an Improved Structure for High-Resistance Grate Plates," in *Energy Procedia*, 2016.

[60]   A. Atmaca and M. Kanoglu, "Reducing energy consumption of a raw mill in cement industry," *Energy*, 2012.

[61]   A. Atmaca and R. Yumrutaş, "Analysis of the parameters affecting energy consumption of a rotary kiln in cement industry," *Appl. Therm. Eng.*, 2014.

[62]   A. Atmaca and R. Yumrutaş, "The effects of grate clinker cooler on specific energy consumption and emissions of a rotary kiln in cement industry," *Int. J. Exergy*, 2015.

[63] A. Atmaca and R. Yumrutaş, "Thermodynamic and exergoeconomic analysis of a cement plant: Part i - Methodology," *Energy Convers. Manag.*, 2014.

[64] A. Atmaca and R. Yumrutaş, "Thermodynamic and exergoeconomic analysis of a cement plant: Part II - Application," *Energy Convers. Manag.*, 2014.

[65] K. S. Mujumdar, K. V. Ganesh, S. B. Kulkarni, and V. V. Ranade, "Rotary Cement Kiln Simulator (RoCKS): Integrated modeling of pre-heater, calciner, kiln and clinker cooler," *Chem. Eng. Sci.*, 2007.

[66] E. Worrell, L. Price, N. Martin, C. Hendriks, and L. O. Meida, "Carbon dioxide emissions from the global cement industry," *Annu. Rev. Energy Environ.*, 2001.

[67] A. Rahman, M. G. Rasul, M. M. K. Khan, and S. Sharma, "Aspen plus based simulation for energy recovery from waste to utilize in cement plant preheater tower," in *Energy Procedia*, 2014.

[68] R. Dong, Z. Zhang, H. Lu, and Y. Yu, "Recovery of waste heat in cement plants for the capture of CO 2," *Front. Chem. Sci. Eng.*, 2012.

[69] H. Mikulčić, J. J. Klemeš, M. Vujanović, K. Urbaniec, and N. Duić, "Reducing greenhouse gasses emissions by fostering the deployment of alternative raw materials and energy sources in the cleaner cement manufacturing process," *J. Clean. Prod.*, 2016.

[70] F. Akgun, "Investigation of energy saving and NOx reduction possibilities in a rotary cement kiln," *Int. J. Energy Res.*, 2003.

[71] C. Meyer, "Concrete Materials and Sustainable Development in the United States," p. 12, 2002.

[72] S. Licht *et al.*, "STEP cement: Solar Thermal Electrochemical Production of CaO without CO 2 emission," *Chem. Commun.*, 2012.

[73] S. Licht, B. Wang, and H. Wu, "STEP - A solar chemical process to end

anthropogenic global warming. II: Experimental results," *J. Phys. Chem. C*, 2011.

[74] A. Meier, E. Bonaldi, G. M. Cella, W. Lipinski, and D. Wuillemin, "Solar chemical reactor technology for industrial production of lime," *Sol. Energy*, 2006.

[75] G. Moumin *et al.*, "CO_2 emission reduction in the cement industry by using a solar calciner," *Renew. Energy*, 2020.

[76] S. Abanades and L. André, "Design and demonstration of a high temperature solar-heated rotary tube reactor for continuous particles calcination," *Appl. Energy*, 2018.

[77] S. Tescari *et al.*, "Experimental and numerical analysis of a solar rotary kiln for continuous treatment of particle material," in *AIP Conference Proceedings*, 2018.

[78] B. Igliński and R. Buczkowski, "Development of cement industry in Poland – History, current state, ecological aspects. A review," *Journal of Cleaner Production*. 2017.

[79] U. S. P. R. Arachchige, D. Kawan, L. Tokheim, and M. C. Melaaen, "Model Development for CO_2 Capture in the Cement Industry," *Int. J. Model. Optim.*, 2013.

[80] J. I. Bhatty, F. MacGregor Miller, and S. H. Kosmatka, *Innovations in portland cement manufacturing*. Skokie, Ill. : Portland Cement Association, ©2004, 2004.

[81] "NZ Institute of Chemistry." [Online]. Available: https://nzic.org.nz/.

[82] K. H. W. I. AG, "KHD Humboldt Wedag." [Online]. Available: https://www.khd.com/tube-mills.html. [Accessed: 31-Dec-2019].

[83] H. Gante Caruso, "Reduction of CO_2 Emissions from Cement Plants,"

University of Waterloo, 2007.

[84] CementHouse, "ACC: Cement House." [Online]. Available: https://www.acclimited.com/.

[85] A. D. Salman, M. Ghadiri, and M. Hounslow, *Handbook of Powder Technology Vol 12 Particle Breakage*. Elsevier Science, 2007.

[86] Ömürden Genç, "Energy-Efficient Technologies in Cement Grinding," in *High Performance Concrete Technology and Applications*, S. Yilmaz and H. B. Ozmen, Eds. Muğla, Turkey.

[87] Eiichi Oka, R. Higashi, and T. Nomiyama, "FULL AUTOMATIC VERTICAL RING ROLLING MILL (VRRM) FOR ROLLING RINGS WITH PROFILED CROSS SECTION."

[88] "Raw Material Homogeniation Silo-China Mining." [Online]. Available: http://www.cement-equipment.com/enjhk/.

[89] F. Mariani, F. Risi, and C. N. Grimaldi, "Separation efficiency and heat exchange optimization in a cyclone," *Sep. Purif. Technol.*, 2017.

[90] M. G. Abuov and P. A. Kovgan, "A study of heat-transfer processes in a countercurrent cyclone heat exchanger," *Therm. Eng.*, 2009.

[91] V. Ari, "Experimental Investigation of Preheating Cyclone Reactors Used in Cement Industry," 2000.

[92] "Development of State of the Art-Techniques in Cement Manufacturing: Trying to Look Ahead," Duesseldorf, Geneva, 2017.

[93] S. Frauke, K. Ioanna, S. B. Maria, R. Serge, and D. S. Luis, "Best Available Techniques (BAT) Reference Document for the Production of Cement, Lime and Magnesium Oxide: Industrial Emissions Directive 2010/75/EU:(Integrated Pollution Prevention and Control)," 2013.

[94] Dylan Moore, "Cement Plants and Kilns in Britain and Ireland." [Online].

Available: https://www.cementkilns.co.uk/index.html.

[95] L. Szabó, I. Hidalgo, J. C. Císcar, A. Soria, and P. Russ, "Energy consumption and CO_2 emissions from the world cement industry," Spain, 2003.

[96] Peter Hoddinott, "The role of CEMENT in the 2050 LOW CARBON ECONOMY," Brussels.

[97] H. Piringer, "Lime Shaft Kilns," in *Energy Procedia*, 2017.

[98] "IPPC Reference Document on Best Available Techniques in the Cement, Lime and Magnesium Oxide Manufacturing Industries."

[99] "The Cement Sustainability Initiative (CSI), Cement Industry Energy and CO_2 Performance: Getting the Numbers Right."

[100] R. BASTIER, A. BOCAN, B. GILBERT, and A. REGNAULT, "Fours de cimenterie, atelier de cuisson de clicker," p. 102, 2000.

[101] F. Zeman, "Oxygen combustion in cement production," in *Energy Procedia*, 2009.

[102] B. Liu, M. Wang, Y. Wen, X. Hao, and X. Fan, "Research on control mechanism model of grate cooler based on seepage heat transfer theory," *J. Comput. Inf. Syst.*, 2013.

[103] J. A. Moya, N. Pardo, and A. Mercier, "Energy Efficiency and CO_2 Emissions: Prospective Scenarios for the Cement Industry," 2010.

[104] S. Basu and A. Debnath, *Power Plant Instrumentation and Control Handbook.* .

[105] M. P. Prieto, N. Solomakhina, and P. M. Álvarez de Uribarri, "Multimodal networks and decentralized renewable generation: Network modeling and energy/exergy performance evaluation," in *Urban Energy Systems for Low-Carbon Cities*, 2019.

[106] "Green Match." [Online]. Available: https://www.greenmatch.co.uk/.

[Accessed: 01-Jan-2020].

[107] P. Reiter, H. Poier, and C. Holter, "BIG Solar Graz: Solar District Heating in Graz - 500,000 m2 for 20% Solar Fraction," in *Energy Procedia*, 2016.

[108] TheWorldBank, "The World Bank GROUP." [Online]. Available: https://globalsolaratlas.info/. [Accessed: 01-Jan-2020].

[109] S. Kalogirou, *Solar energy engineering: processes and systems*, 1st ed. Elsevier/Academic Press, 2009.

[110] "Sun Power." [Online]. Available: https://www.sunpower-solar.com/. [Accessed: 01-Jan-2020].

[111] F. Jalili Jamshidian, S. Gorjian, and M. Shafiee Far, "An Overview of Solar Thermal Power Generation Systems; Components and Applications," p. 9.

[112] "SUNTASK." [Online]. Available: https://shen-tai.en.made-in-china.com/product/oKeQXLZgkUWO/China-Poland-CPC-Solar-Collector-with-Largest-Aperature-Area.html.

[113] "Supreme Heating Western Australia." [Online]. Available: https://supremeheatingwa.com.au/solar-pool-heating/evacuated-tube-systems.html.

[114] "Jiaxing Fanrong Electric Appliances." [Online]. Available: https://cnfaro.en.made-in-china.com/.

[115] "CNIM." [Online]. Available: https://www.youtube.com/watch?v=pP48pAb8sec.

[116] I. Pelece and P. Shipkovs, "Theoretical and experimental investigations of cylindrical air-heating solar collector," *Latv. J. Phys. Tech. Sci.*, 2016.

[117] P. Gorantla and B. Janarthanan, "Thermal Model of Cylindrical Trough Collector Receiver," *Int. J. Pure Appl. Math.*, vol. 116, pp. 155–171, 2017.

[118] H. Olia, M. Torabi, M. Bahiraei, M. H. Ahmadi, M. Goodarzi, and M. R.

Safaei, "Application of nanofluids in thermal performance enhancement of parabolic trough solar collector: State-of-the-art," *Applied Sciences (Switzerland)*. 2019.

[119] M. G. Rasul, A. K. Azad, and S. C. Sharma, *Clean Energy for Sustainable Development. Comparisons and Contrasts of New Approaches*, 1st ed. Academic Press, 2016.

[120] "Anushree Greentech India Pvt. Ltd." [Online]. Available: https://www.exportersindia.com/anushree-greentech-india-pvt-ltd/solar-parabolic-dish-concentrator-4008005.htm.

[121] T. Kodama, "High-temperature solar chemistry for converting solar heat to chemical fuels," *Progress in Energy and Combustion Science*. 2003.

[122] "Progressive Solar Energy Systems: Solar Powering the Future." [Online]. Available: http://www.progressivesolarenergysystemsllc.com/2017/12/05/different-kinds-of-renewable-energy/.

[123] S. Qazi, "Solar Thermal Electricity and Solar Insolation," in *Standalone Photovoltaic (PV) Systems for Disaster Relief and Remote Areas*, 2017.

[124] A. Sayigh, *Comprehensive renewable energy*, 1st ed. Elsevier, 2012.

[125] G. Stryi-Hipp, *Renewable Heating and Cooling: Technologies and Applications*. 2015.

[126] K. Lovegrove and W. Stein, *Concentrating solar power technology: Principles, developments and applications*. Woodhead Publishing, 2012.

[127] A. M. Patnode, "Simulation and Performance Evaluation of Parabolic Trough Solar Power Plants," University of Wisconsin, Madison, 2006.

[128] M. F. Modest, *Radiative Heat Transfer*. 2013.

[129] M. Rosa-Clot and G. M. Tina, "The Floating PV Plant," in *Submerged and*

Floating Photovoltaic Systems, 2018.

[130] ZHIFENG WANG, *DESIGN OF SOLAR THERMAL POWER PLANTS*, 1st ed. Academic Press.

[131] "SolarPaces (2010) Solar parabolic trough." .

[132] "Final Report - ECOSTAR (European Concentrated Solar Thermal Road-Mapping)."

[133] R. Z. Wang and T. S. Ge, *Advances in Solar Heating and Cooling*. 2016.

[134] P. Poživil, V. Aga, A. Zagorskiy, and A. Steinfeld, "A pressurized air receiver for solar-driven gas turbines," in *Energy Procedia*, 2014.

[135] I. Hischier, D. Hess, W. Lipinski, M. Modest, and A. Steinfeld, "Heat transfer analysis of a novel pressurized air receiver for concentrated solar power via combined cycles," *J. Therm. Sci. Eng. Appl.*, 2009.

[136] C. Borgnakke, R. E. Sonntag, and G. J. Van Wylen, *Fundamentals of thermodynamics*, 7th ed. Wiley, 2009.

[137] O. Kubaschewski and C. B. Alcock, *Metallurgical thermo-chemistry*. National Physical Laboratory, Teddington, Middlesex, England]: Pregman Press, 1979.

[138] M. P. Boyce, *Gas Turbine Engineering Handbook*, 4th ed. Butterworth-Heinemann, 2012.

[139] E. Rathakrishnan, *Elements of Heat Transfer*. 2012.

[140] P. Schwarzbözl, "A TRNSYS Model Library for Solar Thermal Electric Components (STEC)," *Ref. Man. Release 3.0 Köln, Ger.*

[141] "TRNSYS 18," *Univ. Wisconsin-Madison*, 2018.

[142] "TESSLibs 17," *Univ. Wisconsin-Madison*, 2012.

[143] "TRNSYS 18: A TRaNsient SYstem Simulation program," *Univ. Wisconsin-*

Madison.

[144] V. Meyer, A. Pisch, K. Penttilä, and P. Koukkari, "Computation of steady state thermochemistry in rotary kilns: Application to the cement clinker manufacturing process," *Chem. Eng. Res. Des.*, 2016.

[145] P. J. Harper, T. W. Von Backström, T. . Fluri, and D. G. Kröger, "TRNSYS MODELING OF A 100 MWE HYBRID COMBINED CYCLE CONCENTRATING SOLAR POWER PLANT," 2012.

[146] C. M. I. Hussain, B. Norton, and A. Duffy, "Technological assessment of different solar-biomass systems for hybrid power generation in Europe," *Renewable and Sustainable Energy Reviews*. 2017.

[147] T. B. Johansson, H. Kelly, A. K. N. Reddy, L. Burnham, and R. H. Williams, *Renewable Energy: Sources for Fuels and Electricity*. Island Press, 1993.

APPENDIX A

INPUT AND OUTPUT VALUES OF THE UNITS OF A CEMENT PLANT

Table A.1 [30]

Appendix Table A.1 Raw mill inlet properties

Input Materials	$\dot{m}$ (kg/h)	c_p (kJ/kgK)	T_1 (K)
Limestone	74,252	0.82	295
Marl	43,208	0.64	295
Clay	14,856	0.92	295
Iron ore	1350	0.62	295
Bauxite	1350	0.64	295
Moisture of limestone	4455	4.18	295
Moisture of marl	7777	4.18	295
Moisture of clay	2526	4.18	295
Moisture of iron ore	135	4.18	295
Moisture of bauxite	135	4.18	295
Gas from RK	66,346	1.45	567
Return material	27,104	0.81	360
Leaking air	4058	1.01	295
Dust	2103	1.05	565
Electrical work	3250kW		
Total	249,655	-	-

Table A.2 [30]

Appendix Table A.2 Raw mill output properties

Output Materials	$\dot{m}$ (kg/h)	c_p (kJ/kgK)	T_2 (K)
Farine	162223	0.92	380
Hot gas	68346	1.45	380
Steam	15028	2.01	380
Leaking Air	4058	1.01	380
Heat loss	4422.9 kW		
Total	249,655	-	

Table A.3 [30]

Appendix Table A.3 Pyroprocessing tower input properties

Input Materials	$\dot{m}$ (kg/h)	c_p (kJ/kgK)	T_1 (K)
Farine to PYRO Unit	129332	0.92	354
Moisture of Farine	4213	4.19	300
Hot gas from RK	66346	1.55	1725
Ambient Air	4058	1.01	300
Electrical work	5000 kW		
Total	204827	-	

Table A.4 [30]

Appendix Table A.4 Pyroprocessing tower output properties

Output Materials	$\dot{m}$ (kg/h)	c_p (kJ/kgK)	T_2 (K)
Precalcined Farine	103465.6	1.01	1011
Steam	9791	2.01	300
Exhaust gas	66346	1.02	523
Leakages	25224	0.61	300

154

Total	204827	-

Table A.5 [30]

Appendix Table A.5 The rotary kiln inputs properties

Coal content	$\dot{m}$ (kg/h)	c_p (kJ/kgK)	T_1 (K)
C_2	4788	0.03	344
Ash	1468.8	1.3	344
O_2	273.6	0.92	344
H_2	259.2	14.32	344
H_2O	201.6	4.8	344
N_2	115.2	1.04	344
S_2	93.6	5.64	344
Total	7200	1.04263	
LHV of coal	31655.825 (kJ/kg)		

Farine content	$\dot{m}$ (kg/h)	c_p (kJ/kgK)	T_1 (K)
CaO	75,369	0.61	1110
SiO_2	18,543	0.69	1110
Al_2O_3	5145	2.01	1110
Fe_2O_3	2709	4.16	1110
MgO	1312.5	0.37	1110
K_2O	901.95	4.31	1110
H_2O	739.2	4.18	1110
Na_2O	249.9	4.36	1110
SO_3	30.45	0.62	1110
Total	105,000	0.84716	1110

Primary Air content	$\dot{m}$ (kg/h)	c_p (kJ/kgK)	T_1 (K)
N_2	7675.7	1.04	320
O_2	2056.1	0.92	320
Ar	118.4	4.97	320
CO_2	3.9	0.85	320

Table A.5 (Continued)

	$\dot{m}$	c_p	T_1
H$_2$O	3	4.18	320
Other	8.9	1.007	320
Total	9866	1.154	320

Secondary Air content	$\dot{m}$ (kg/h)	c_p (kJ/kgK)	T_1 (K)
N$_2$	69639.6	1.146	1084
O$_2$	18654.1	1.074	1084
Ar	1074.1	4.97	1084
CO$_2$	35.8	1.21	1084
H$_2$O	26.9	2.4	1084
Other	80.6	1.177	1084
Total	89,511	1.09	1084

TOTAL	211577		
Electrical work	4341.5kW		

Table A.6 [30]

Appendix Table A.6 The rotary kiln output properties

Cinker content		$\dot{m}$ (kg/h)	c_p (kJ/kgK)	T_2 (K)
C$_4$AF	4CaO	1956	0.618	1550
	Al$_2$O$_3$	1434.4	2.167	1550
	Fe$_2$O$_3$	2934	4.426	1550
C$_2$S	2CaO	6520	0.618	1550
	SiO$_2$	7824	0.743	1550
C$_3$A	3CaO	3260	0.618	1550
	Al$_2$O$_3$	3390.4	2.167	1550
C$_3$S	3CaO	23472	0.618	1550
	SiO$_2$	11084	0.743	1550
K$_2$O		1304	4.779	1550
SO$_3$		652	0.887	1550
MgO		717.2	0.392	1550
Na$_2$O		652	4.711	1550
Total		65,200	1.0645	1550

156

Hot Gas content	$\dot{m}$ (kg/h)	c_p (kJ/kgK	T_1 (K)
N_2	91975.98	1.083	1120
CO_2	30035.7	1.093	1120
H_2O	7742.54	2.046	1120
O_2	1468.41	1.012	1120
Ar	1334.92	4.97	1120
SO_2	734.21	0.71	1120
Other	200.24	1.05	1120
Total	133,492	1.177	1120

Dust and ash content		$\dot{m}$ (kg/h)	c_p (kJ/kgK	T_1 (K)
C_4AF	$4CaO$	463.86	0.71	710
	Al_2O_3	180.39	2.598	710
	Fe_2O_3	309.24	5.3	710
C_2S	$2CaO$	1713.705	0.705	710
	SiO_2	927.72	0.924	710
C_3A	$3CaO$	734.445	0.705	710
	Al_2O_3	438.09	2.598	710
C_3S	$3CaO$	4329.36	0.705	710
	SiO_2	1546.2	0.924	710
Ash		2241.99	1.3	710
Total		12885	1.0518	710
TOTAL		211,577		

Table A.7 [30]

Appendix Table A.7 Properties of the GCC's inputs and outputs

Input materials	$\dot{m}$ (kg/h)	c_p (kJ/kgK	T_1 (K)
Clinker	63,972	1.21	1595
Cooling Air	169,776	0.99	313
Electrical work	1873kW		
Total	233,748	-	-

Table A.7 (Continued)

Output materials	$\dot{m}$ (kg/h)	c_p (kJ/kgK)	T_2 (K)
Secondary Air	50,580	1.09	1182
Exhaust Air	84,600	1.01	510
Tertiary Air	37996	1.01	910
Cooled clinker	63,972	0.88	390
Total	233,748		

Table A.8 [30]

Appendix Table A.8 Heat loss rates in cyclones and gas channels

Sections	$\dot{Q}_{Total}$ (kW)
1st Cyclone	2119.1
2nd Cyclone	3215.6
3rd Cyclone	5263.8
4th Cyclone	5924
Gas channels	6253.3
Total loss	22775.7

Table A.9

Appendix Table A.9 Calculated heat exchange rate in each cyclone and its corresponding duct

Sections	$\dot{Q}_{Total}$ (kW)
C_1 and D_1	3,169.8
C_2 and D_2	4,810
C_3 and D_3	7,873.8
C_4 and D_4	8,861.3
Total	24,714.9